Strong Fe-Lα Fluorescent Emission in Type-1 Seyfert Galaxies

by

Sherry Hurlburt

A Thesis Submitted to

Saint Mary's University, Halifax, Nova Scotia

in Partial Fulfillment of the Requirements for

the Degree of Master of Science in Astronomy

(Department of Astronomy and Physics)

August 8, 2013, Halifax, Nova Scotia

Approved: Dr. Luigi Gallo (Supervisor)

Approved: Dr. Robert Deupree (Examiner)

Approved: Dr. Kamil Bradler (Examiner)

Date: August 8, 2013.

Acknowledgements

First, I would like to thank my supervisor, Dr. Luigi Gallo, for his patience and support throughout my last two years at Saint Mary's University. I am also thankful to the faculty, staff, and other graduate students at Saint Mary's for their insights and support.

Thank you to my family, especially Gerald, Arceli, Shawn, Julie, Sarah, Ben, Richard, Anne, Michael, Marc and Alain for the continuous love and support provided to me prior to and during the completion of this work.

Most importantly, I would like to thank my fiancé, Stephen, whose constant encouragement and love helped me to achieve this dream. You are my inspiration and I would not be where I am today without your support. I love you and I am truly blessed to have you in my life.

Contents

iii

List of Figures

List of Tables

x

Abstract

Strong Fe-Lα Fluorescent Emission in Type-1 Seyfert Galaxies.

by Sherry Hurlburt

A search for relativistically blurred Fe-Lα is performed on 353 nearby broad and narrow line Type-1 active galactic nuclei (AGN). Simple phenomenological modeling is applied to establish the presence of Fe-Lα. Potential Fe-Lα emission is detected in 65 of these objects. The detection of such a high signal-to- noise ratio (S/N) feature provides confirmation of the reflection model and also presents the possibility to attempt reverberation mapping in AGN. To determine the strength of the Fe-Lα feature and the S/N of the observation required so that Fe-Lα emission can be differentiated in the spectrum from an absorption edge, simulations were performed for various values of the equivalent width (EW) and the number of counts from $0.5 - 2.0$ keV. Seven objects in the sample have sufficient S/N to potentially distinguish Fe-Lα from absorption. Detailed spectral fitting of these seven objects shows that the driving factor in finding Fe-Lα emitters is simply S/N.

August 8, 2013.

Abbreviations

AGN – Active Galactic Nuclei

ASCA – *Advanced Satellite for Cosmology and Astrophysics*

BBB – Big Blue Bump

BLR – Broad-line Region

BLS1 – Broad-line Seyfert 1

BQS – Bright Quasar Survey

CAIXA – Catalogue of AGN in the *XMM-Newton* Archive

CCF – Current Calibration File

CIF – Calibration Index File

EPIC – European Photon Imaging Camera

ESA – *European Space Agency*

EUV – Extreme Ultraviolet

EW – Equivalent Width

FoV – Field of View

FPA – Focal Plane Assembly

FWHM – Full Width at Half Maximum

GTI – Good Time Interval

HR – Hardness Ratio

IR – Infrared

MOS – Metal Oxide Semi-conductor

NLR – Narrow-line Region

NLS1 – Narrow-line Seyfert 1

ODF – Observation Data File

PSPC – Position Sensitive Proportional Counter

QSO – Quasi-Stellar Object

RASS – *ROSAT All-Sky Survey*

RGS – Reflection Grating Spectrometer

SAS – *XMM-Newton* Science Analysis System

SED – Spectral Energy Distribution

SMBH – Supermassive Black Hole

S/N – Signal-to-Noise ratio

SOC – *XMM-Newton* Science Operations Centre

SSC – Synchrotron Self-Compton

UV – Ultraviolet

WA – Warm Absorber

XMM-Newton – *X-ray Multi Mirror-Newton*

XSA – *XMM-Newton* Science Archive

Chapter 1

Introduction

1.1 Active Galactic Nuclei

1.1.1 AGN versus Normal Galaxies

Active Galactic Nuclei (AGN) are galactic nuclei that are interacting with their surroundings and that show energetic phenomena, such as large electromagnetic luminosities and/or extended jets. These energetic phenomena are caused by a central supermassive black hole (SMBH), i.e. a black hole with mass of $\sim 10^6 - 10^9$ M$_\odot$, which is actively accreting matter from its surroundings via an accretion disk into a relativistically deep gravitational potential well. AGN differ from normal galaxies, which have inactive SMBHs at their centres, in several ways. The emission from the central source of an active galaxy can be brighter than the combined emission from all the stars in the host galaxy. AGN emission can cover the entire electromagnetic spectrum, from radio waves to gamma-rays, whereas the spectrum of a normal galaxy is black body in shape and peaks near optical and infrared wavelength (Peterson 1997). Figure 1.1 shows these differences, as well as other features of AGN spectra, which will be discussed later. In addition, active galaxies show variations in brightness over all observable timescales and some have jets originating from the central engine, characteristics that are not seen in normal galaxies.
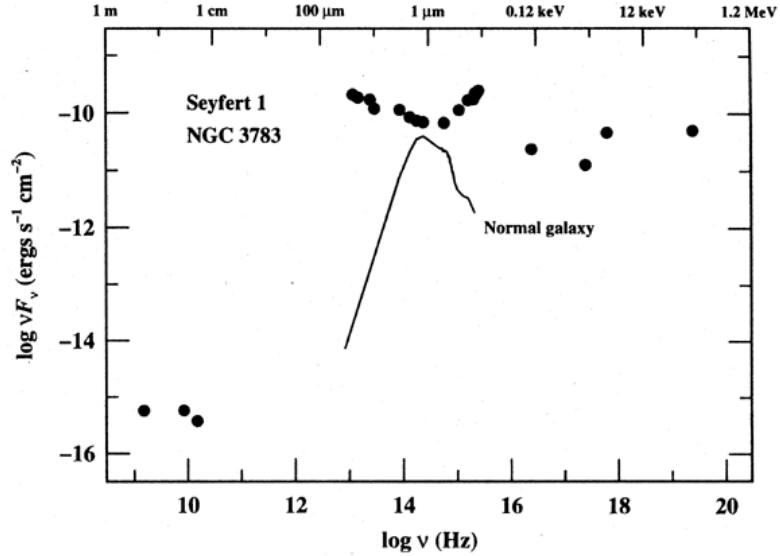
Figure 1.1: *The broadband spectral energy distribution (SED), from radio waves to gamma-rays, of the radio-quiet Seyfert-1 galaxy NGC 3783. For comparison, the SED of a normal galaxy is also shown. Spectral features that can be seen include the IR bump (1 μm and longward), the submillimeter break (far IR to submillimeter wavelengths), and the big blue bump (1μm and blueward). Figure from Peterson (1997). Reproduced by permission.*

1.1.2 Type-1 and Type-2 Seyfert Galaxies

Seyfert galaxies are lower luminosity, radio-quiet[1] AGN that have stellar-like cores and unusual ultraviolet (UV), optical, and infrared (IR) emission line characteristics. There are two main subclasses of Seyfert galaxies, known as Type-1 and Type-2. Type-1 Seyfert galaxies (or Seyfert-1 galaxies) are characterized by two kinds of emission lines that can be superposed on one another. The first are narrow lines (e.g. [OIII]λ5007) that have widths on the order of 10^2 km s^{-1} and properties of a low-density[2], ionized gas, which defines the narrow-line region (NLR). The second are the broad lines that are seen as permitted line transitions (e.g. $H\alpha, H\beta$) only and have widths of up to $\sim 10^4$ km s^{-1}. They have properties of a high-density gas (since broad forbidden-lines are not

---

[1]An AGN is said to be radio quiet if $F(5GHz)/F(B) < 10$, where $F(5GHz)$ is the radio flux at $5GHz$, and $F(B)$ is the optical B-band ($\sim$ 4400 Å) flux (Peterson 1997).

[2]The low-density property of the gas allows forbidden-line transitions to occur because the lack of collisions allows atoms in excited states to de-excite by emitting forbidden-line photons instead of de-exciting via collisions.

seen), which defines the broad-line region (BLR) (Peterson 1997). Since the gas that the broad lines are emitted from is situated close to the black hole and is rotating around it with high velocities, the emitted photons are Doppler shifted and hence the observed emission lines are broadened. The gas that the narrow lines are emitted from is more distant from the black hole and thus these emission lines are narrower than the broad lines. The kinematics of the NLR are likely dominated by the host galaxy and not by the central black hole. Only narrow lines are seen in Seyfert-2 galaxies. A particularly interesting subclass of Seyfert-1 galaxies is the Narrow-Line Seyfert-1 (NLS1) galaxies, which are characterized by narrow broad lines and strong Fe II emission in the optical/UV. More formally, they have broad optical Balmer emission lines, with $\text{FWHM}_{H\beta} < 2000 \quad \text{km s}^{-1}$, and weak forbidden lines with $[\text{OIII}](\lambda 5007)/\text{H}\beta_{\text{total}} < 3$ (Osterbrock & Pogge 1985, Goodrich 1989). Their unique features are believed to be due to low inclinations and/or high Eddington accretion rates (Grier *et al.* 2012).

To explain the large variety of AGN, unified models of AGN have been proposed. It is believed that the observed features of some AGN depend on the viewing angle of the system, where the differences we observe can be attributed to our vantage point (Krolik 1999). A unification model can be used to explain why broad lines are seen in Seyfert-1 galaxies, but not in Seyfert-2 galaxies. This concept is illustrated in Figure 1.2. If we have a direct view of the region surrounding the SMBH of a galaxy, we would see both the narrow line and broad line regions and classify the galaxy as a Seyfert-1. However, if we view the central region through a dusty torus located far from the BLR, we would only see the NLR and classify the galaxy as a Seyfert-2. Thus, the same AGN can be classified differently, depending on the orientation at which the system is viewed. This hypothesis has been successful in accounting for the first-order differences between some Type-1 and Type-2 AGN; however, there are intrinsic differences between AGN as well (Krolik 1999, Peterson 1997).
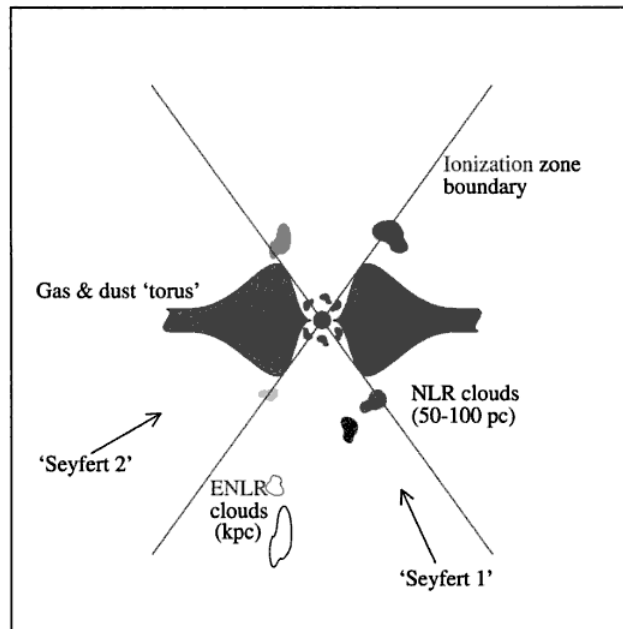
Figure 1.2: *A schematic (not to scale) for the unification of Seyfert-1 and Seyfert-2 galaxies. The central continuum source and BLR are surrounded by the dusty torus. An observer viewing the continuum source and BLR close to the axis of the torus would have an unobscured view of the central region and classify the galaxy as a Type-1. If the observer views the continuum source and BLR close to the midplane of the torus, the central region is obscured and thus the observer would classify the same galaxy as a Type-2. Figure from Peterson (1997). Reproduced by permission.*

1.1.3 AGN Spectra

The continuum spectra of AGN are quite different from that of normal galaxies (Figure 1.1). black body emission, which is a good first-order approximation of the spectra of normal galaxies[3], cannot be used to describe all parts of AGN spectra. Broadband continuum spectra of AGN can, however, be approximated by power laws. This led to the notion that AGN continua have a non-thermal origin (Peterson 1997). This continuum emission is believed to be caused by Comptonization, i.e. inverse Compton scattering or synchrotron self-Compton (SSC), since these processes result in power law spectra with high-energy cut-offs in the X-ray region. This is because the non-thermal processes

---

[3]A black body is a good approximation to the spectra of normal galaxies because the collection of thermal radiation of all stars typically peaks in optical or UV.
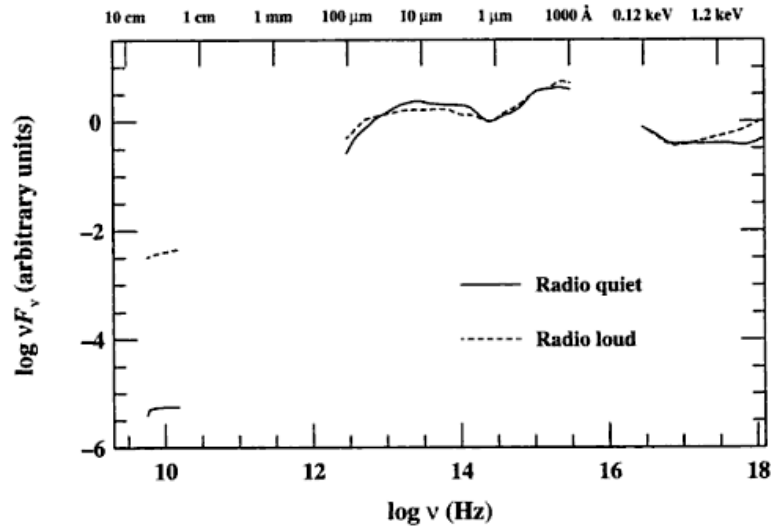
Figure 1.3: *The mean SEDs from the sample of radio-loud and radio-quiet AGN, shown by the dashed and solid lines, respectively. Two gaps are seen in the SEDs, one in the EUV ($\sim 0.12\ keV$) and one in the millimeter wavelength region (see text for details). As in Figure 1.1 the IR bump (1 μm and longward), the submillimeter break (far IR to submillimeter wavelengths), and the big blue bump (1 μm and blueward) can also be seen. Figure from Peterson (1997). Reproduced by permission.*

which give rise to the power law emission no longer dominate at such high energies.

As Figure 1.3 shows, there are two gaps in the spectra at energies below ~ 100 eV. One gap is in the extreme ultraviolet (EUV) region (~ 0.12 keV) and is due to absorption by neutral hydrogen in the disk of the Galaxy. The other is in the millimeter wavelength region and is due to the opacity of the Earth's atmosphere and a lack of sensitive detectors for $\lambda \geq 300\ \mu$m (Peterson 1997). Since the radio continuum is flat and can be described by a power law, the emission is non-thermal and is thought to be due to synchrotron radiation (possibly from extended jets). The bolometric luminosity emitted in the radio band ($\sim 10^{10}$ Hz) is approximately an order of magnitude greater in AGN than in normal galaxies (see Figure 1.3) and up to several orders of magnitude greater in some cases [4].

While a power law is a reasonable first order approximation, there are some important features that it overlooks. In the infrared (IR) region ($\sim 1 - 100\mu$m), an enhancement above the power law

---

[4]Note that radio-quiet objects are not radio silent. Even in radio-loud objects, the radio emission is usually much weaker than the emission from other bands.

is seen for wavelengths longward of 1 μm. This feature, shown in Figures 1.1 and 1.3, has led some to believe that the IR emission has a thermal origin. It is attributed to emission by warm dust grains and is known as the "IR bump" (Krolik 1999). Far IR to submillimeter observations of radio-quiet AGN also show a rapid decrease at low energies (Figures 1.1 and 1.3). This is referred to as the "submillimeter break". Most of the bolometric luminosity of an AGN is emitted in a strong broad feature that dominates AGN spectra blueward of 1μm and extends into the ultraviolet (UV). This feature is known as the "big blue bump" (BBB) and is attributed to thermal emission originating from a geometrically thin, optically thick accretion disk (Peterson 1997). X-ray emission accounts for about 10% of the bolometric luminosity of AGN, and the rapid variability suggests that they come from the innermost regions of AGN (Mushotzky *et al.* 1993). Thus, X-rays are critical probes for studying the underlying processes and physics involved in these regions. In the next section, we will discuss the X-ray spectrum ($\sim 0.1 - 100$ keV) of AGN in more detail. Some AGN spectra also show a gamma ray power law. This power law is weaker than what we would expect by extrapolating the X-ray power law to higher energies. The origin of the gamma ray emission is not well understood, but is generally attributed to synchrotron self-Compton (SCC) (Krolik 1999, Peterson 1997).

1.2   The X-ray Spectrum of Type-1 AGN

Type-1 AGN (i.e. Seyfert-1 AGN) offer the cleanest view of the SMBH region. As such, they are the ideal objects for studies of regions closest to the black hole and thus we will focus on Type-1 AGN in this work. Their X-ray continuum from 2-50 keV is well described by a power law. Again, this is because a power law is a good representation of the Comptonization process that causes the primary X-ray emission. This emission originates from an extended atmosphere of hot electrons, known as the corona (or primary X-ray emitter), which surrounds the inner regions of the SMBH and accretion disk. While we are able to determine that the corona is a very compact region[5], its geometry still remains unknown (Reynolds & Nowak 2003). UV photons emitted from the accretion disk pass

---

[5]We know the corona is compact because from reverberation mapping studies, the rapid variability of the X-rays implies a small emitting region.

through the corona, where the hot electrons transfer energy to the photons, which then emanate from the corona with higher energies as X-rays. The corona is an isotropic emitter, thus some of the X-rays are emitted towards the observer, while others illuminate the inner accretion disk. Therefore, some of the emitted X-rays will also irradiate the cold, optically thick accretion disk, giving rise to back-scattered emission called the reflection spectrum. The observed X-ray spectrum will thus be a combination of the primary emission from the corona and the reflected emission from the disk. This is shown in Figure 1.4.
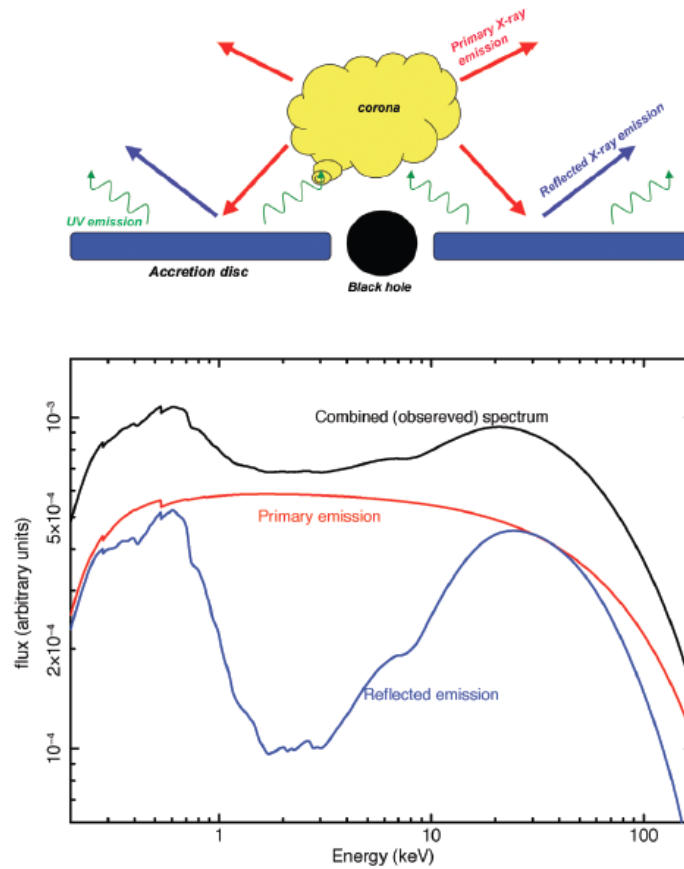
Figure 1.4: *The top image is a depiction of the inner black hole region, while the bottom shows the corresponding contribution of each component to the observed X-ray spectrum. Figure from Gallo (2011). Reproduced by permission.*

1.2.1 Warm Absorption

Absorption features, mostly K-shell and L-shell ionization edges of heavy elements (i.e. O, Fe, Mg, Si and S), are often seen at lower X-ray energies in Type-1 AGN spectra. These are due to 'warm absorbers', i.e., partially ionized, optically thin gas along our line of sight to the X-ray source (Reynolds & Nowak 2003, Peterson 1997). These warm absorbers are located at large distances from the inner black hole region. Warm absorbers are the main source of the spectral complexity seen at low energies in Seyfert-1 AGN spectra (Miller 2007). As they are highly ionized, the warm absorber clouds are distinct from the BLR clouds. Absorption features associated with distant cold (neutral) gas (or the host galaxy) are also seen in X-ray spectra.

1.2.2 The Soft Excess

Another feature of the X-ray spectra of Type-1 AGN is the "soft excess", a sharp rise above the power law below ~ 1 keV. A black body in the soft X-ray regime of Seyfert-1s can characterize this soft excess component. The origin of the soft excess is unknown, however, some believe that it is the Comptonized (Wien) tail of the big blue bump (Peterson 1997). This is not the case for most Seyfert-1 AGN since the soft excess is not caused by thermal emission from the accretion disk as the inferred temperatures are unreasonably high and do not vary with luminosity (Miller 2007). In these cases, the soft excess is believed to be due to a collection of blurred X-ray emission lines from the accretion disk. The nature of the soft excess is still unknown, and this feature is one of the least understood aspects of the X-ray spectrum.

1.2.3 Distant Reflection

X-ray spectra of Type-1 AGN also rise above the power law at higher energies. This component is known as the "Compton hump" or "hard tail" and is attributed to Compton reflection off the accretion disk or more distant matter (Peterson 1997). Some Type-1 AGN also show signatures of reflection from distant gas. These are associated with scattered emission from the torus, which is

located light months to light years away (Fabian 1996).

1.3 The Reflection Spectrum

1.3.1 Continuum and Emission Lines

Reflection spectra of Seyfert-1 AGN are generated from partial reprocessing of the primary X-ray emitter by the cold (relatively neutral) accretion disk surrounding the SMBH. As the continuum source illuminates the cold accretion disk from above, the X-ray photons will have two possible fates. They will either undergo Compton scattering by bound electrons (the outer electrons of non-ionized atoms) or free electrons (associated with ionized H and He), or photoelectric absorption, thus ionizing the top layers of the disk. The resulting ion will now de-excite in one of two ways, both beginning with an L-shell ($n = 2$) electron dropping down to the lower energy K-shell ($n = 1$). Either the excess energy is emitted as a Kα photon (this process is known as fluorescence), or the extra energy ejects another L-shell electron (known as the Auger effect) (Reynolds & Nowak 2003). The probability that an ion in an excited state will de-excite by emitting a fluorescent photon instead of emitting an Auger electron is known as the fluorescent yield of the species. Again, this photoionization produces the reflection spectrum. X-ray reflection spectra consist of emission lines due to fluorescence of the most abundant metals, which dominate the spectra below 10 keV, and the Compton hump, which peaks around $20 - 30$ keV (Figure 1.5). Since photoelectric absorption depends on the photon energy, incident soft X-rays will be mostly absorbed while incident hard X-rays will be Compton scattered back out of the disk. This explains the Compton hump at higher X-ray energies. The reflection spectrum is an important component of AGN X-ray spectra as it yields information on the incident X-ray emission and ionization state of the accretion disk.

1.3.2 Fe-Kα

Due to its high cosmic abundance and high fluorescent yield, the most prominent fluorescent emission line is the iron Kα line at ~ 6.4 keV (Reynolds & Nowak 2003). The Fe-Kα line is mostly isolated
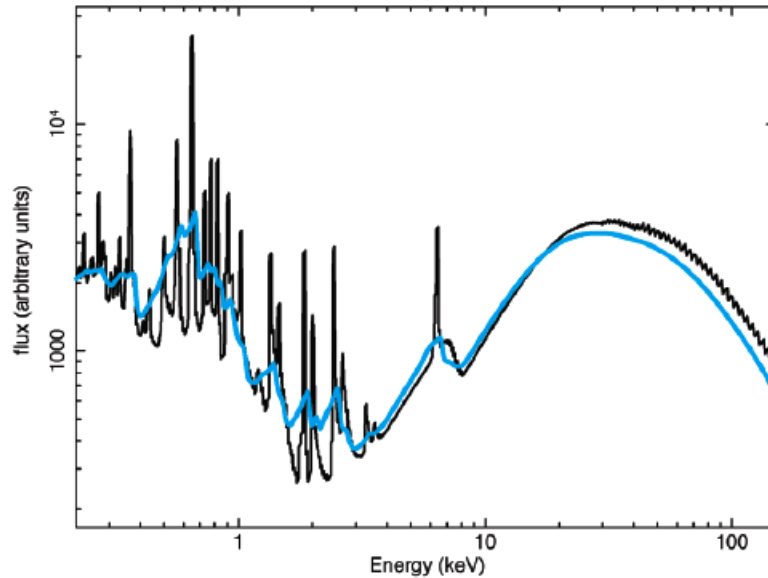
Figure 1.5: *The reflection spectrum produced by X-ray irradiation of a power law primary emitter onto a lowly ionized accretion disk (black). The blue line shows the same reflection spectrum modified by relativistic effects (these effects will be discussed in Section 4). Figure from Gallo (2011). Reproduced by permission.*

from the other weak emission lines, which are mostly found below 2 keV, also making it stand out. A feature resembling a "shoulder" is seen redward of the Fe-Kα line. This characteristic, known as the "Compton shoulder", arises due to the line photons that have undergone Compton scattering before emerging from the disk (Peterson 1997). The Fe-Kα line is often seen, with varying strength, in AGN. For objects with large iron abundances, it may also be possible to detect Fe-Lα line emission, a feature that is predicted to coincide with Fe-Kα (Fe-Lα fluorescence will be discussed in section 1.5.2).

While H and He are completely ionized, the metals in accretion disks may not be completely ionized and hence can imprint spectral lines, edges and other signatures on the reflection spectrum. The strength and shape of these features, which are due to photoelectric absorption, fluorescence and Compton scattering processes, tell us information about the composition, motion, abundance, and ionization of the accretion disk, the gravitational potential depth of the SMBH, as well as the

geometry of the SMBH region.

1.3.3 Constant Density Models

A simple X-ray reflection model that produces most of the features seen in AGN spectra consists of a semi-infinite, cold slab of constant density gas that is irradiated from above by an X-ray power law continuum. Such models are referred to as constant density models and were the first models used for computing theoretical reflection spectra (Ross & Fabian 1993). Assuming the accretion disk structure is stationary, time-independent, and of constant density (with cosmic abundances) and that the outer layers of the disk are in thermal and ionization equilibrium allows the structure of the disk atmosphere, and hence the reflection spectrum, to be obtained (Reynolds & Nowak 2003). It is now useful to define the ionization parameter, $\xi(r) = 4\pi F_x(r)/n(r)$, where $F_x(r)$ is the X-ray flux per unit area of the accretion disk at radius r and $n(r)$ is the co-moving electron number density. Thus, the ionization parameter measures the ratio of the photoionization rate to the recombination rate. For constant density models, the value of the ionization parameter characterizes four different regions of behavior, shown in Figure 1.6, where $\xi < 100$ erg cm s^{-1} is the neutral reflection region, 100 erg cm s$^{-1} < \xi < 500$ erg cm s^{-1} is the intermediate ionization region, 500 erg cm s$^{-1} < \xi < 1000$ erg cm s^{-1} is the high ionization region, and $\xi > 5000$ erg cm s^{-1} is the fully ionized region. Differences among theoretical reflection spectra with varying values for the ionization parameter show an Fe-Kα emission line at 6.4 keV for lowly ionized disks, whereas Compton back-scattering contributes mostly to the emission near 6 keV for highly ionized disks.

To show how the reflection spectrum can be useful for obtaining information about the black hole region, George & Fabian (1991) determined the dependence of the shape of the reflection spectrum on various parameters, such as elemental abundances of the accretion disk material, the inclination angle (defined relative to the normal of the accretion disk), and the intensity of the incident X-rays, for two different geometries. They also confirmed that, as expected, the distribution of the irradiating continuum photons that escape from the slab depends strongly on both the initial energy and incident angle of the primary X-rays. As can be seen from Figure 1.7, emerging fluorescent photons with
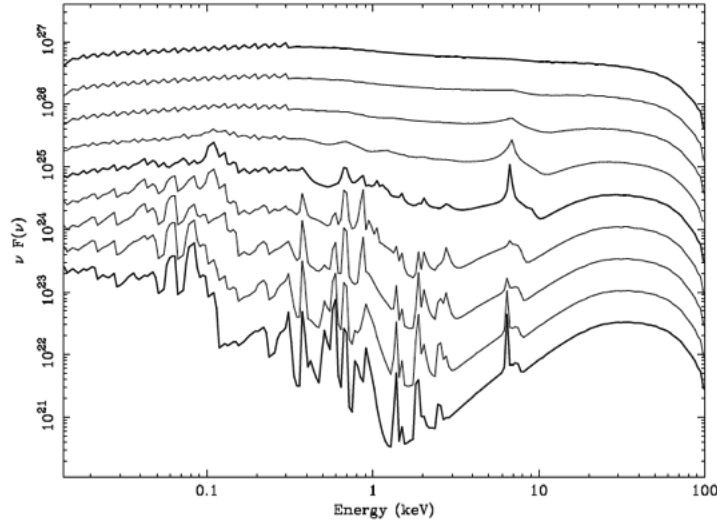
Figure 1.6: *Theoretical reflection spectra for ionization parameters* $log(\xi) = 1.0-5.0$, *in increments of 0.5 from top to bottom. Figure from Reynolds & Nowak (2003). Reproduced by permission.*

high incidence angles, θ_0, are more likely to escape to the surface as they originate from smaller vertical depths into the slab (on average). The photon index, Γ, is the spectral index of the X-ray power law $F(E) \propto E^{-\Gamma}$, where $\Gamma = \alpha + 1$ and α is the power law index. Their results for the profile and equivalent width of the Fe-Kα fluorescent line (generated with a simple constant density model) are consistent with the observations of the line in several AGN. Ross & Fabian (2005) also assumed a constant density atmosphere for their computations of model reflection spectra. Using their code, they produced a comprehensive grid of reflection models, for all important ionization states and transitions, with the ionization parameter, the spectral index, and the iron abundance as free parameters. As can be seen in Figure 1.6, varying the ionization parameter has a large effect on the emission and absorption features of the reflection spectrum. The shape of the reflection spectrum depends significantly on the photon index, which also affects the emission and absorption features, and the iron abundance (Figure 1.8). More recent models relax the assumption of constant density, and assume that the outer layers of the disk are in hydrostatic equilibrium; however, the results generally agree with those of the constant density models (Ballatyne *et al.* 2001). The
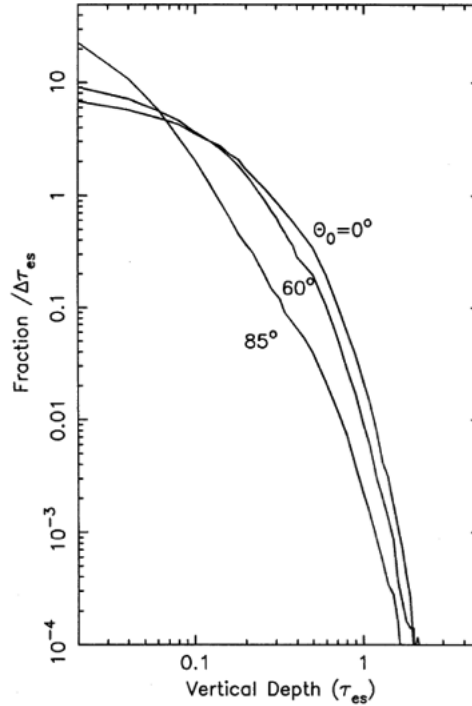
Figure 1.7: *Plot of the fraction of escaping fluorescent photons produced per unit of depth as a function of vertical depth into the slab. This is shown for three values of θ_0 (as indicated), assuming an incident power law with a photon index $\Gamma = 1.7$. Figure from George & Fabian (1991). Reproduced by permission.*

assumption of an accretion disk with constant density allows models to run faster than those without this assumption, which are very time consuming. In addition, constant density models are useful because the geometry of the inner black hole region is unknown for many sources.

1.4 Blurring Effects and Models

1.4.1 Blurring Effects

Emission lines in the reflection spectrum are intrinsically narrow; however, they become shaped and broadened in the black hole environment. First, we will consider how Doppler effects change an intrinsically narrow emission line. Since the accretion disk is rotating, some regions of the disk are moving towards us while others are moving away. The emission coming from the regions
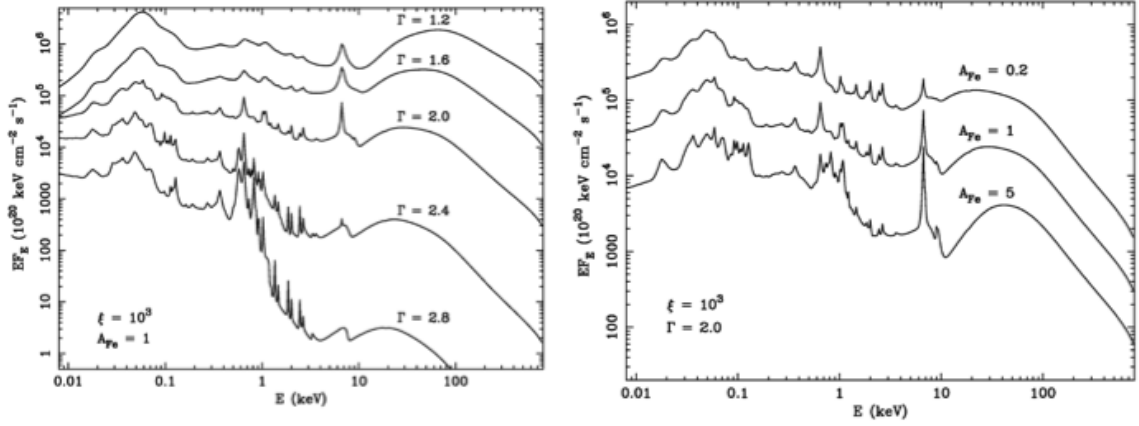
Figure 1.8: *Left panel: Reflection spectra for various values of the photon index. The illuminating spectrum has fixed values of the ionization parameter and iron abundance, where $\xi = 10^3$ erg cm s^{-1} and $A_{Fe} = 1$ (i.e. Solar). Right panel: Reflection spectra for various values of the iron abundance. The illuminating spectrum has fixed values of the ionization parameter and photon index, where $\xi = 10^3$ erg cm s^{-1} and $\Gamma = 1.2$. Figure adapted from Ross & Fabian (2005). Reproduced by permission.*

moving towards us will appear blueshifted while the emission from the regions moving away from us will appear redshifted. This causes the emission line to appear double-peaked. We also know that the material close to the black hole is moving at a speed close to the speed of light and thus it is susceptible to special relativistic effects. As a result, the light radiating from material moving towards us will be beamed, or enhanced, and the light radiating from material moving away from us will be dimmed. The observed emission line will now be broadened, redshifted, and asymmetric, with a higher blue peak and lower red peak. Additionally, general relativistic effects modify the observed reflection spectrum very close to the black hole because the photons lose energy as they escape from the deeper gravitational well. Hence, the emission line appears redshifted since all the photons making up the line have lost energy. In addition, photons that are closer to the black hole lose more energy than those farther away, causing the line profile to be stretched to lower energies. As Figure 1.9 shows, the observed profile of the emission line is a superposition from all these effects at different distances from the black hole. Therefore, the geometry and dynamics of the black hole region can be determined by modelling the shape of the observed emission lines in the reflection
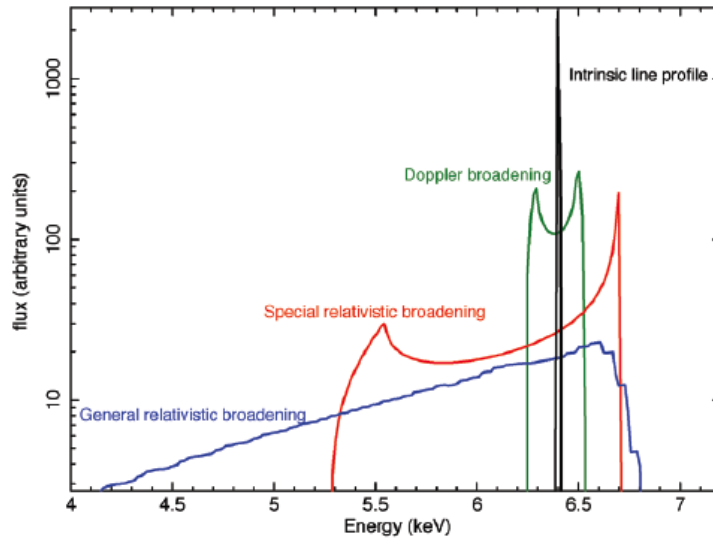
Figure 1.9: *Changes to the intrinsically narrow emission line (black line profile) due to Doppler, special relativistic and general relativistic effects are shown by the green, red, and blue line profiles, respectively. Figure from Gallo (2011). Reproduced by permission.*

spectrum.

1.4.2   Light-bending

Since the power law component is generated by the corona, this component should dominate the X-ray spectrum. However, in some cases, the secondary reflection spectrum rises above the primary power law component. This unexpected behaviour can be explained by light-bending which, to the observer, weakens the power law emission while not substantially reducing the reflection spectrum. Due to the curvature of spacetime around black holes, geodesics follow a curved path that bends around the central mass. Therefore, if the corona is close enough to the black hole, most of the geodesics will curve toward the inner accretion disk and black hole. As an isotropic emitter, the X-ray emission from the corona, as seen by the observer, will be diminished while the reflected X-ray emission that reaches the observer will be maintained (or even increased). The effects of light-bending on the central region and the observed X-ray spectrum is shown in Figure 1.10, in

contrast to Figure 1.4. In addition to explaining the observed dominance of the secondary component above the primary component in X-ray spectra, light-bending also accounts for the X-ray variability seen in some AGN (Gallo 2011). If the observed changes in the X-ray flux are ascribed to geometric effects instead of intrinsic changes in the AGN (which is difficult and abstruse), the variability in some AGN can be successfully explained by light-bending, (i.e. the low-flux state of the AGN is attributed to a reduced primary component). There are some cases, however, where light-bending is incapable of explaining the observed variability, which may actually arise from changes within the primary emitter.
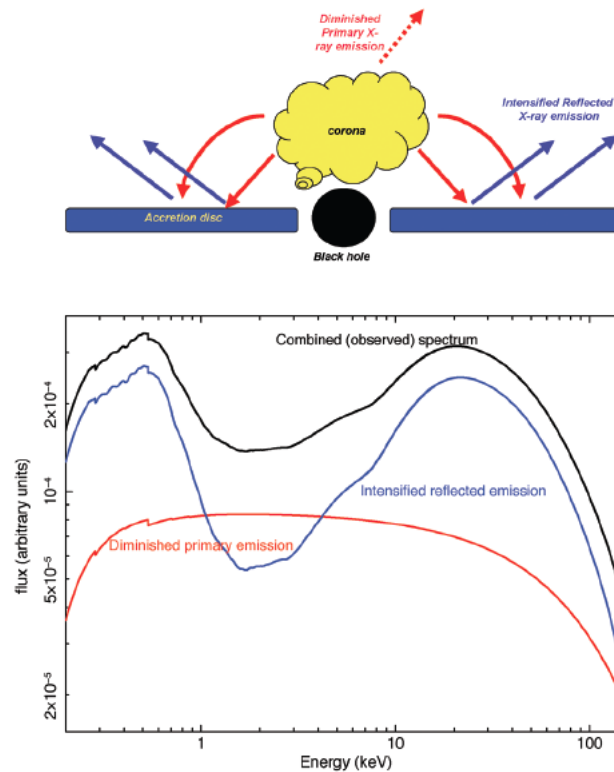
Figure 1.10: *The top diagram shows how the geodesics will curve toward the black hole and inner accretion disk if the corona is situated close enough to this central region, thus diminishing the primary X-ray emission. The bottom diagram shows the effects on the observed reflection spectrum. Figure from Gallo (2011). Reproduced by permission.*
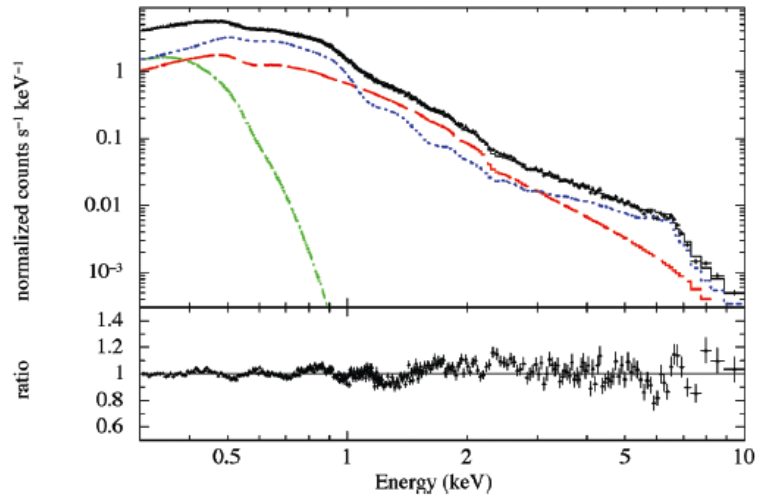
Figure 1.11: *The reflection model and data-to-model ratio of 1H0707-495. The power law, reflection and black body components are shown by the red dashed, blue dotted and green dot-dashed lines, respectively. Figure from Gallo (2011). Reproduced by permission.*

1.4.3   Reverberation Mapping

Due to the primary X-ray emitter and the accretion disk being disjointed components, changes in the primary emitter should be seen in the reflection spectrum after a reverberation lag (that is, the time it takes light to travel across the region). Long, high-quality observations are needed to detect reverberation lags in X-ray spectra because the compactness of the region being considered implies that the delays are very short (i.e. on timescales as short as minutes – hours). As an example, we will consider the $\sim$500 ks observation of the AGN 1H0707-495 taken by *XMM-Newton* in January 2008. The reflection model used to fit the spectrum of 1H0707-495, and the data-to-model ratio are shown in Figure 1.11. As this figure demonstrates, the reflection component dominates the 0.3 – 1.0 keV and 4 – 10 keV ranges of the spectrum, while the primary component only dominates in the intermediate 1 – 4 keV range. This can be explained by the aforementioned light-bending scenario. We therefore expect changes in the power law dominated region of the spectrum to be appear at other energies at later times. Analysis of 1H0707-495 by Zoghbi *et al.* (2010) (Figure 1.12) shows these reverberation lags. A negative lag is seen where changes in the low energy region

(0.3 – 1.0 keV) follow changes in the intermediate X-ray range (1 – 4 keV). Both long positive lags and short negative lags are seen in the figure. The positive lags, which have been studied for sometime, are attributed to an accretion mechanism of the black hole system (the propagation of accretion fluctuations) and the negative lags are attributed to the light travel time between the primary emitter and the reflection component (Gallo 2011). Detection of these reverberation lags is important because it is the only way to "map out" the unresolved inner black hole region. In addition to 1H0707-495, similar characteristics have been seen in similar sources, such as IRAS 13224-3809 (Fabian *et al.* 2012).
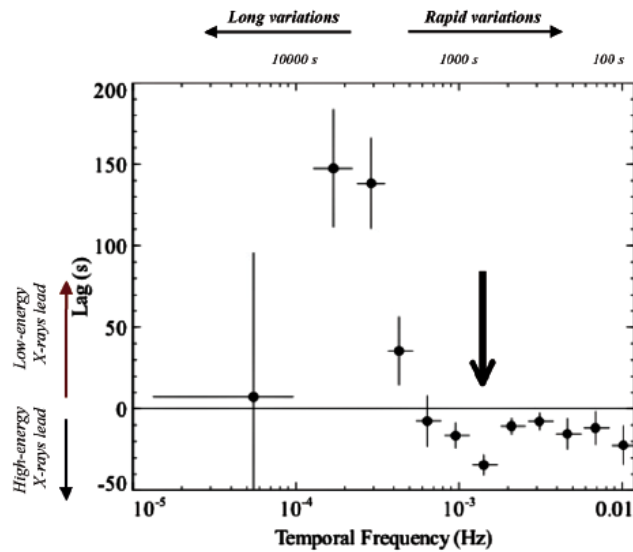
Figure 1.12: *The time lag between the* $0.3 - 1.0 \, keV$ *and* $1 - 4 \, keV$ *regions as a function of Fourier frequency. The black arrow indicates the reverberation lag. Figure from Gallo (2011). Reproduced by permission.*

1.4.4   Disk Emissivity and the Lamp Post Model

The emissivity is the reflected power per unit area as a function of position on the accretion disk. We know that the flux incident on a certain point of the disk decreases with increasing distance from the corona to the disk. Thus, the emissivity profile depends on the location and shape of the corona, and the geometry of the corona and disk system. These parameters can therefore be constrained

by determining their effects on emissivity profiles while also taking into consideration inferred distances from reverberation lags (Wilkins & Fabian 2011). In Euclidean space, the emissivity at a point on the disk is inversely proportional to the square of the distance from the corona times the cosine of the angle (with respect to the normal) of the incident rays. Hence, for large distances between the disk and the source, the emissivity would be inversely proportional to r^3. Close to a black hole, however, the X-rays would be focused towards the inner disk and the black hole itself due to general relativistic effects. Thus, for black hole systems, the emissivity should decrease at a steeper rate with distance assuming a flat accretion disk.
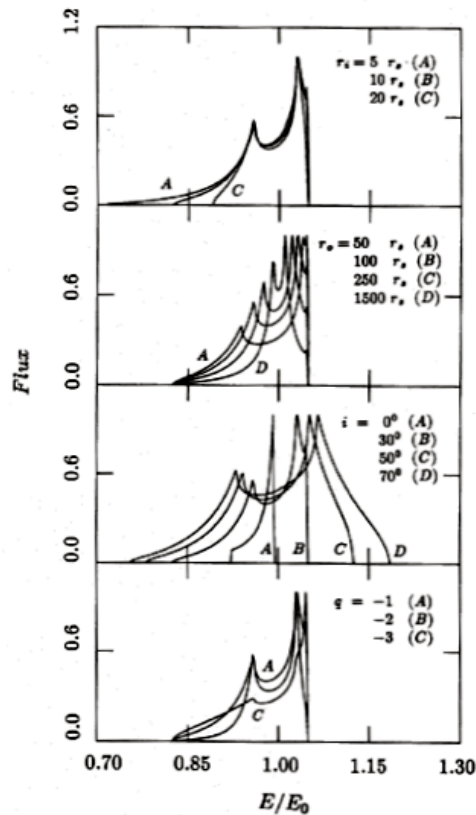
Figure 1.13: *Line profiles for various values of each of the four parameters. From top to bottom, line profiles are shown for a range of inner radius, outer radius, inclination, and emissivity index, while parameters other than the one varied are fixed. Unless otherwise specified, the parameters are fixed at $r_i = 10r_s, r_o = 100r_s, i = 30°$, and $q = 2$ (Fabian et al. 1989). Reproduced by permission.*

Models for profiles of relativistically broadened emission lines from an accretion disk, such as that of Fabian *et al.* (1989), assume for simplicity that the line emissivity follows a power law with a constant index (q) since the radial dependence of the line emissivity is not well known. Line profiles for these relativistically broadened emission lines for various emissivity laws were calculated by Fabian *et al.* (1989) for the case of a Schwarzschild (zero spin) black hole and by Laor (1991) for the case of a Kerr (max spin) black hole. A more realistic emissivity law than that of a power law dependence is the 'lamp-post model'. This model assumes that the corona is located at a height, h, above the centre of the accretion disk. For a flat accretion disk, with negligible relativistic effects on the flux from the corona, the emissivity profile, $J(r_e)$, is proportional to $h/(r_e^2 + h^2)^{3/2}$, where r_e is the initial emission position on the disk. This reduces to the classical case (a power law with $q = 3$) for $r_e \gg h$. However, since most of the flux originates from the inner disk, emissivity profiles are dependent on the height of the corona from the accretion disk. Fabian *et al.* (1989) found that the shape of the line profile is mostly dependent on the outer radius and inclination (with respect to the normal of the accretion disk), the blue peak is always higher than the red peak, a single broadened peak is seen for low inclination and/or large outer radius, and a redshift of the whole profile is only seen for low inclinations. Figure 1.13 shows the theoretical line profiles stepping through ranges of the inner radius, outer radius, inclination, and emissivity index. Laor *et al.* (1991) found that most of the flux is seen at low inclinations for large r_e, the red horn diminishes as r_e becomes smaller, and the shape of the line is mostly altered by general relativistic effects at low inclinations whereas it is mostly altered by the Doppler effect for high inclinations. The line profiles observed at various values of $\mu = \cos(\theta_0)$ and emitted at specific r_e are shown in Figure 1.14. Since the line profiles mostly depend on the inner radius, the outer radius, the inclination, and the emissivity index, the shape of the line can be used as a diagnostic for the location of the emission region and the inclination of the black hole system (Miller 2007, Reynolds & Nowak 2003). Laor (1991) also calculated the effects of the different emissivity laws on the shape of the line profile. He determined that the lines are likely to be asymmetric and broad, with a sharp blue wing and an extended red wing (confirming the results of Fabian *et al.* 1989), and that most of the line peaks should be blueshifted.
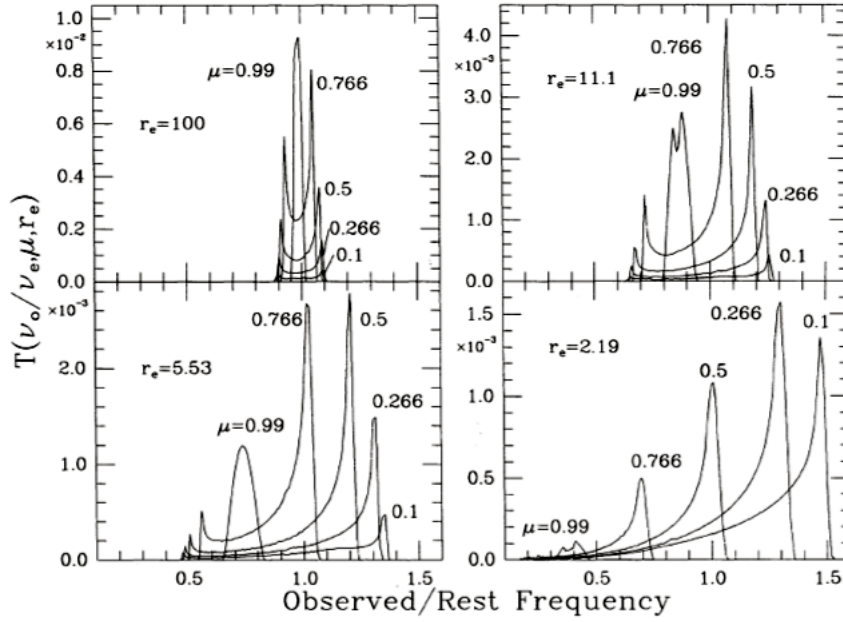
Figure 1.14: *Profiles of a line emitted at specific r_e and observed at various inclination angles. For small values of r_e, relativistic effects significantly affect the line profile. Figure from (Laor 1991). Reproduced by permission.*

While Fabian *et al.* (1989) and Laor (1991) generally agree, there are some differences in their results. The results from Laor (1991) differ from those of Fabian *et al.* (1989) in that they show stronger relativistic effects. These differences are attributed to the fact that different metrics were used.

1.4.5 Measuring Black Hole Spin

The profiles of relativistically broadened emission lines can also be used to measure the spin of black holes. One way to do this is by examining the breadth of the red wing of a relativistic disk line (Brenneman & Reynolds 2006). Photons climb deeper potential wells, (and thus lose more energy) the closer they are emitted to the black hole. As a result, the red wing of the line profile becomes more extended as the material gets closer to the black hole (Figure 1.15). The proximity of the material to the black hole is dictated by the inner accretion disk edge, which partially depends on the
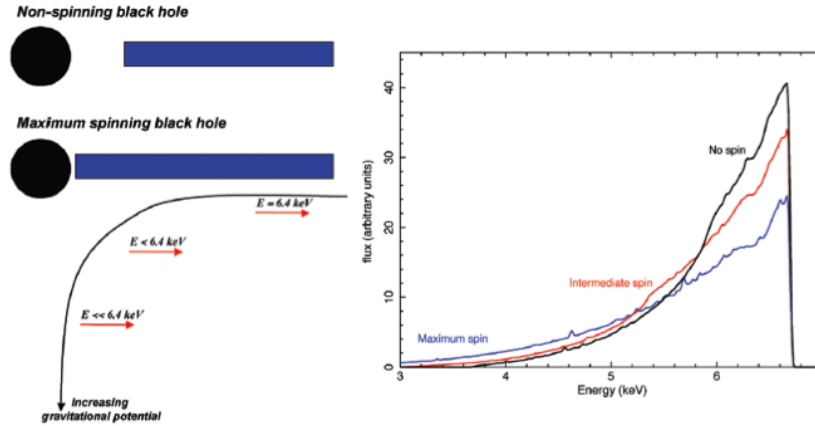
Figure 1.15: *Left Panel: The inner region of both a non-spinning and a maximum spinning black hole. As the spin increases, the inner edge of the accretion disk moves closer to the black hole event horizon. As a result, photons emitted close to the black hole undergo larger gravitational redshifts. Right panel: The effects of black hole spin on the line profile of a relativistically broadened disk line. Figure adapted from Gallo (2011). Reproduced by permission.*

black hole spin. A spinning black hole has an innermost stable circular orbit (ISCO) that is up to five times closer to the event horizon than a non-spinning black hole because of frame dragging caused by the rotation of the black hole (Gallo 2011). This scenario is portrayed in Figure 1.15. Because the reflection models are calculated in the fluid frame they need to be convolved with relativistic line models to obtain the spectrum as seen by a distant observer. The parameters obtained from fitting this convolved spectrum can then be used to determine the black hole spin, which is a more complete method than that of fitting a disk line (Miller 2007). Black hole spin is usually measured by the dimensionless spin parameter, a, which is defined as $a = cJ/GM^2$, where J and M are the angular momentum and mass of the black hole, respectively. A non-spinning (i.e. Schwarzschild) black hole has a spin parameter of $a = 0$, while a maximal spinning Kerr black hole has a value of $a = 0.998$. The technique of using relativistic disk lines to measure black hole spin has been used on several AGN (see Miller 2007, Reynolds & Nowak 2003), such as MGC–6-30-15, NGC 4051, and Mrk 776 (all of which were found to have high spin parameters). Based on the assumption that black holes grow by accretion via a thin disk, current theoretical models predict that 70% of all SMBHs should have maximal spin (Volonteri *et al.* 2005).

1.4.6 Relativistic Emission Line and Convolution Models

Several relativistic emission line models are accessible for fitting through various packages. The DISKLINE model, available through the spectral fitting package named XSPEC (Arnaud 1996), is based on the calculations of Fabian *et al.* (1989). It models an emission line from a relativistic accretion disk around a Schwarzschild black hole. The parameters of the DISKLINE model are the line energy, the emissivity index (which assumes a power law dependence), the inner and outer disk radii (measured in units of Schwarzschild (r_s) or gravitational radii (r_g), where $1r_g = 1/2r_s = GM/c^2$), the inclination of the system, and the photon flux in units of photon cm^{-2} s^{-1}. However, since the entire X-ray reflection spectrum is subject to the same relativistic effects as a single emission line, a convolution model, RDBLUR, was implemented in XSPEC to relativistically blur the emission from an accretion disk. The spectrum is blurred by convolving the reflection spectrum with the profile of the relativistically broadened emission line produced by the DISKLINE model. Since the DISKLINE model only considers the case of a Schwarzschild black hole, the general relativistic calculations for a maximal spin Kerr black hole ($a = 0.998$) by Laor (1991) were implemented as the model LAOR in XSPEC. The KDBLUR model is the convolution model for LAOR and is analogous to the RDBLUR convolution model for DISKLINE. In 2004 the first model that includes spin as a variable parameter, allowing black hole spin to be constrained by spectra, was made available through XSPEC. This model, and its corresponding convolution model are KYLINE and KYCONV, respectively (Dovčiak *et al.* 2004). Brenneman & Reynolds (2006) introduced a new model, KERRDISK, and convolution model, KERRCONV, that also included black hole spin as a variable parameter and enabled physical parameters of the black hole system (such as the angular momentum) to be formally constrained [6].

1.4.7 Physical Models

When the X-ray irradiation is so strong that it determines the ionization state of the accretion disk, models that are more realistic, or physical, are required. The REFLIONX grid of reflection models

---

[6]Such parameters could not be well constrained with the model developed by Dovčiak *et al.* in 2004.

(Ross & Fabian 2005) in XSPEC is an example of a physical model. As mentioned in Section 1.3.3, this model calculates reflection spectra for an optically-thick accretion disk of constant density that is illuminated by an X-ray power-law spectrum. Ross & Fabian (2005) calculated reflection spectra for ionization parameters of $\xi = 30$, 100, 300, 1,000, 3,000 and 10,000 erg cm s^{-1}, photon indices of $\Gamma = 1.0 - 3.0$ in increments of 0.2; and iron abundances of $A_{Fe} = 0.1$, 0.2, 0.5, 1.0, 2.0, 5.0, and 10.0 times the solar value. This produced a grid of 462 reflection models for all abundant species and their important transitions, which is useful for interpreting X-ray spectra from AGN.

As indicated in Section 1.2.1, absorption features due to warm absorbers (ionized gas) along our line of sight may be seen in X-ray spectra of Type-1 AGN. Therefore, it is important to model absorption features when necessary to obtain accurate continuum models. The XSTAR (Kallman & McCray 1982) analytical model in XSPEC calculates physical conditions and emission spectra of warm absorbers. Absorption features due to distant cold gas, or the host galaxy, are also sometimes seen in X-ray spectra. This absorption can be modelled using the ZTBABS model in XSPEC, which calculates the column density of X-ray absorption by cold gas, taking into account the redshift of the source.

1.5 Observations of Relativistic Lines in AGN

1.5.1 Fe-Kα Observations

The most prominent X-ray reflection feature is the Fe-Kα line at 6.4 keV due to its high cosmic abundance, high fluorescent yield, and isolation in the spectrum. As a feature of the reflection spectrum that is believed to originate from just a few gravitational radii from the central black hole, the relativistic effects discussed above broaden this line. Examining the shape of this broad line gives us the clearest views to date for studying the physics that occurs in the black hole environment (Reynolds & Nowak 2003). This broad line is therefore a powerful diagnostic tool for measuring properties of the black hole, such as mass, inclination, spin, and the location and kinematics of the accretion disk, via the techniques of line spectroscopy. The first detection of this broad iron line in an
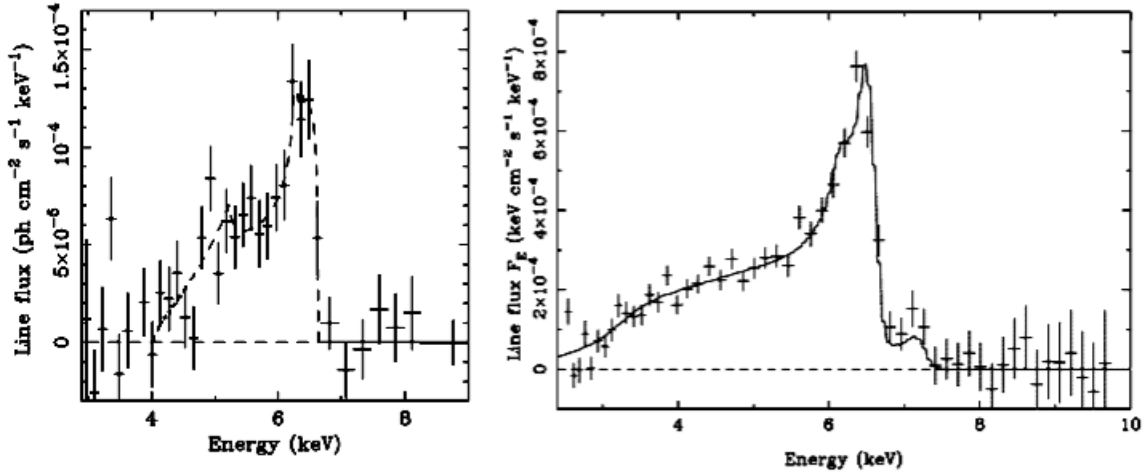
Figure 1.16: *Left Panel: The relativistically broadened iron line (with the continuum subtracted) of MGC–06-30-15 from the long ASCA observation taken in 1994. The line is fit with a model, shown by the dashed line, of an emission line from a relativistic accretion disk around a Schwarzschild black hole. An emissivity profile of r^{-3} extending down to the ISCO is assumed, and the inclination is fixed at $30°$. Figure from Reynolds & Nowak (2003). Reproduced by permission. Right Panel: The relativistic iron line from the higher signal-to-noise 2001 XMM-Newton observation of MGC–06-30-15. Figure from Fabian et al. (2002). Reproduced by permission.*

AGN was found in the Seyfert-1 galaxy MGC–06-30-15 by the *Advanced Satellite for Cosmology and Astrophysics (ASCA)* (Tanaka *et al.* 1995). The iron line of MGC–06-30-15 can be seen in Figure 1.16. Due to its broad iron line as a potential for black hole diagnostics, MGC–06-30-15 is one of the most well studied AGN to date. Broad iron lines have now been detected in several Galactic X-ray sources and AGN and are believed to be common features of normal Seyfert-1 galaxies (Miller 2007, Reynolds & Nowak 2003). Typical equivalent widths of Fe-Kα lines are about 180 eV with red wings extending down to $3 - 6$ keV (Miller 2007).

1.5.2 Fe-Lα Observations

Because the region below 2 keV of the reflection spectrum contains emission from most metals (in addition to iron), absorption lines and edges from warm gas associated with the AGN (or host galaxy) and is blurred by relativistic effects, it is hard to distinguish individual features. Progress was

made, however, when relativistic emission from Fe-Lα, which can be seen when the iron abundance is high [7], was observed for the first time in the NLS1 galaxy 1H0707-495 in 2009 (Fabian *et al.* 2009).

1.5.3 1H0707-495

The first *XMM-Newton* observation of 1H0707-495 (the 46 ks observation in 2000) depicts two main spectral features: a complex, soft excess below 1 keV and a sharp, deep spectral drop around 7 keV (rest frame energies). There were two main interpretations for the spectral drop; it was due to either a photoelectric absorption edge (i.e. partial covering), or the blue wing of a broadened, relativistic line (i.e. strong reflection) (Boller et at. 2002). The long (500 ks) *XMM-Newton* observation of 1H0707-495 was analyzed by Fabian *et al.* (2009). The ratio spectrum of these data (shown in Figure 1.11) to a simple model (consisting of a power law continuum, a black body and two LAOR lines) features two broad, strong emission lines. Fabian *et al.* (2009) found that the best-fit to this model yields rest frame line energies of 0.89 and 6.41 keV, inner and outer radii of 1.3 r_g and 400 r_g, respectively, and an inclination of $55.7°$. Thus, the emission lines are well described by broad iron K and L fluorescent line emission. The ratio of the data to this model, for each orbit of the *XMM-Newton* observation in 2008 is shown in Figure 1.17. While both the partial covering model and reflection model provide a good fit to the data above 3 keV, an absorber that produces the observed spectral drop would also produce other spectral features that are not seen. Additionally, different absorption models for 1H0707-495 have not been able to explain its spectral structure without needing to implement emission (Fabian *et al.* 2009, Zoghbi *et al.* 2010). Spectral variability and timing analysis, along with spectral fitting indicate that the emission is coming from the inner accretion flow and therefore give validity to the reflection model for X-ray emission in AGN.

---

[7]Fe-Lα is expected to accompany Fe-Kα, but when the iron abundance is high we see it stand out over the other elements.
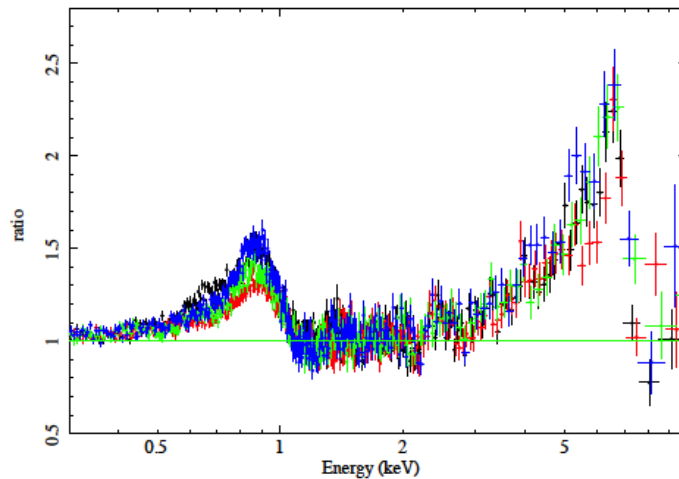
Figure 1.17: *The ratio of the data to the model, for each orbit of the XMM-Newton observation of 1H0707-495 in 2008. The model consists of a power law, black body and two* LAOR *emission lines (with normalizations set to zero). Figure from Fabian et al. (2009). Reproduced by permission.*

1.5.4   IRAS 13224-3809

Another extreme NLS1 galaxy that has a very similar X-ray spectrum to that of 1H0707-495 is the source IRAS 13224-3809. Both of these objects have large soft excesses, spectral features around 1 and $7 - 8$ keV, large iron abundances and high variability. Like 1H0707-495, IRAS 13224-3809 also has two spectral features that are well described by relativistic emission lines due to Fe-K and L fluorescence (see Figure 1.18). Previous work by Ponti *et al.* (2010) demonstrates how absorption models do not describe the observed data for IRAS13224-3809 well, as they require a very high iron abundance, and two disjoint absorbers that are not physically linked but are in a highly relativistic outflow. In addition, absorption models overpredict the absorption in soft X-rays due to Fe M fluorescence and require an additional black body component that is physically unrealistic to describe the large soft excess. Ponti *et al.* (2010) have shown that IRAS13224-3809 is closely related to 1H0707-495 with respect to spectral and variability properties, and that the reflection model provides a valid, self-consistent description of the observed data.
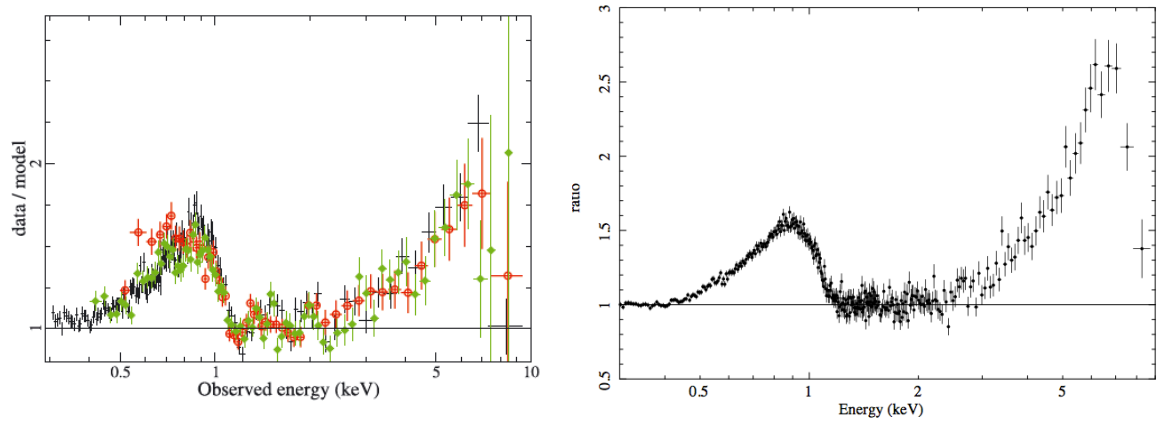
Figure 1.18: *Same as that shown in Figure 1.17, but for IRAS 13224-3809. Left Panel: Data from the* 64 ks *XMM-Newton observation in 2002 is shown in black. The red and green circles show the data from the front illuminated detectors and back illuminated CCD, respectively, on the* 200 ks *Suzaku observation of the object (taken in 2007). Figure from Ponti et al. (2010). Reproduced by permission. Right Panel: Data from the* 500 ks *XMM-Newton observation in 2011.*

1.6   A Search for Strong Fe-Lα Emitters

As mentioned in section 1.5.2, both NLS1 galaxies 1H0707-495 and IRAS 13224-3809 are strong emitters of Fe-Lα fluorescence, presumably because of high iron abundance. The equivalent width[8] (EW) of the Fe-Lα line is 180 eV and 200 eV for 1H0707-495 and IRAS 13224-3809, respectively. This leads to the following questions: Are there other extreme Type-1 AGN that exhibit strong Fe-Lα emission? Can strong Fe-Lα emission be seen in typical Seyfert 1 AGN as well? If not, why are some Type-1 AGN strong Fe-Lα emitters while others are not? To answer these questions, a search for Fe-Lα, like that observed in the NLS1 galaxies 1H0707-495 and IRAS13224-3809, was performed on a sample of nearby broad and narrow line Type-1 AGN, with redshifts ranging from 0.002336–0.918388. The model used to search for potential Fe-Lα in the sample of AGN is the same simple phenomenological model used by Fabian *et al.* (2009), consisting of a power law continuum, a black body component, and two relativistic LAOR lines (details will be discussed in

---

[8]The equivalent width is the total area in a spectral line divided by the continuum flux. More specifically, it is the width of a rectangle that has a height equal to that of the continuum and an area equal to that of the spectral feature.

Chapter 2).

This work aims to determine whether or not there is an intrinsic difference between objects that emit Fe-Lα and objects that show no Fe-Lα emission, and if so, explain what may be causing the suppression of Fe-Lα emission in certain sources. In addition, this work also aims to determine the strong Fe-L emitters that will be good candidates for reverberation mapping (see Secttion 1.4.3). The addition of Fe-Lα as a feature for studying reverberation mapping would be useful as it is difficult to perform these studies with Fe-K alone, because of the small effective area of modern telescopes at energies $E > 5$ keV, and thus another feature is needed. The combination of both Fe-L and K for such studies would allow shorter observations to be analyzed for reverberation lags, and would also allow current lags to be detected with higher significance, giving further merit to the reflection model.

This thesis beings by introducing the *XMM-Newton* Observatory, the process of data reduction and the AGN sample (Chapter 2). A description of sample properties, and Fe-Lα and Fe-Kα sources is given in Chapter 3. Analysis of strong Fe-Lα candidates is presented in Chapter 4. Conclusions and suggestions for future work are provided in Chapter 5.

Chapter 2

Observations and Data reduction

2.1 The XMM-Newton Observatory

The *European Space Agency's* (*ESA's*) *X-ray Multi Mirror* space observatory (*XMM-Newton*, Jansen *et al.* 2001) was launched in a 48 hour orbit on December 10, 1999. The Focal Plane Assembly (FPA) carries two Reflection Grating Spectrometer (RGS) readout cameras (den Herder *et al.* 2001), a European Photon Imaging Camera (EPIC) pn-CCD camera (Struder *et al.* 2001) and two EPIC Metal Oxide Semi-conductor (MOS) CCD arrays (Turner *et al.* 2001). Each of the three X-ray telescopes onboard the observatory consists of 58 Wolter I grazing-incidence mirrors that are gold-coated and nested coaxially and cofocally. This configuration allows the best possible effective area over a wide energy range. The grazing incidence angles of the mirrors range from 17 – 42 arcmin. The mirrors have a focal length of 7.5 m, and a geometrical effective area of 1500 cm^2 at 1.5 keV (Jansen *et al.* 2001). The X-ray mirrors are used to focus X-ray sources, whose spectra and images are recorded by CCDs. Each telescope has a camera at the focus, two have MOS CCDs and one has a pn-CCD.

The EPIC cameras allow sensitive imaging over an energy range of 0.15 - 12 keV, in the 30 arcmin field of view (FoV) of the telescope, with moderate spectral and angular resolution (Turner *et al.* 2001). Each EPIC CCD operates in photon counting mode with a fixed, mode dependent frame

read-out frequency. Among other things, the positions, arrival times, and energies of each event are recorded in event lists, which are tables consisting of one entry line for each received event. From these event lists, spectra, light curves, and images can be created. Since this work uses data from the EPIC pn-CCD only, we will now focus on this instrument.

As X-rays illuminate the bottom (i.e. back contact) of the detector (Figure 2.1), the charges are captured in electron potential minima, located $10 \ \mu m$ from the surface, and stored under the transfer registers. The electrons are then readout and transferred to the on-chip amplifier at the end of the CCD column.
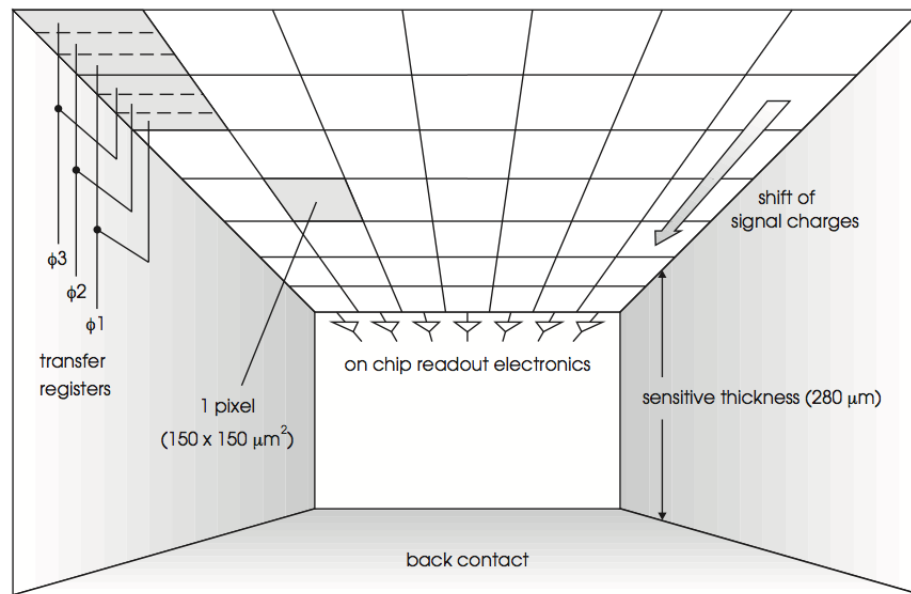
Figure 2.1: *Illustration into the interior of the pn-CCD. On-chip amplifiers are positioned at the end of each CCD line (Struder 2001). Reproduced by permission.*

The focal plane of the pn-CCD camera is composed of four quadrants, with three $3 \times 1 \ cm^2$ pn-CCDs each, operated in parallel on a single four inch silicon wafer. Each pn-CCD has 200×64 pixels, with a pixel size of $150 \ \mu m^2$ and a position resolution of $120 \ \mu m$ (Struder *et al.* 2001). The layout of the focal plane is shown in Figure 2.2. The imaging area of 36 cm^2 covers about 97% of the telescope FoV. Approximately $6 \ cm^2$ of the CCD's area is located outside the FoV and is used for instrument background studies.
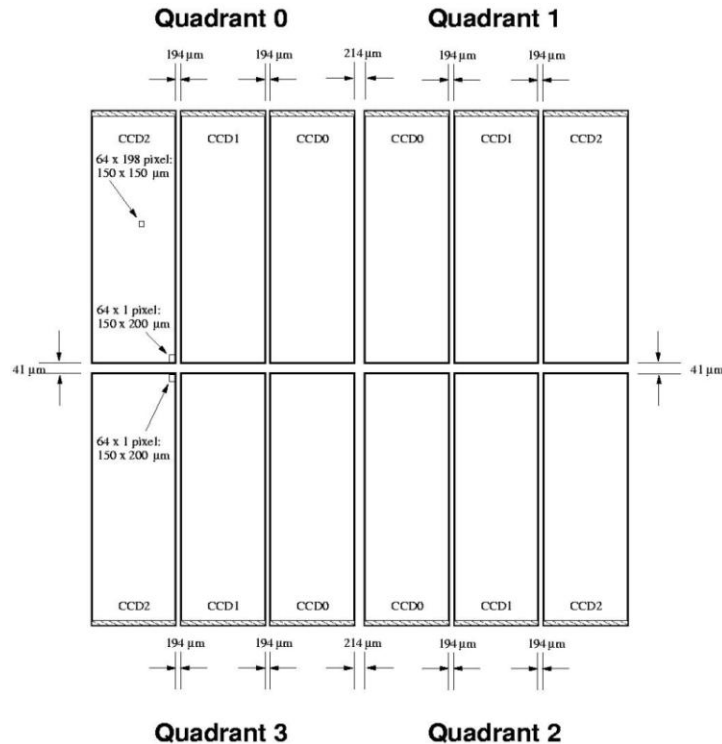
Figure 2.2: *The focal plane of the pn-CCD camera. The layout shows internal boundaries of the focal plane and the partially sensitive gaps between the CCDs and quadrants. The focal point of the telescope is CCD0 in quadrant 1 (Struder 2001). Reproduced by permission.*

The EPIC pn-CCD camera has several operating modes for data collection (shown in Figure 2.3). The full frame and extended full frame modes use all four quadrants of the focal plane. The difference between these modes is that the extended full frame mode uses a longer time for integration of the X-ray image, yielding a smaller percentage of "out-of-time events". This is useful for imaging dim extended sources. In large window mode all four quadrants are used, but only the inner half of each CCD is read out. The small window mode reads out the inner part (area of 63 pixels $\times$ 64 pixels) of CCD0 in quadrant 1, which is the part at the focal point of the telescope. In timing mode, only CCD0 in quadrant 1 is used. In this mode, a one dimensional image is constructed along the column axis, meaning that the position resolution is maintained in only one dimension. Along the row axis, data from a predefined area are formed into a one dimensional row which is rapidly read out. Finally, burst mode, which is a special case of timing mode, allows for a greater time resolution

(by transferring more pixels), but has a duty cycle of only 3% . This mode allows the brightest X-ray sources to be observed. The choice of operating mode depends on the brightness of the object and is used to mitigate pileup. Pileup occurs when a source is so bright that two or more X-ray photons hit the same pixel before it is read-out. Pileup affects the X-ray spectrum because piled-up events are registered as having higher energies. In this work we only considered objects observed in the imaging modes (i.e. not the timing mode).
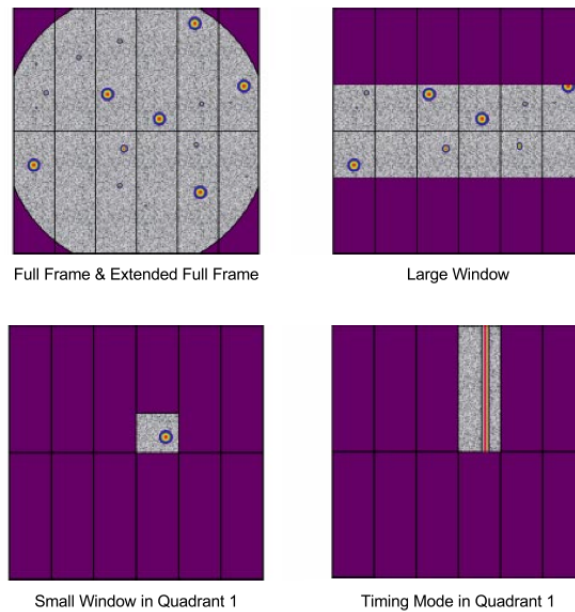
Figure 2.3: *Areas of the pn-CCD array that are read out in the various operating modes (Struder 2001). Reproduced by permission.*

2.2 Data Acquisition and Processing

The *XMM-Newton* Science Archive (XSA)[1], developed by the *XMM-Newton* Science Operations Centre (SOC), is a depository of the *XMM-Newton* science data. The XSA contains all the *XMM-Newton* raw observation data products and relevant auxiliary data necessary for reduction and analysis of the *XMM-Newton* data, which are added to the archive once the data become available

---

[1]http://xmm.esac.esa.int/xsa

to the SOC (after the proprietary period). Access to the XSA is available through a graphical user interface, which allows users to query the archive, visualize products, and retrieve science products.

Data were processed using the *XMM-Newton* Science Analysis System (SAS v12.0.1), a software package of tasks, scripts and libraries intended to reduce and analyze *XMM-Newton* science data. For a given *XMM-Newton* observation, the following data files are needed for data reduction.

- ODFs: uncalibrated, raw event files from the EPIC and other *XMM-Newton* instruments, instrument housekeeping files, radiation monitor files, and spacecraft files (these contain information on spacecraft altitude, orbit, housekeeping, and time conversion).

- CCFs: all calibration files that are valid at a particular time and for a specific observation date are organized in a CCF, which is needed to carry out the analysis of the data. For a given observation, the CCF is selected based on when the observation was made and the time of the analysis. In order to use the CCF, the information of relevant calibration files and the location of the directory containing the calibration files must be provided. This information is held in the calibration index file (CIF).

These data files can be retrieved from the XSA. The steps used for the reduction and analysis of all *XMM-Newton* data are the following.

1. Locate ODF and CCF files.

   (a) Tell SAS where to find the ODF of the observation to be analyzed, and where the CCFs are stored.

2. Create the CIF and ODF summary file.

   (a) Retrieve the observation date and select the calibration files for that time period.

   (b) Extract information from the instrument housekeeping files and calibration database, and incorporate this information into the ODF summary file.

3. Create calibrated event lists from the ODFs.

(a) Process all ODF components and create calibrated event lists for the EPIC-pn by running the SAS command EPCHAIN.

4. Filter calibrated event lists and extract source and background.

   (a) Make tables from the event lists using events that arrive in good time intervals.

   (b) Extract source photons from a circular region by specifying the spatial coordinates of the source and the radius of the circle.

   (c) Extract background photons from a circular region offset from, but close to, the source region.

   (d) Check for background flaring by looking at a histogram of counts.

      - If background flaring occurs, filter high background periods from the event list by setting upper limits on the number of counts allowed.

   (e) Check for pileup by using the SAS task EPATPLOT, which shows model distributions for single and double events without pileup. If the resulting data plot deviates from the model distribution by more than 5%, there is a strong possibility that pileup has occurred.

      - To correct for pileup, the core of the source is excised up to a radius where the pileup becomes negligible. This is done by extracting source photons from an annular region (instead of a circular region) around the centre of the source, removing more of the central region until the observed pattern distributions for single and double events are within 5% of the model distributions.

5. Extract spectra from filtered event lists and generate response files.

   (a) Create the single- and double-event pattern[2] source spectrum, using the SAS task EVSELECT, by specifying the filtered event list and the extracted source region.

   ---
   [2]Only single- and double- events (patterns 0–4) are used because only these patterns are well calibrated for spectral analysis.

(b) Create the background spectrum, using the SAS task EVSELECT, by specifying the filtered event list and the extracted background region.

(c) Scale the background region to the area of the source region, accounting for CCD gaps and bad pixels.

(d) Generate the redistribution matrix file (RMF) and the Auxiliary Response File (ARF), which are needed for spectral fitting in XSPEC[3]. The RMF and ARF can be calculated using the SAS tasks ARFGEN and RMFGEN, respectively.

6. Bin spectra.

(a) Group the source spectrum to a minimum of 20 counts per energy bin using the SAS task GRPPHA. This facilitates the use of the χ^2 minimization technique used in spectral fitting, and ensures adequate statistics in the 0.3–10 keV energy band.

Once the source spectra are binned, they can be used for spectral analysis. All spectral fitting was done by the X-ray spectral fitting program, XSPEC. The following steps outline the spectral fitting procedure.

1. Choose a parameterized model that is thought to represent the actual source spectrum.

2. Choose initial values for the model parameters.

3. Use XSPEC to predict the spectrum that would be detected for such a model.

4. Use a χ^2 minimization technique to find the values of the model parameters that give the best-fit between the theoretical model and the observed spectrum. These parameter values are called the "best-fit parameters", and the model made up of these parameters is known as the "best-fit model".

---

[3]The EPIC detector response function is required by XSPEC to simulate the output spectrum observed by EPIC. The response function gives the probability that an incoming photon of energy E will be detected in the corresponding channel. The ARF gives the effective area as a function of energy.

5. Evaluate the calculated χ^2 fit statistic to determine how well the model explains the observed data.

2.3 Sample Selection and Criteria

The sample used in this work comes from a combination of three catalogues, namely, the Catalogue of AGN in the *XMM-Newton* Archive (CAIXA, Bianchi *et al.* 2009), the sample of soft X-ray selected AGN by Grupe *et al.* (2004), and the QSOs in the Bright Quasar Survey (BQS) catalogue by Boronson & Green (1992).

2.3.1 CAIXA

The CAIXA catalogue consists of all radio-quiet, unobscured ($n_H < 2 \times 10^{22}$ cm^{-2} in X-rays) AGN observed by *XMM-Newton* in targeted observations, whose data were public by March 2007 (no further updates have been made to this catalogue). AGN with less than 200 counts in the energy bands of $0.5 - 2$ and $2 - 10$ keV were excluded, as well as spectra with pileup larger than 1%. After applying these criteria, 156 objects remain in the catalogue. Of these 156 objects, 77 are quasars and 79 are Seyfert galaxies, where 21 of the Seyfert galaxies are NLS1s, 30 are BLS1s, and the remaining 28 are 'other' (i.e. unclassified). The redshift of the objects range from z = 0.002 − 4.520.

2.3.2 Soft X-ray selected AGN

The sample described by Grupe *et al.* (2004) includes all bright soft X-ray *ROSAT All-Sky Survey (RASS)* AGN from Thomas *et al.* (1998) with the following criteria applied:

1. Mean *RASS* Position Sensitive Proportional Counter (PSPC) count rate ≥ 0.5 cts/s

2. Hardness ratio[4] < 0.00

3. Galactic latitude $|b| > 20°$

---

[4]The hardness ratio is defined as HR = (hard-soft)/(hard + soft) with soft energies from $0.1 - 0.4$ keV and hard energies from $0.5 - 2.0$ keV.

Criterion 1 was applied to ensure a sufficient number of X-ray photons, during the average RASS time coverage (200 – 400 s) to allow spectral analysis. Criterion 2 was imposed to guarantee a soft X-ray spectrum. Criterion 3 ensures that the X-ray spectrum is not hardened by Galactic extinction. Applying these criteria, Thomas *et al.* (1998) found 397 sources, where 113 are AGN (excluding BL Lac objects). From this sample of 113 AGN, Grupe *et al.* (2004) excluded three known transient sources, resulting in a total of 110 objects. The sample of 110 sources consists of 51 NLS1s and 59 BLS1s.

2.3.3   PG Quasars

The sample defined by Boronson & Green (1992) contains all objects in the BQS catalogue (Schmidt & Green 1983) that have $z < 0.5$. Boronson & Green (1992) also excluded two objects, one because it does not have broad lines, and one because the correct redshift is greater than 0.5. This yields a total of 87 objects.

2.3.4   Selection Criteria

Combining the three samples discussed above yields an initial sample of 353 objects of which, 108 are NLS1s, 191 are BLS1s, and 54 are unclassified. This sample was reduced by only including objects with PN data in the *XMM-Newton* archive. To avoid possible absorption, only Type 1 – 1.5 AGN were selected. In addition, objects with column density $n_H > 1 \times 10^{21} \text{cm}^{-2}$ were excluded because a clear view of the $E > 0.3$ keV region is needed. Finally, the three samples were cross-referenced to eliminate double or triple counts of the same *XMM-Newton* observation. This resulted in a sample with 297 observations. Finally, during the data reprocessing (see Section 2.2), objects that had no detectable source on the pn-CCD, were excluded. The final sample consists of 202 observations (154 unique objects), of which 67 are NLS1s and 113 are BLS1s[5]. Table 2.1 provides a list of the unique sources. Where more than one observation of an object is available, the observation with the best signal-to-noise ratio is listed.

---

[5]The remaining 22 objects have no recorded $FWHM_{H\beta}$ and hence cannot be classified as NLS1 nor BLS1.

Table 2.1: Log of Observations (abridged)

Object Name	Observation ID	Start Date	Duration (ks)	GTI Exposure (ks)
B21128+31	0102040201	Nov. 22, 2000	24.61	15.61
TonS180	0110890401	Dec. 14, 2000	31.05	20.62
Mrk1044	0112600301	Jul. 23, 2002	8.38	5.55
1H0419-577	0112600401	Dec. 04, 2000	9.56	5.72
RXJ0323.2-4931	0140190101	Aug. 16, 2003	29.61	24.91
NGC 985	0150470601	Jul. 15, 2003	57.95	39.79
NGC 4051	0157560101	Nov. 22, 2002	51.87	45.82
ESO359-G19	0201130101	Mar. 09, 2004	24.44	16.8
H0439-272	0301450101	Aug. 13, 2005	20.52	13.93
Fairall 1116	0301450301	Aug. 28, 2005	20.52	14.05
QSO0056-363	0401930101	Nov. 26, 2006	47.11	41.39
RXJ1034.6+3938	0506440101	May 31, 2007	93.21	76.99
PG 0157+001	0101640201	Jul. 29, 2000	14.77	6.59
PG 0844+349	0103660201	Nov. 04, 2000	26.41	13.49
PG 1202+281	0109080101	May 30, 2002	17.92	12.86
PG 1048+342	0109080701	May 13, 2002	33.18	27.53
PG 1114+445	0109080801	May 14, 2002	43.51	37.50
PG 1307+085	0110950401	Jun. 13, 2002	13.97	10.84
PG 0947+396	0111290101	Nov. 03, 2001	21.98	17.55
PG 0953+414	0111290201	Nov. 22, 2001	15.57	11.53
PG 1115+407	0111290301	May 17, 2002	21.12	15.03
PG 1216+069	0111291101	Dec. 18, 2002	16.95	14.03
PG 1211+143	0502050101	Dec. 21, 2007	64.87	45.53
PG 1004+130	0140550601	May 04, 2003	22.21	18.08
3C 249.1	0153210101	Nov. 01, 2002	23.02	9.98
PG 0921+525	0201130501	Nov. 15, 2004	47.42	32.86
PG 1116+215	0111290401	Dec. 02, 2001	10.19	5.55
PG 1011-040	0202060101	May 08, 2005	31.92	24.53
PG 1126-041	0202060201	Dec. 31, 2004	33.82	29.06
⋮	⋮	⋮	⋮	⋮

The names, observation IDs, start dates, durations, and GTI exposure times of the unique objects in the AGN sample. This is a sample table showing the first several entries. The full table is shown in Appendix A.

Chapter 3

Sample Characteristics

As high energy X-ray photons (E $\geq$ 7 keV) irradiate the accretion disk, they eject electrons in the K-shell (n = 1) of iron in the disk via photoelectric absorption. Fe-Kα fluorescence occurs when an Fe ion de-excites as an electron from the L-shell (n = 2) drops down to fill the vacancy in the K-shell. The excess energy is emitted as a Fe-Kα photon. This process is depicted in Figure 3.1. When a vacancy exists in the L-shell of an Fe ion, either by Fe-Kα fluorescence or photoelectric absorption, an electron from the M-shell drops down to fill the vacancy in the L-shell. This process is known as Fe-Lα fluorescence, because the excess energy is emitted as a Fe-Lα photon (see Figure 3.1).

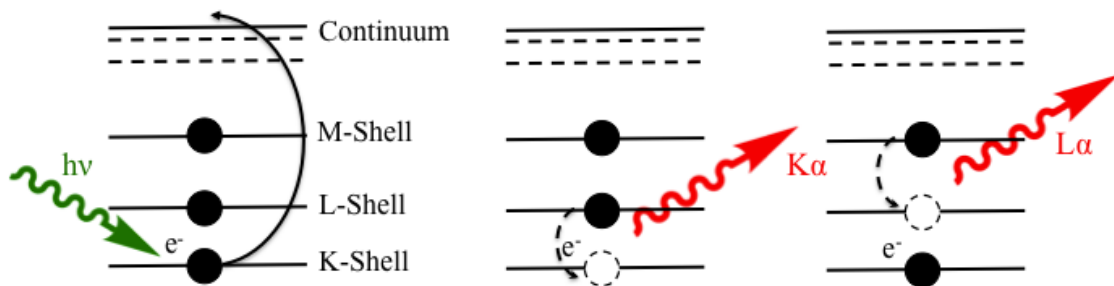The energy of the Kα photon of iron ranges from 6.4 keV – 6.97 keV, increasing from neutral

Figure 3.1: *Left Panel: Photoelectric absorption by an incoming X-ray photon. Middle Panel: Fe-Kα fluorescence, produced when an L-shell electron drops down to the lower energy K-shell. Right panel: An M-shell electron drops down to the L-shell, emitting Fe-Lα fluorescence.*

iron (Fe I) to the highest ionization stage (Fe XXVI) (Kallman 1995). The energy of the Lα photon

of iron ranges from 0.7 keV – 1.2 keV, increasing with higher ionization stages (Kallman 1995). The

ratio of the Fe-Lα line flux to that of the Fe-Kα line has no lower limit, however, it has a maximum

value of ~ 1.6 for an accretion disk with a column density of $10^{23.5}$ cm^{-2} and $\xi \approx 1,000$ erg cm

s^{-1}. The ratio can be as large as ~ 80 for an accretion disk with a column density of $10^{20.0}$ cm^{-2}

and $\xi \approx 10$ erg cm s^{-1}. This upper limit arises because the conditions required for efficient Fe-Lα

production are inconsistent to those required for efficient Fe-Kα production (Kallman 1995).

As noted in Section 1.6, it is useful to find strong Fe-Lα emitters in addition to 1H0707-495 and

IRAS 13224-3809. A search for simultaneous Fe-Lα and Fe-Kα emission was performed on the

AGN sample described above in Section 2.3. This was done by applying the same phenomenological

model used by Fabian *et al.* (2009) to detect simultaneous Fe-Lα and Fe-Kα in 1H0707-495 to the

spectra in the AGN sample. The model consists of a black body component (BLACK BODY in

XSPEC), a power law component (POWER LAW in XSPEC), and two broad accretion disk emission

line components (LAOR profiles in XSPEC). The black body component is used to model the soft

excess (see Section 1.2.2), the power law is used to model the primary X-ray emitter, and the LAOR

profiles are used to model possible relativistic Fe-Kα and Fe-Lα lines. The LAOR profiles are narrow

Gaussian profiles that are broadened by the effects discussed in Section 1.4.1, that is, the motion of

the accretion disk and the relativistic effects in the vicinity of the black hole. The model parameters

of the LAOR profiles are the emission line energy (E), the power law disk emissivity index (q) (i.e.

the power law dependence of the emissivity, which scales as r^{-q}, where r is the radial distance of

the point of emission from the X-ray source), the inner and outer accretion disk radii (r_{in} and r_{out}

in units of r_g), the disk inclination (i in degrees), and the flux of the emission line (norm). The

model parameters of the BLACK BODY component are the temperature (kT in units of keV), and the

normalization of the component in units of photons keV^{-1} cm^{-2} s^{-1}. The model parameters of the

POWER LAW component are the photon index, Γ, (see Section 1.3.3), and the normalization. The

power law plus black body model is a crude approximation of the continuum emission. However,

when the two LAOR profiles are included, a significant improvement is achieved for the spectral fits.
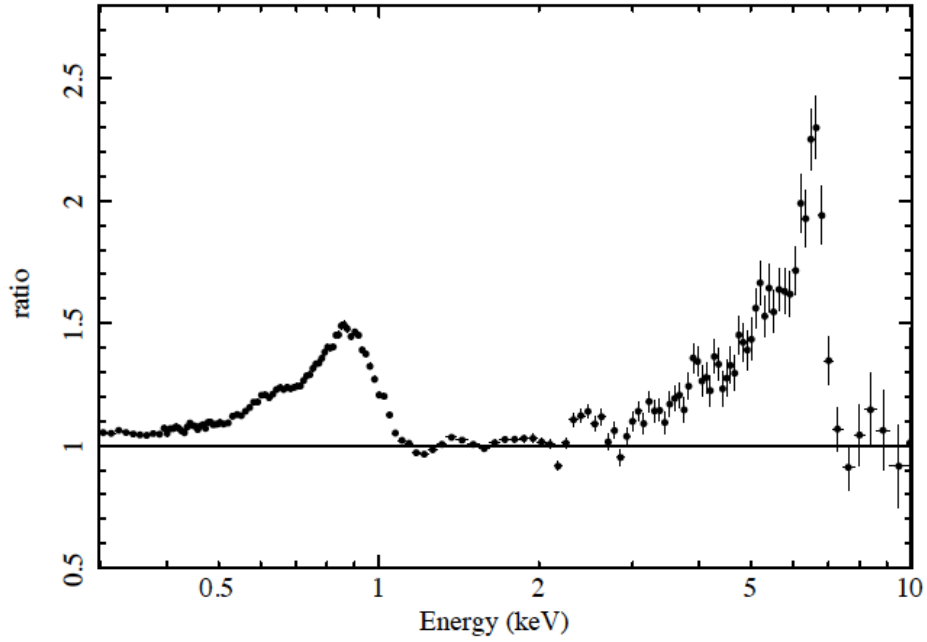
Figure 3.2: *Residuals obtained by fitting the phenomenological model to the 2008, $\sim 500\ ks$ observation of 1H0707–495, after setting the normalizations of the* LAOR *lines to zero. Figure from Fabian et al. (2009). Reproduced by permission.*

The energies of the two profiles are ~ 1 keV and $E \sim 6$ keV. Figure 3.2 shows the residuals of the model fitted to the 2008 observation of 1H0707–495, after setting the normalizations of the LAOR lines to zero.

Since the Fe-Lα and Fe-Kα lines are expected to originate from the same region of the accretion disk, the blurring parameters of the two LAOR components (i.e. r_{in}, i, and q) are linked. The fit is not very sensitive to the outer disk radius (r_{out}) so this parameter is fixed to the maximum value of $400\ r_g$. This model is devised to find candidate strong relativistic Fe-Lα emitters. By fitting this model to the spectra in our AGN sample, the energies of the relativistic Fe-Lα and Fe-Kα lines can be determined, as well as the EWs and fluxes of the LAOR model components. The values of the energies can then be compared to the expected values for Fe-Lα and Fe-Kα, and the flux ratio can be compared to that expected from theory (Kallman 1995). In this way, we hope to determine if an object is a candidate for simultaneous Fe-Lα and Fe-Kα emission. A good fit ($\chi^2_\nu \sim 1$) was obtained

for all observations. Objects with the following criteria were rejected as candidates for simultaneous Fe-Lα and Fe-Kα emission.

- Fe-Lα line energy significantly outside the acceptable range of E = 0.7 − 1.2 keV

- Fe-Kα line energy significantly outside the acceptable range of E = 6.40 − 6.97 keV

- Flux consistent with zero (within 2.7 σ)

Thus, a significant Fe-Lα or Fe-Kα detection requires both a consistent energy and a non-zero line normalization for that feature. The data to model ratio plots, like that shown in Figure 3.2, for all unique objects are shown in Appendix B.

After finding candidates for strong Fe-Lα emitters, it is important to asses the statistical significance of the components because the addition of the Fe-Lα and Fe-Kα LAOR lines may not have significantly improved the model. In addition, because the continuum is not modelled properly, the LAOR line energies may not correspond exactly to the expected values. Since we are looking for strong Fe-Lα emitters, we only want to consider objects with both Fe-Lα and Fe-Kα emission or objects with only Fe-Lα emission. Objects with only Fe-Lα emission are included because it is possible that Fe-Lα is present in these objects, even without the detection of Fe-Kα. It is possible that the Fe-Kα feature is not detected because of the higher statistics in the lower energy range, or softer spectra in the $0.3 − 10$ keV band could make it difficult to detect Fe-Kα, especially for low signal-to-noise (S/N) observations.

Once the phenomenological model was applied, the sample was divided into four smaller subsamples based on the detections of Fe-Lα and Fe-Kα, namely: group A, objects with significant detection of only Fe-Kα; group B, objects with significant detections of both Fe-Lα and Fe-Kα; group C, objects with significant detection of only Fe-Lα; and group D, objects with no significant detections of either line. Objects found in group A likely have harder spectra in the $0.3 − 10$ keV band, which produces stronger Fe-Kα emission relative to Fe-Lα, and/or relatively high S/N in the Fe-Kα energy band. Objects in group B likely have high reflection fractions (see Section 4.2) and/or

high iron abundances or high S/N. Objects in group C likely have softer spectra in the $0.3 - 10$ keV band, which produces stronger Fe-Lα emission relative to Fe-Kα, and/or relatively high S/N in the Fe-Lα energy band or high iron abundances. Objects in group D likely have low reflection fractions and/or low S/N. These four samples are summarized in Table 3.1.

To determine if the detections of Fe-Lα and Fe-Kα in the B and C samples were statistically significant at the 3σ level, we checked if the addition of the Fe-Kα and Fe-Lα LAOR components to the continuum model improved the fit, based on the number of parameters added (i.e. the change in degrees of freedom, $\Delta\nu$) and the change in χ^2 ($\Delta\chi^2$). The addition of one LAOR line component adds 5 parameters to the continuum model (BLACK BODY + POWER LAW), thus the change in degrees of freedom is $\Delta\nu = 5$. Therefore, looking at a χ^2 distribution table, $\Delta\nu = 5$ requires $\Delta\chi^2 \geq 18.21$ for the addition of the LAOR component to improve the continuum model fit at the 3σ level. The addition of a second LAOR line component only adds 2 more parameters (since the blurring parameters between the LAOR components are linked) to the BLACK BODY + POWER LAW + LAOR model, thus the change in degrees of freedom is $\Delta\nu = 2$. Therefore, $\Delta\nu = 2$ requires $\Delta\chi^2 \geq 11.83$

for the addition of the second LAOR component to improve the model fit at the 3σ level.

We now define $\Delta\chi^2$ (Fe-Kα) as the change in χ^2 after adding a Fe-Kα LAOR component to the continuum model, $\Delta\chi^2$ (Fe-Lα) as the change in χ^2 after adding a Fe-Lα LAOR component to the continuum model, and $\Delta\chi^2(K\alpha - L\alpha)$ as the change in χ^2 after adding a Fe-Lα LAOR component to the BLACK BODY + POWER LAW + LAOR $_{Fe\text{-}K\alpha}$ model. Since the B sample includes detections of simultaneous Fe-Lα and Fe-Kα, both $\Delta\chi^2$ (Fe-Kα) ≥ 18.21 and $\Delta\chi^2(K\alpha - L\alpha) \geq 11.83$ are required for 3σ detections of the features. Since the C sample only requires significant detection of Fe-Lα, only $\Delta\chi^2$ (Fe-Lα) ≥ 18.21 is required for 3σ detection of the feature.

As mentioned in the previous section, assuming an accretion disk with a column density of $10^{23.5}$ cm^{-2} and $\xi \approx 1,000$ erg cm s^{-1}, the ratio of the Fe-Lα line flux to that of the Fe-Kα line has a maximum value of ~ 1.6. The flux ratio, $F_{Fe\text{-}L\alpha}$ / $F_{Fe\text{-}K\alpha}$, for objects in the B sample was compared to the expected ratio range to determine if an object is a candidate for simultaneous Fe-Lα

and Fe-Kα emission. Objects with an inconsistent flux ratio were considered non-detections. This criterion was not applied to objects in the C sample because only Fe-Lα detection is required and the expected flux ratio range assumes detection of both Fe-Lα and Fe-Kα.

Therefore, objects with the following criteria were excluded from the B sample.

- $\Delta\chi^2$ (Fe-Kα) < 18.21

- $\Delta\chi^2(K\alpha - L\alpha) < 11.83$

- $F_{Fe\text{-}L\alpha}$ / $F_{Fe\text{-}K\alpha} > 1.6$

Objects with the following criterion were excluded from the C sample.

- $\Delta\chi^2$ (Fe-Lα) < 18.21

The number of objects in samples A, B, C, and D are 17, 54, 11, and 24, respectively. Table 3.1 shows the energies, equivalent widths, equivalent width ratios and flux ratios of the LAOR lines with significant Fe-Lα and/or Fe-Kα detections.

Although the phenomenological model provides a good fit to the spectrum, it only approximates the continuum emission and it does not take into account all spectral features. For example, we do not expect that the emission peaks arise from single lines, but from line and absorption edge complexes in the reflection spectrum. However, the model is sufficient to find candidate Fe-Lα and Fe-Kα emitters, and the parameters obtained with this model can be used as a guide for more realistic reflection models that will be discussed in Section 4.2.

The average values of the Fe-Lα and Fe-Kα energies and equivalent widths are compared between the different types of AGN in our sample, namely the NLS1, BLS1, and 'other' objects (Table 3.2). On average, the EW for both Fe-Lα and Fe-Kα are higher for NLS1s. However, the average ratio of EW(Fe-Lα) / EW(Fe-Kα) is approximately the same for NLS1s and BLS1s. The Fe-Lα and Fe-Kα LAOR line energies are also approximately the same for NLS1s and BLS1s.

Table 3.1: Sample Properties

Group	Description	$< E_L >$	σ	$< EW_L >$	σ	$< E_K >$	σ	$< EW_K >$	σ	$< \frac{EW_L}{EW_K} >$	σ	$< \frac{F_{Fe-L\alpha}}{F_{Fe-K\alpha}} >$	σ
A	significant Fe-Kα detection but no significant detection of Fe-Lα					6.72	0.64	1.30	1.95				
B	significant detections of both Fe-Lα and Fe-Kα	0.98	0.16	0.06	0.05	6.54	0.31	1.08	1.03	0.14	0.35	0.95	0.82
C	significant Fe-Lα detection but no significant detection of Fe-Kα	0.95	0.30	0.15	0.14								
D	no significant detection of Fe-Lα nor Fe-Kα												

Average values and standard deviations of the energies (in keV), EWs (in keV), EW ratio and flux ratio of the LAOR lines for objects with significant Fe-Lα and/or Fe-Kα detections. A description of each sample is also provided.

Table 3.2: NLS1 and BLS1 properties

Classification	$< E_L >$	σ	$< EW_L >$	σ	$< E_K >$	σ	$< EW_K >$	σ	$< \frac{EW_L}{EW_K} >$	σ
NLS1	0.95	0.16	0.07	0.05	6.49	0.35	1.47	1.44	0.04	0.03
BLS1	1.01	0.15	0.06	0.06	6.54	0.29	0.85	0.49	0.05	0.01
'other'	1.12	0.52	0.05	0.05	6.68	0.44	0.68	0.67	0.07	0.04

Average values and standard deviations of Fe-Lα and Fe-Kα energies (in keV), equivalent widths (in keV), and equivalent width ratio for the NLS1, BLS1, and 'other' objects.

Chapter 4

Analysis and Discussion

4.1 Distinguishing Absorption and Reflection

An alternative hypothesis to the blurred reflection model is the absorption model, which posits that the Fe-Lα feature is actually an effect of the continuum being absorbed by warm absorbers. In some cases, both an Fe-Lα line and an absorption edge can provide acceptable fits to the same spectrum, depending on how the power law is modelled. If a flat power law slope is chosen, an absorption edge may adequately fit the Fe-Lα feature. Alternatively, if a steep value for the power law slope is chosen, the Fe-Lα feature can be described by a relativistic emission line. For example, both an absorption edge and a LAOR line can be fit equally well to the 2000 observation of 1H0707–495 (obs ID: 0110890201, GTI exposure: 36ks), as shown in Figures 4.1 and 4.2. However, this degeneracy can be broken by acquiring higher S/N observations. For example, fitting an absorption edge to the Fe-Lα feature in the January 2008, 500ks 1H0707–495 observation (obs ID: 0511580201) instead of a LAOR line does not yield an acceptable fit, as shown in Figures 4.3 and 4.4. Even though all the objects in our sample (Chapter 3) can be fitted with a LAOR profile, we can only dismiss a possible warm absorption origin in objects with sufficiently high S/N data.

Because both absorption and reflection models can explain the Fe-Lα feature in some objects, it is important to determine which objects have a reasonable probability of distinguishing between
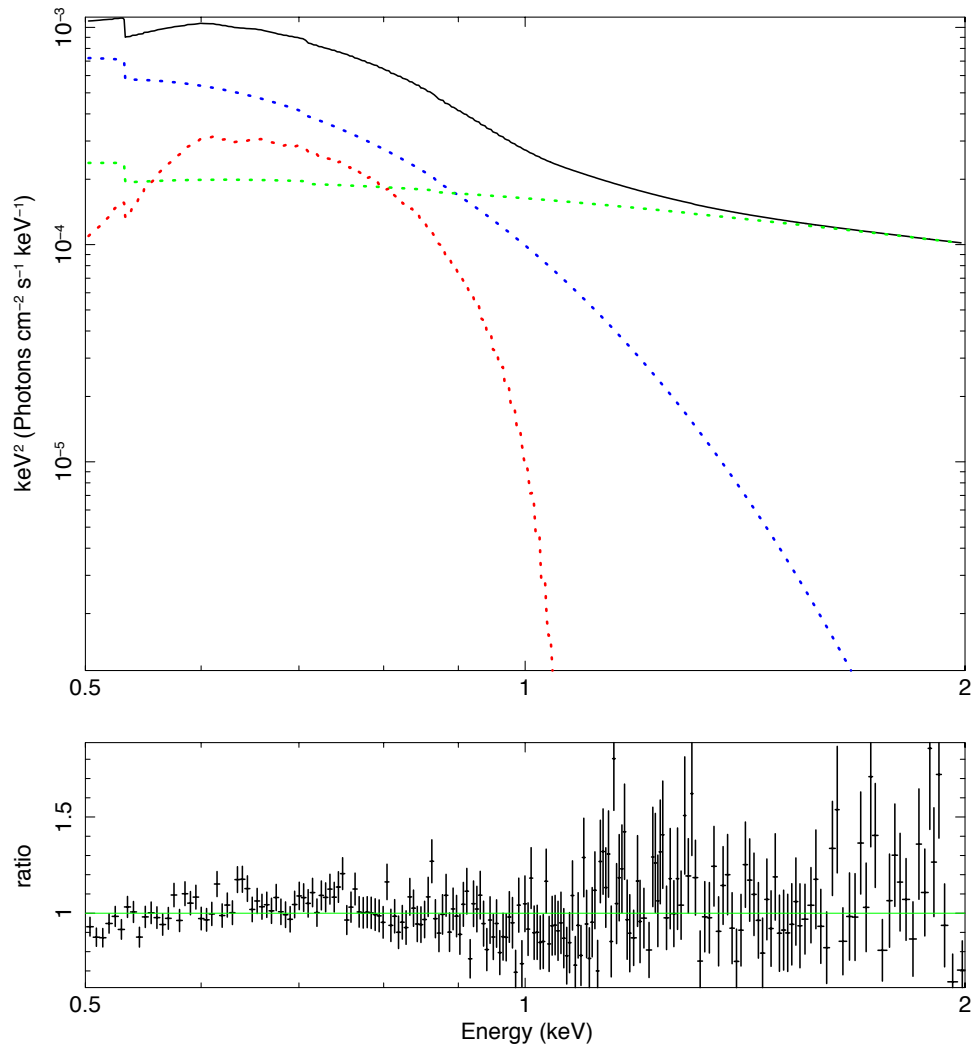
Figure 4.1: *Top panel: The 0.5 – 2.0 keV region of the 2000 1H0707–495 observation. The 0.5 – 2.0 keV region is fit with a* LAOR *line and the model components are shown. The* LAOR *line is shown in red, the black body component is shown in blue, the power law component is shown in green, and the total model is shown in black. Bottom Panel: The data to model ratio with error bars of 1σ.*
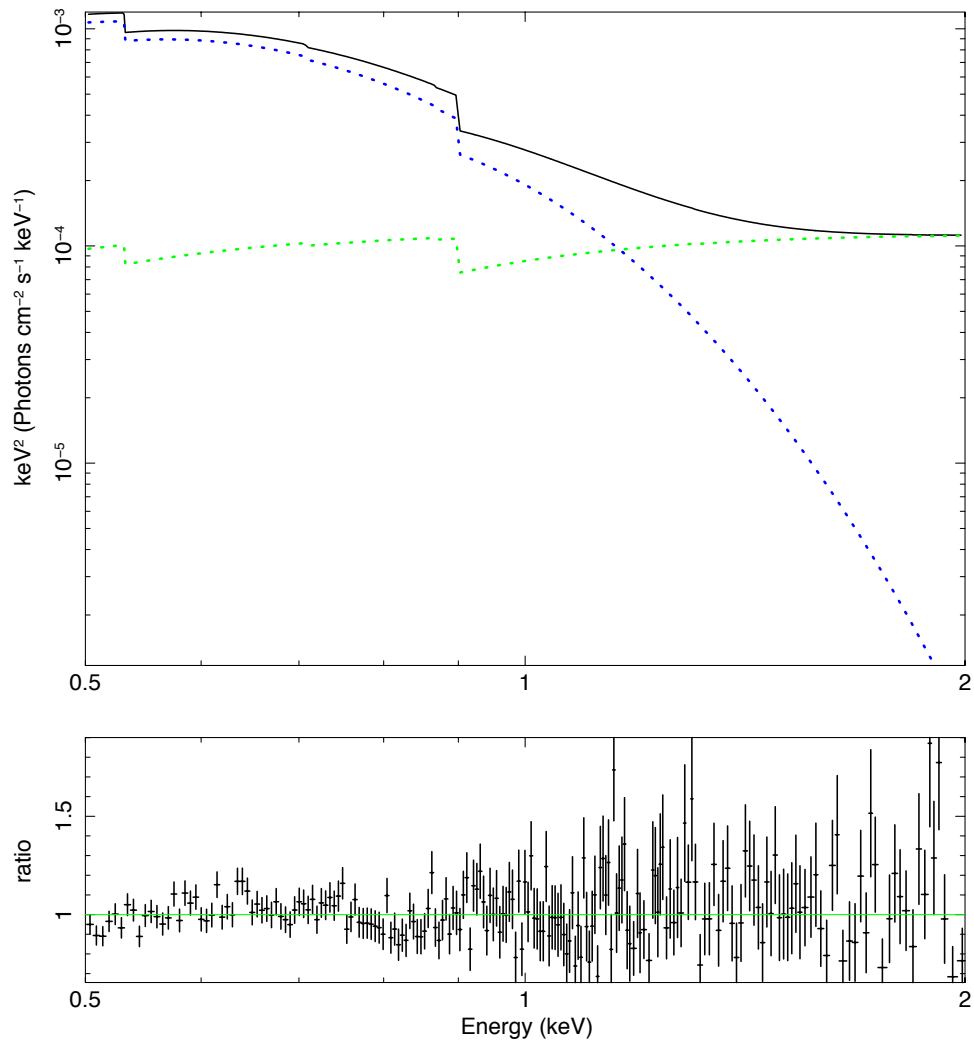
Figure 4.2: *Top panel: The 0.5 – 2.0 keV region of the same 1H0707–495 observation shown in Figure 4.1. The 0.5 – 2.0 keV region is fit with an absorption edge instead of a* LAOR *line and the model components are shown. The black body component is shown in blue, the power law component is shown in green, and the total model is shown in black. Bottom Panel: The data to model ratio with error bars of 1σ.*
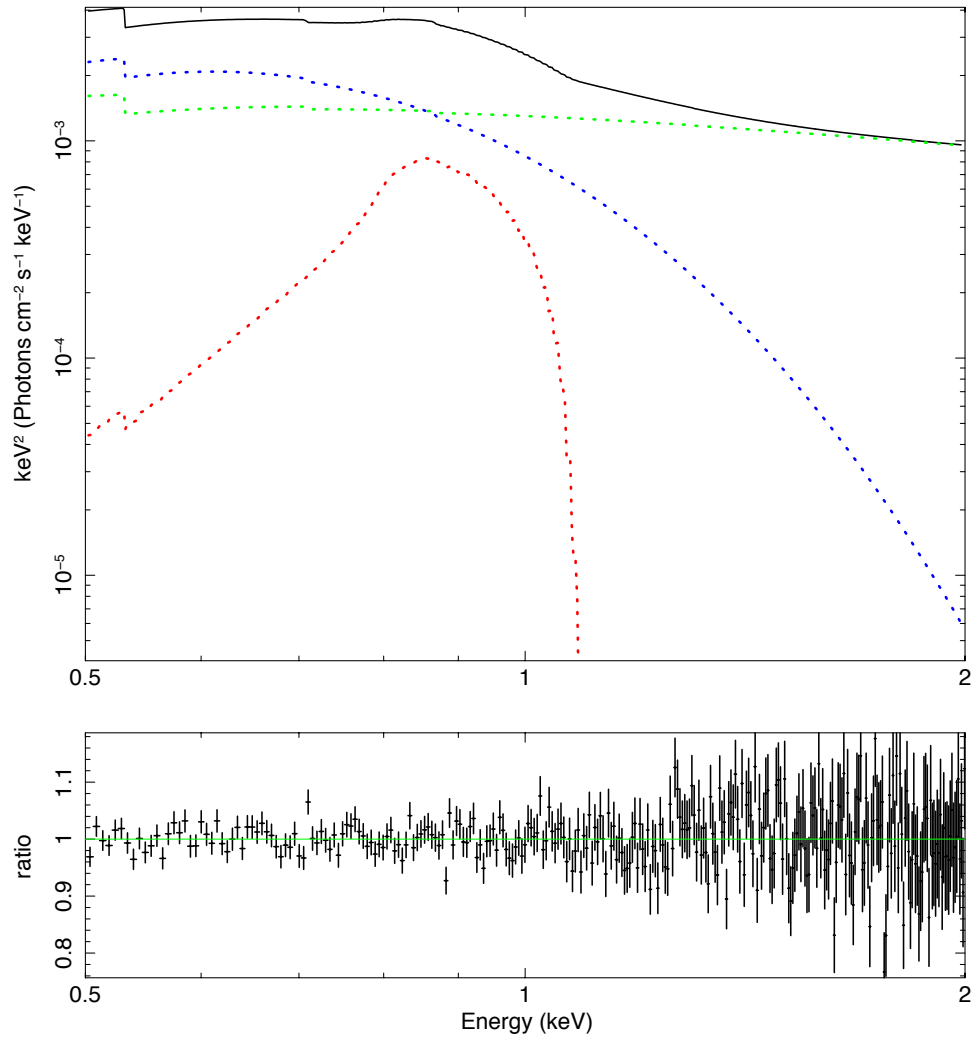
Figure 4.3: *Same as Figure 4.1, but for the 2008, 500 ks 1H0707–495 observation.*
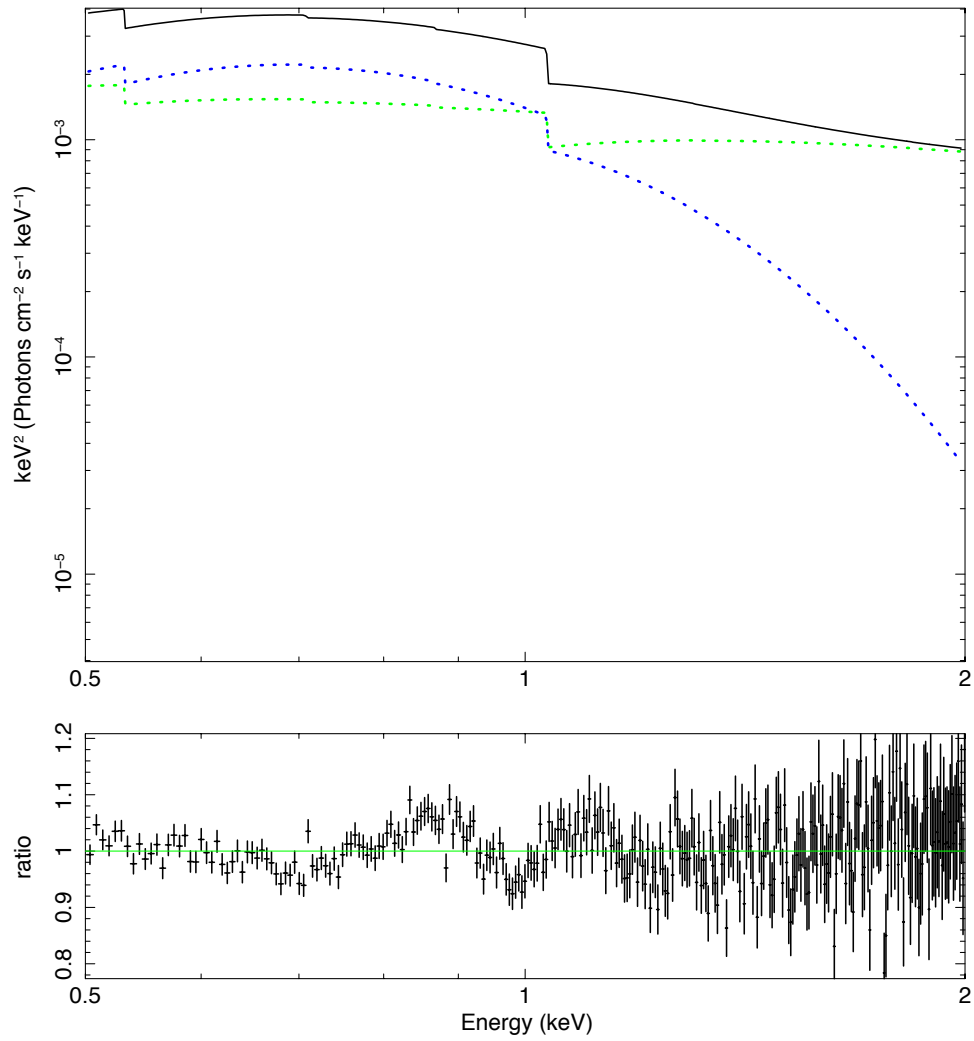
Figure 4.4: *Same as Figure 4.2, but for the 2008, 500ks 1H0707–495 observation. In the bottom panel, an excess in residuals can be seen at $\sim 0.9 \; keV$. This is because the absorption edge cannot adequately describe the Fe-Lα feature.*

reflection and absorption. The probability of distinguishing between these models is dictated by both the strength of the Fe-Lα feature and the number of counts in the spectrum. To determine the objects in which reflection can likely be differentiated from absorption, multiple simulations of the Fe-Lα line in 1H0707-495 were performed, using the XSPEC task FAKEIT, with varying strength and exposure times. These simulations were then used to produce a grid. The FAKEIT task requires the response files and a model to generate the spectrum that would be observed by convolving that model with the response files, assuming the exposure time as specified by the user. Starting from the phenomenological model described in Section 3, the strength of the Fe-Lα feature was varied to the desired value by changing the EW of the LAOR profile. To change the EW of the LAOR profile, the normalization and photon index of the power law component and the normalization of the Fe-Lα LAOR line were varied, while keeping the ratio between the Fe-Lα line to the Fe-Kα line constant. Four models, with the same components as the phenomenological model, were generated in this manner, each with a different Fe-Lα EW value. The four models have Fe-Lα EW values of 0.06, 0.10, 0.20 and 0.30 keV.

These models were then used to carry out the spectral simulations. The simulations were performed using the RMF and ARF files of the July 2007 1H0707-495 (obs ID: 0511580401 GTI exposure: 34 ks). Throughout all simulations, the flux from 0.3 – 10 keV was held constant. Before performing the simulations, a test simulation was completed on each model to determine the predicted model count rate from 0.5 – 2.0 keV. From the count rate, the exposure time needed to obtain a specific number of counts can be determined from the formula *count rate = number of counts / exposure time*. For each of the four EW models, four simulations were performed with different exposure times, resulting in a total of 16 simulations. The values of the exposure times were chosen to obtain photon counts between 0.5 – 2.0 keV of 10^3, 10^4, 10^5, and 10^6 counts. The number of counts is used to represent the S/N because higher S/N is usually achieved with a higher number of source counts. The range 0.5 – 2.0 keV is considered because this is the region where Fe-Lα is present. The simulated data represent the spectra that would be obtained from an *XMM-Newton* observation for an object with an Fe-Lα line of a specific EW and a specific number

of counts in the 0.5 – 2.0 keV range.

To determine the EW needed to distinguish Fe-Lα from an absorption edge, given a certain number of counts, each simulated spectrum was fit to both the phenomenological model and an absorption edge model, ZEDGE $\times$ (BLACK BODY + POWER LAW), in the 0.5 – 2.0 keV range. Model parameters of the ZEDGE component are the line energy (E in keV), the optical depth (τ), and the redshift. The spectral fit was considered statistically significant at the 3σ level if the given null hypothesis probability of the fit was less than, or equal to 0.003 (i.e. $p(H_0 \leq 0.003)$). Therefore, if the null hypothesis probability shows that the fit is statistically significant for both models, it is not possible to differentiate between Fe-Lα emission and an absorption edge, for that tested EW and S/N combination. Note that the Fe-Lα model fit will always be statistically significant because the same model used to generate the simulated spectrum is being fitted to the simulated data. From this procedure, we found that for 10^3 and 10^4 counts, an $EW \geq 0.3$ keV is needed to distinguish the features; for 10^5 counts, an $EW \geq 0.06$ keV is needed; and for 10^6 counts, we can attempt to distinguish features with $EW < 0.06$ keV. As expected, with higher S/N data, weaker Fe-Lα emission can be detected.

Next, the EW needed to distinguish between a LAOR line and an absorption edge for specific values of the number of counts was determined. The minimum values needed to differentiate between the two features for seven values of the EW and the corresponding number of counts between 0.5 – 2.0 keV are given in Table 4.1. Connecting these points results in a boundary that indicates the EW values needed in an *XMM-Newton* observation with a given number of counts to distinguish an Fe-Lα line from an absorption edge at the 3σ level. Figure 4.5 shows this boundary with ratio plots of the 16 simulated spectra fitted with an absorption edge in the $0.5 - 2.0$ keV range. Figure 4.6 shows the boundary plotted over the objects in the B and C samples. The area above this line is the parameter space where we have the highest probability of distinguishing Fe-Lα emission from absorption. This parameter space does not exclude the existence of a warm absorber (see Section 1.2.1). However, it allows the origin of the Fe-Lα profile to be differentiated from an absorption edge.
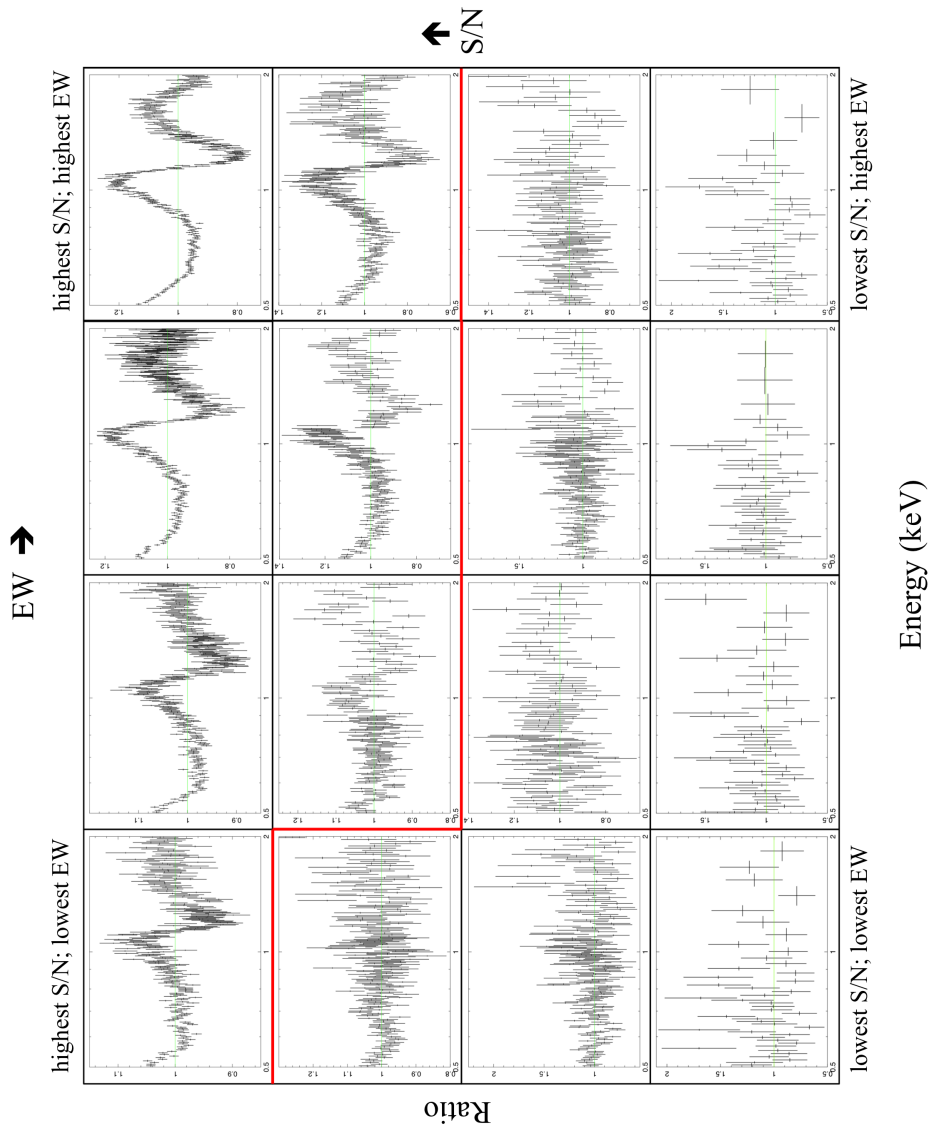
Figure 4.5: *Ratio plots of the sixteen simulated spectra fitted in the 0.5 − 2.0 keV range with an absorption edge. Each row represents one S/N value, with the lowest at the bottom. Each column represents one EW value, with the lowest at the left. The 3σ boundary, which delineates significant detection, is outlined by the red line.*

Table 4.1: 3σ Boundary in the Counts - EW Plane

Number of Counts (.5–2 keV)	Equivalent Width (keV)
1.0×10^3	0.530
1.0×10^4	0.350
3.0×10^4	0.250
1.0×10^5	0.085
3.0×10^5	0.053
1.0×10^6	0.053
2.0×10^6	0.035

The EW needed, for a given number of counts, to differentiate between a LAOR *profile and an absorption edge in an XMM-Newton observation.*
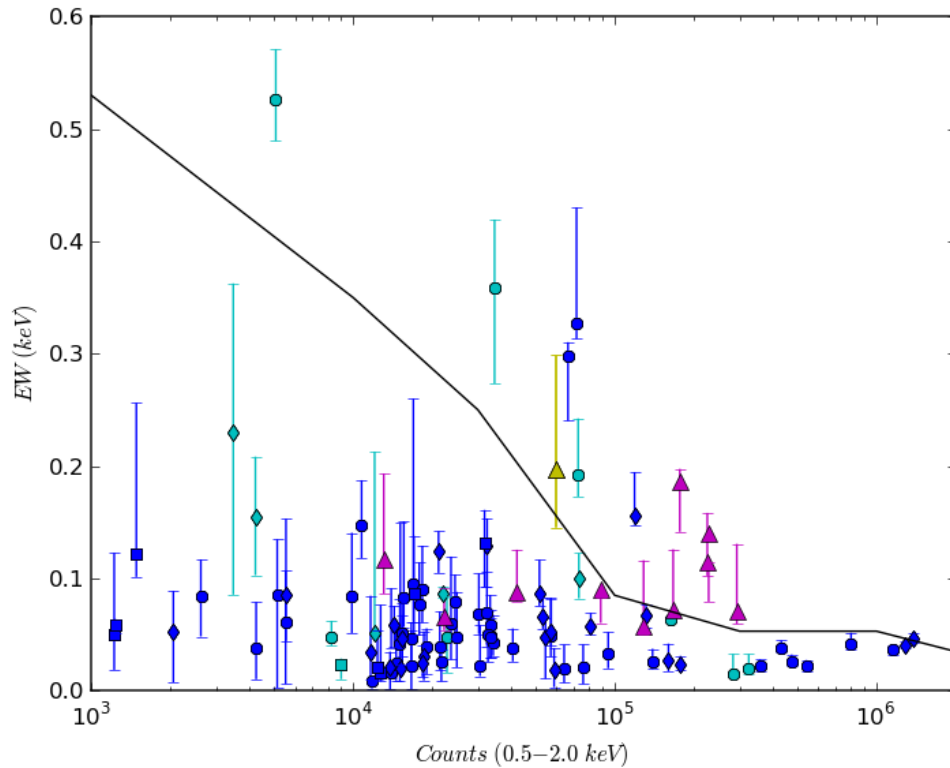

Figure 4.6: *The 3σ boundary plotted over the objects in the B and C samples, shown by the blue and cyan points, respectively. The purple triangles show observations of 1H0707–495, and the yellow triangle shows the observation of IRAS 13224-3809. The diamonds, circles, and squares represent NLS1, BLS1, and 'other' objects, respectively.*

4.2 Blurred Reflection Models

As can be seen from Figure 4.6, there are seven objects, in addition to 1H 0707-495 and IRAS 13224-3809, that lie above the threshold described in the previous section. This means that the Fe-Lα line can likely be distinguished from an absorption edge in these objects. Consequently, these objects are strong candidates for reverberation mapping studies. While the phenomenological model is useful for finding strong Fe-Lα emitters, it does not model all spectral features and is a crude approximation of the continuum emission. Therefore, it would be useful to fit blurred reflection models to these objects. Listed in order of increasing number of $0.5 - 2.0$ keV counts, these objects are NGC 4235, 1H0419–577, QSO 0056–363, NGC 985, IRAS 13349+2438, NGC 4051, and Akn 564.

These objects were first fit with a "baseline" reflection model consisting of Galactic photoelectric absorption (the TBABS component in XSPEC) and two broad band components, namely a blurred reflector (REFLIONX, Ross & Fabian 2005, convolved with the LAOR kernel, KDBLUR2) and a power law. To obtain the best-fit models, other components were then added to this model as necessary on an object-by-object basis.

The KDBLUR2 component convolves the spectrum by the relativistic effects from an accretion disk with a broken power law emissivity profile, which is more realistic than an accretion disk with a single power law emissivity profile across the entire disk. A broken power law allows the emissivity power law index to change at a specific accretion disk radius. The parameters of the KDBLUR2 component are: the inner disk emissivity index (q_{in}), the inner radius of the accretion disk (r_{in}), the outer radius of the accretion disk (r_{out}), the inclination of the accretion disk (i), the break-radius (r_{break}) which describes the disk radius at which the emissivity index changes, and the outer emissivity index (q_{out}), which is the emissivity index that is valid for radii greater than r_{break}. The REFLIONX component models the emergent reflection spectrum for an accretion disk of constant density illuminated by a power law source. The parameters of the REFLIONX component are: the abundance of iron relative to the solar value (A_{Fe}), the photon index of the illuminating

power law spectrum (Γ), the ionization parameter (ξ) as defined in Section 1.3.3, the redshift (z), and the normalization of the reflection spectrum.

For each best-fit model, the photoelectric absorption (TBABS) is fixed at the Galactic value as measured by Kalberla *et al.* (2005). The redshift in REFLIONX is fixed to that of the host galaxy. The photon index of the reflection component is set to the photon index of the power law component, and the outer radius is fixed to the maximum value of $400r_g$, as we did for the LAOR profile fits in Section 3. Unless otherwise stated all other parameters were allowed to vary. In objects where a changing emissivity index across the accretion disk was not required, r_{break} was fixed to r_{out}, and q_{out} was fixed to q_{in}.

Some objects required additional components (see Chapter 1) to achieve good fits. For example, some objects required distant reflectors (Section 1.2.3). In these cases, the distant reflectors were modelled with an un-convolved (i.e. unblurred) REFLIONX component, with parameters fixed to and $A_{Fe} = 1.0; \Gamma = 1.9; \xi = 1.0$ erg cm s^{-1}. Narrow emission from FeXXV at 6.70 keV and FeXXVI at 6.97 keV is seen in $\sim 30\%$ of AGN and when required, these are modelled with narrow Gaussian profiles.

For several objects, the $0.5 - 2.0$ keV band has been studied in detail with high energy resolution gratings. Many of these studies have found evidence for ionized emission and/or absorption. When emission features have been required, they have been modelled by Gaussian profiles with energies, widths, and fluxes fixed to the published values. When warm absorption has been required, it has been incorporated with the XSTAR analytical model, which calculates the emergent spectrum as modified by a warm absorber. The model parameters of the XSTAR component are the column density of the absorbing gas (n_H), the ionization state of the gas [$log(\xi)$], the iron abundance relative to the solar value (A_{Fe}), the oxygen abundance relative to the solar value (A_O) and the redshift of the object (z). Again, these model parameters have been set to fall within the expected range of values as determined from previous high resolution studies.

The best-fit reflection model, for each of the seven objects, is described in detail below. The best-fit models with the data for the seven objects are shown in Figure 4.7. A summary of the

best-fit model parameters for these objects is given in Table 4.2. The calculated blurred reflection fractions in the 0.3 –10 keV band, defined as the flux ratio between the reflection and power law components (F_r / F_p) for each object are also shown in Table 4.2. The reflection fraction is used to determine whether or not the object is in a reflection dominated state (see Chapter 1) at the time of the observation. The best-fit parameters are given in the rest frame of the object, while the figures are shown in the observed frame. The reported errors correspond to a 90% confidence interval (i.e 1.64σ), unless otherwise stated. A standard cosmology ($\Omega_M = 0.3$, and $\Omega_\Lambda = 0.7$) and Hubble Constant of $H_0 = 70$ km s^{-1} Mpc^{-1} was assumed.

NGC 4235: NGC 4235 is a BLS1 galaxy at redshift $z = 0.008$. In addition to the baseline model, the best-fit model consists of distant reflection and cold absorption consistent with Papadakis *et al.* (2008). The cold absorber is modelled by ZWABS in XSPEC which requires the column density (n_H) and redshift as model parameters. The best-fit column density of the cold absorber has a value of $n_H = (1.56^{+0.03}_{-0.01}) \times 10^{21}$ cm^{-2}. The best-fit line energy of the distant reflector is $E = 6.41^{+0.03}_{-0.05}$ keV. The emissivity index was consistent across the disk and rather flat, consistent with isotropic illumination. The best-fit model and the data to model ratio is shown in Figure 4.8.

1H0419–577: 1H0419–577 is a BLS1 galaxy, with a redshift of $z = 0.104$, that shows significant X-ray variability in the soft X-ray regime (Fabian *et al.* 2005). The steep radial dependence of the emissivity profile implies that the inner disk is more illuminated than the outer region, indicating that the ionization structure of the disk surface is likely dependant on r. Therefore, the simple reflection model is replaced with a more physical one, where the inner disk is allowed to have a different ionization state than the outer disk. To achieve this, a second blurred reflector is added to the baseline model, where the ionization parameter of one reflector is high, and the ionization parameter of the other is low. Allowing the inner region of the disk to have a different ionization structure results in a significantly better fit.

Five Gaussian emission lines, which were detected in the RGS spectrum (Pounds *et al.* 2004b), are also required for an acceptable fit. The emission line energies (and corresponding features) are E = 0.74 keV (OVII recombination), E = 0.42 keV ([NVI]), E = 0.56 keV ([OVII]), E = 0.57 keV

Table 4.2: Summary of Blurred Reflection Models

Best-Fit Par.	NGC 4235	1H0419–577	QSO 0056–363	NGC 985	IRAS 13349+2438	NGC 4051	Akn 564
q_{in}	$3.15^{+1.89}_{-1.53}$	7.00 (f)	$6.55^{+2.69}_{-2.76}$	$3.71^{+1.79}_{-1.66}$	$8.40^{+0.52}_{-0.61}$	$5.45^{+2.00}_{-2.13}$	$9.98^{+2.77}_{-2.02}$
q_{out}	3.15 (f)	$3.91^{+0.49}_{-0.67}$	6.55 (f)	3.71 (f)	$3.80^{+0.26}_{-0.31}$	$3.09^{+0.15}_{-0.11}$	$1.93^{+0.21}_{-0.18}$
r_{in} (r_g)	$3.64^{+2.31}_{-1.68}$	$3.91^{+1.57}_{-1.64}$	$2.17^{+0.27}_{-0.29}$	$2.11^{+0.06}_{-0.10}$	$1.31^{+0.06}_{-0.05}$	$1.48^{+0.29}_{-0.22}$	$1.24^{+0.18}_{-0.19}$
r_{break} (r_g)	400 (f)	$4.93^{+0.92}_{-1.17}$	400 (f)	400 (f)	$2.86^{+0.23}_{-0.41}$	$6.37^{+1.45}_{-1.61}$	$2.87^{+0.52}_{-0.41}$
inc. (deg.)	$48.24^{+9.32}_{-10.04}$	$25.88^{+4.82}_{-5.04}$	$27.20^{+14.98}_{-14.64}$	$45.57^{+4.66}_{-4.72}$	$36.14^{+1.58}_{-2.04}$	$17.07^{+6.03}_{-6.20}$	$63.15^{+2.87}_{-2.43}$
Γ	$1.71^{+0.12}_{-0.09}$	$2.10^{+0.05}_{-0.09}$	$2.25^{+0.03}_{-0.07}$	$1.82^{+0.01}_{-0.04}$	$2.10^{+0.09}_{-0.07}$	$2.04^{+0.01}_{-0.01}$	$2.65^{+0.01}_{-0.01}$
ξ_1 (erg cm s^{-1})	$1.90^{+0.74}_{-0.35}$	$7.53^{+3.95}_{-3.27}$	$49.84^{+22.58}_{-23.19}$	$7.28^{+4.26}_{-4.15}$	$887.23^{+169.02}_{-184.65}$	$436.40^{+90.62}_{-98.36}$	$665.79^{+53.80}_{-57.25}$
ξ_2 (erg cm s^{-1})		$49.86^{+8.42}_{-8.28}$			$9.78^{+5.30}_{-4.92}$		
A_{Fe}	$1.34^{+0.99}_{-1.07}$	$0.69^{+0.29}_{-0.17}$	1.00 (f)	$0.72^{+0.44}_{-0.39}$	$3.60^{+0.95}_{-0.68}$	$0.77^{+0.07}_{-0.11}$	$1.19^{+0.21}_{-0.26}$
R. F.	$0.29^{+0.21}_{-0.19}$	$1.08^{+0.51}_{-0.44}$	$0.41^{+0.29}_{-0.22}$	$0.69^{+0.38}_{-0.43}$	$3.74^{+1.87}_{-1.64}$	$0.82^{+0.36}_{-0.31}$	$1.12^{+0.53}_{-0.44}$
χ^2_ν / dof	$1.003 / 313$	$0.941 / 648$	$0.977 / 780$	$1.029 / 1276$	$0.997 / 1073$	$1.067 / 1744$	$1.041 / 1529$

The best-fit values for the strong Fe-Lα emitters. The calculated reflection fraction, R.F., is also listed for each object. Values denoted with (f) are fixed.

(OVII), and E = 0.65 keV (OVIII Lyα). Figure 4.9 shows the best-fit model with the data to model ratio.

QSO 0056–363: QSO 0056–363 is a broad line quasar with a redshift of $z = 0.164$. A distant reflector plus the baseline model make up the best-fit model, which is shown below in Figure 4.10. A changing emissivity index was not required for an acceptable fit.

NGC 985: NGC 985 is a BLS1 galaxy located at redshift $z = 0.043$. The best-fit model consists of the baseline model, a warm absorber (as described by Krongold *et al.* 2008), and a distant reflector. The warm absorber has best-fit parameter values of $n_H = (1.89^{+1.13}_{-1.07}) \times 10^{22}$ cm^{-2} and $log(\xi) = 1.88^{+0.07}_{-0.06}$. The best-fit line energy of the distant reflector is $E = 6.43^{+0.02}_{-0.01}$ keV. A constant emissivity index provided an acceptable fit. The best-fit model and the data to model ratio are shown in Figure 4.11.

IRAS 13349+2438: IRAS 13349+2438 is a broad line quasar at $z = 0.1076$. The best-fit model (Figure 4.12) is composed of two warm absorbers (as described by Lee *et al.* 2013), a second blurred reflector, and two Fe emission lines in addition to the baseline model. The multi-zone warm absorber has parameter values of WA$_1$: $n_H = 1.01 \times 10^{21}$ cm^{-2}, $log(\xi) = 1.67$, and WA$_2$: $n_H = (1.00^{+0.04}_{-0.08}) \times 10^{22}$ cm^{-2}, $log(\xi) = 1.62^{+0.10}_{-0.08}$. All values for WA$_1$ are fixed, while for the second WA the parameters were allowed to vary. The best-fit values from both warm absorbers are consistent with those published by Lee *et al.* (2013). The Fe emission line energies are fixed at $E = 6.70$ keV (FeXXV) and $E = 6.97$ keV (FeXXVI).

NGC 4051: NGC 4051 is a NLS1 galaxy located at redshift $z = 0.0023$. In addition to the baseline model, the best-fit model consists of seven narrow Gaussian emission lines (as described by Uttley *et al.* 2004), a distant reflection component and five warm absorbers (as described by King *et al.* 2012). The emission line energies (and corresponding features) are E = 0.74 keV (OVII recombination), E = 0.56 keV ([OVII]), E = 0.65 keV (OVIII Lyα), E = 0.91 keV (NeIX and OVIII), E = 0.725 (FeXVII), E = 6.40 keV (Fe XVII, Fe-Kα), and E = 6.71 keV (FeXXV Kα). The warm absorbers have parameter values of WA$_1$: $n_H = 1.40 \times 10^{22}$ cm^{-2}, $log(\xi) = 2.97$, WA$_2$: $n_H = 1.00 \times 10^{20}$ cm^{-2}, $log(\xi) = -0.47^{+0.19}_{-0.21}$, WA$_3$: $n_H = (1.11^{+0.08}_{-0.12}) \times 10^{22}$ cm^{-2}, $log(\xi) = 4.36^{+1.47}_{-1.55}$,
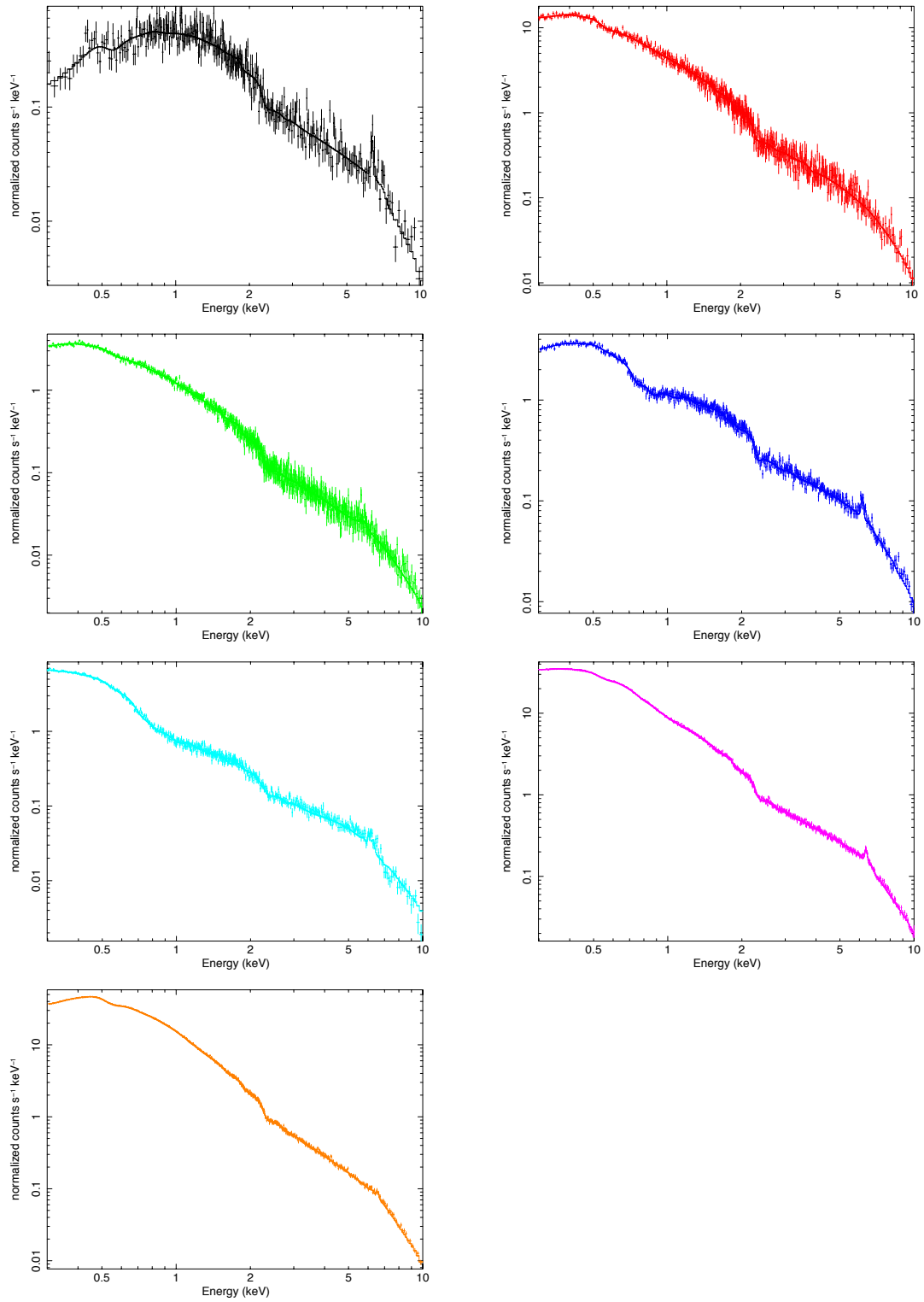
Figure 4.7: *The best-fit model with the data for NGC 4235, 1H0419–577, QSO 0056–363, NGC 985, IRAS 13349+2438, NGC 4051, and Akn 564, from left to right.*
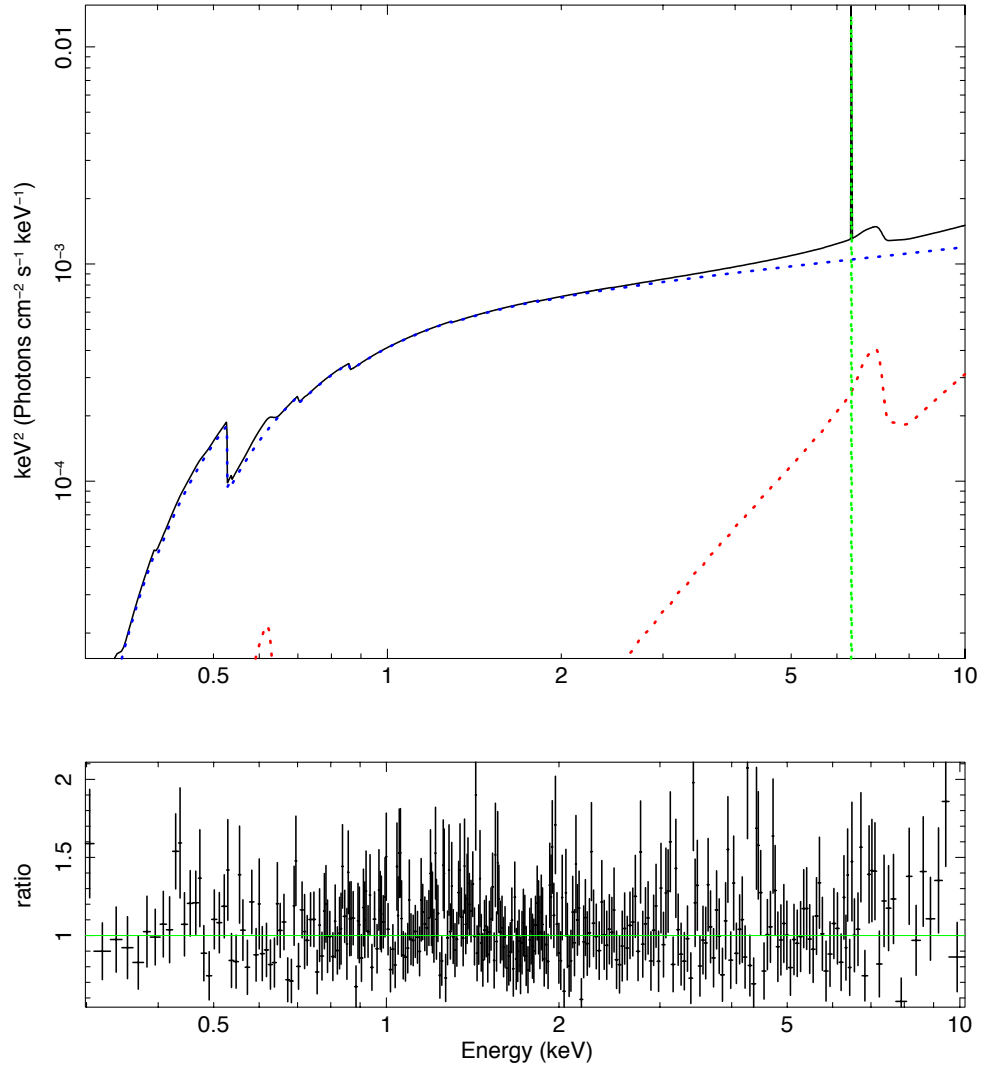
Figure 4.8: *Top panel: The best-fit model for NGC 4235. The* REFLIONX *component is shown in red, the distant reflection component is shown in green, and the power law is shown in blue. The total model is shown in black. Bottom Panel: The data to model ratio.*
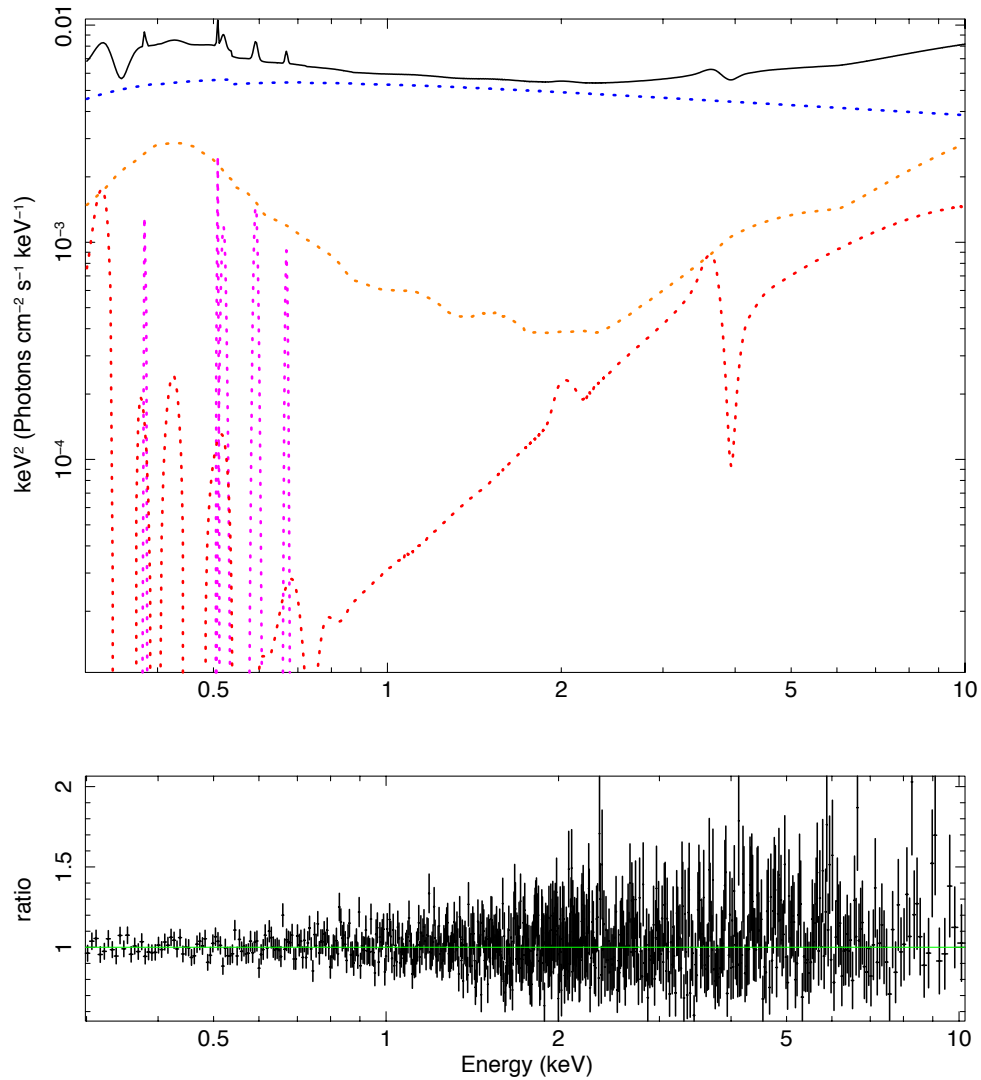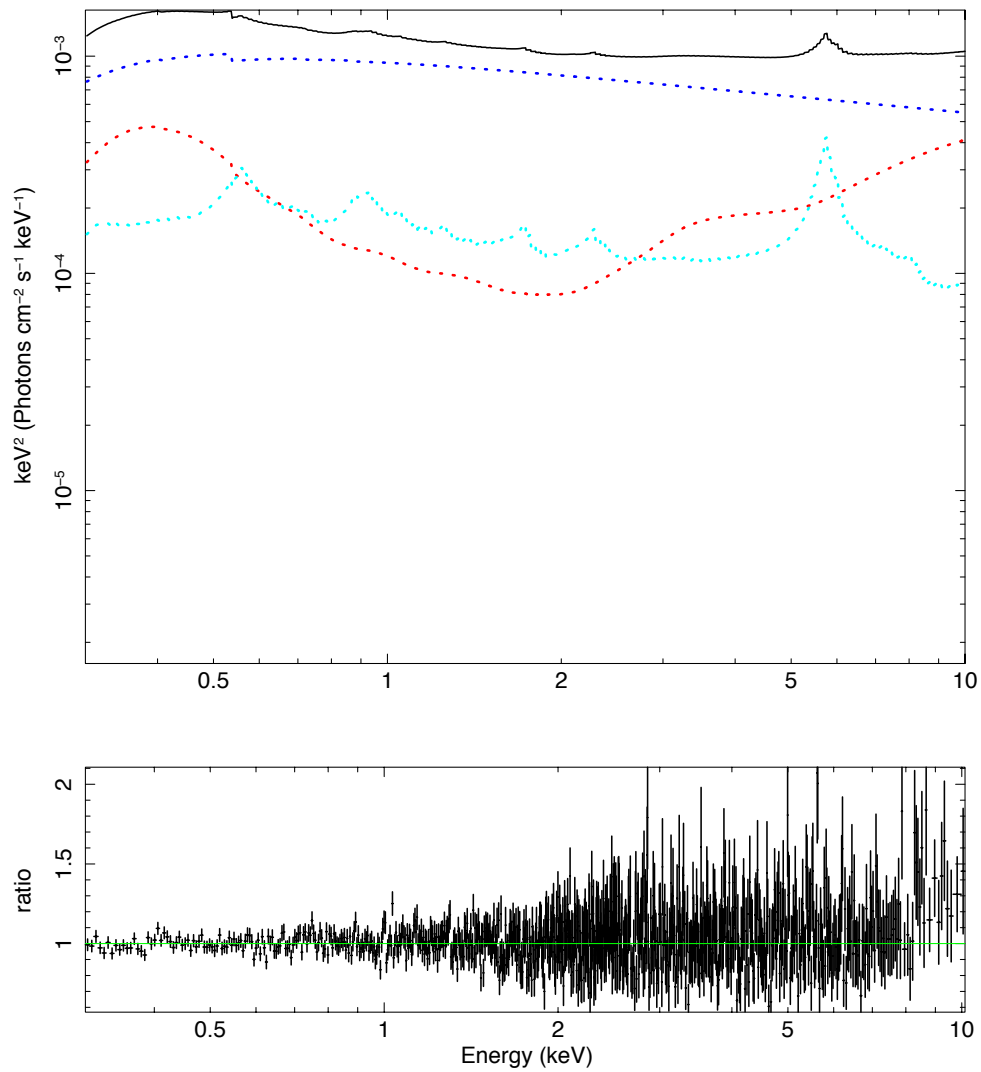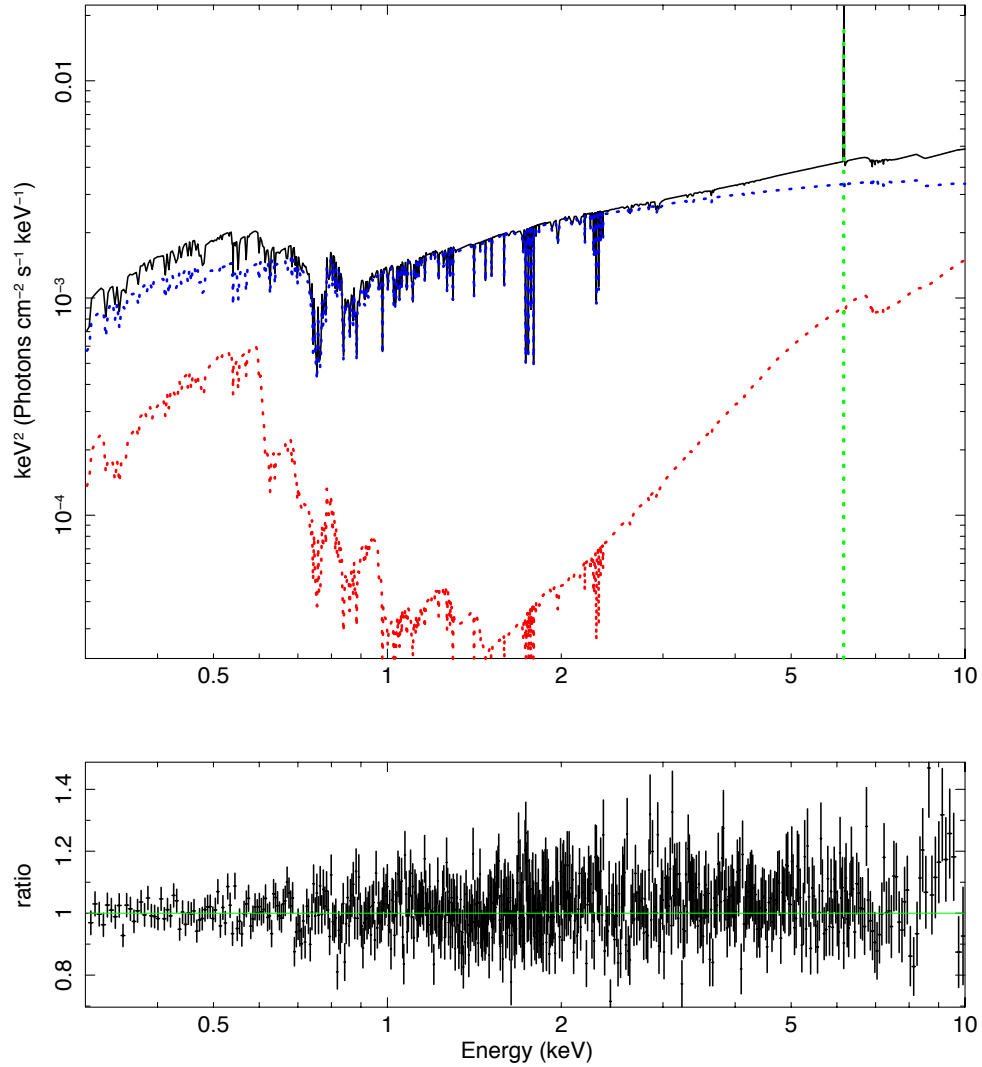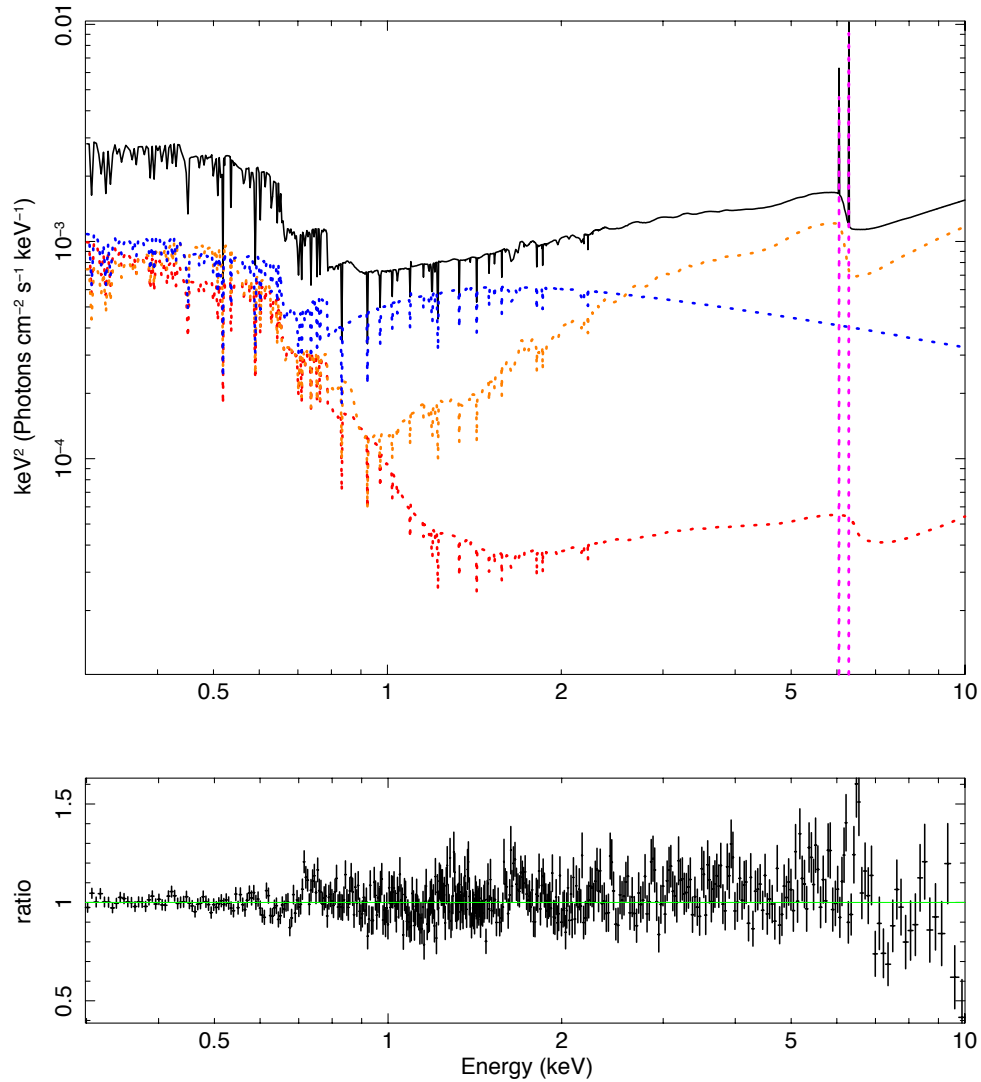
Figure 4.9: *Top panel: The best-fit model for 1H0419–577. The* REFLIONX *component with high ionization is shown in red, the* REFLIONX *component with low ionization is shown in orange, the Gaussian emission lines are shown in magenta, and the power law is shown in blue. The total model is shown in black. Bottom Panel: The data to model ratio.*

Figure 4.10: *Top panel: The best-fit model for QSO 0056–363. The* REFLIONX *component is shown in red, the distant reflection component is shown in light blue, and the power law is shown in blue. The total model is shown in black. Bottom Panel: The data to model ratio.*

Figure 4.11: *Top panel: The best-fit model for NGC 985. The* REFLIONX *component is shown in red, the distant reflection component is shown in green, and the power law is shown in blue. The total model is shown in black. Bottom Panel: The data to model ratio.*

Figure 4.12: *Top panel: The best-fit model for IRAS 13349+2438. The* REFLIONX *component with high ionization is shown in red, the* REFLIONX *component with low ionization is shown in orange, the Gaussian emission lines are shown in magenta, and the power law is shown in blue. The total model is shown in black. Bottom Panel: The data to model ratio.*

WA$_4$: $n_H = (5.41^{+2.07}_{-2.21}) \times 10^{21}$ cm^{-2}, $log(\xi) = 2.50^{+1.14}_{-1.35}$, and WA$_5$: $n_H = (4.58^{+2.28}_{-2.31}) \times 10^{20}$ cm^{-2}, $log(\xi) = 1.78^{+0.89}_{-0.73}$. All values for WA$_1$ are fixed, while only $log(\xi)$ is allowed to vary in WA$_2$. The parameters for the other warm absorbers were allowed to vary. The best-fit values from all warm absorbers are consistent with those published by King *et al.* (2012). Figure 4.13 shows the best-fit model with the data to model ratio. The small residuals in the low energy region can be improved with an absorption edge, however, the best-fit continuum values are not largely affected by the addition of the absorption edge.

Akn 564: Akn 564 is a NLS1 located at $z = 0.0247$. The best-fit model requires three warm absorbers (as described by Dewangan *et al.* 2007) and two Gaussian emission lines (as described by Smith *et al.* 2008). The best-fit model and the data to model ratio is shown in Figure 4.14. Values for the warm absorbers are WA$_1$: $n_H = 2.41 \times 10^{20}$ cm^{-2}, $log(\xi) = 0.87$, WA$_2$: $n_H = 6.03 \times 10^{20}$ cm^{-2}, $log(\xi) = 2.56$, and WA$_3$: $n_H = 1.00 \times 10^{20}$ cm^{-2}, $log(\xi) = -0.75^{+0.04}_{-0.06}$. The values of n_H and $log(\xi)$ are fixed for WA$_1$ and WA$_2$, while only $log(\xi)$ varies for WA$_3$. The emission line features and energies are E = 0.56 keV ([OVII]), and E = 6.71 keV (FeXXV).

The values of the blurred reflection continuum are presented in Table 4.2. The values of Γ, ξ, and $A(Fe)$ are all within the average values for Type-1 AGN (Walton *et al.* 2013). Therefore, there is no distinguishing spectral characteristic that makes the detection of Fe-Lα more probable in these objects compared to any other object. The calculated reflection fractions are also typical and these objects are not necessarily reflection dominated. This indicates that if the feature is present, only strong S/N is needed to detect Fe-Lα and distinguish it from an absorption edge.

4.3 Multi-Epoch Fitting

Five of the seven candidates for strong Fe-Lα emission have multiple observations. These objects are 1H0419–577, QSO 0056–363, IRAS 13349+2438, NGC 4051, and Akn 564. For completeness, the best-fit model for the observation above the 3σ threshold was also applied to the other observations,
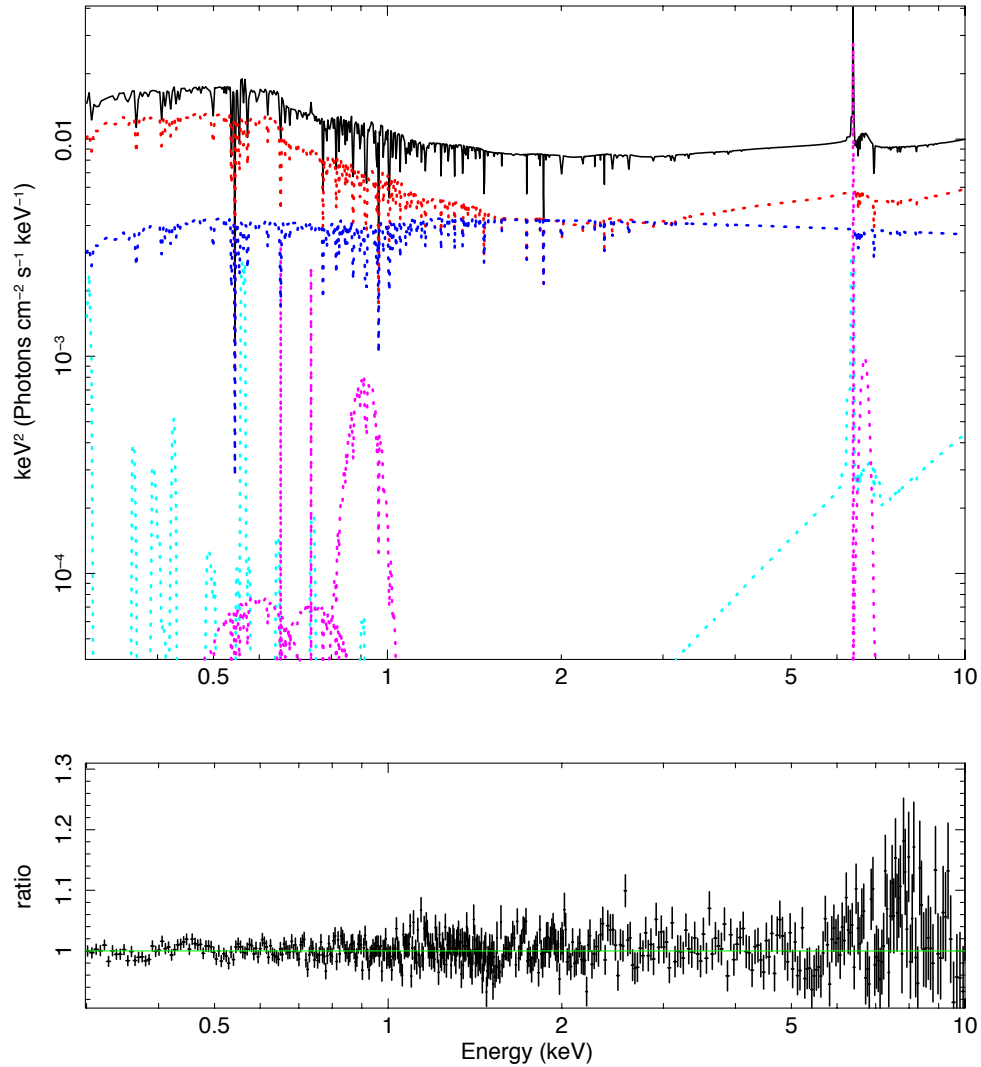
Figure 4.13: *Top panel: The best-fit model for NGC 4051. The* REFLIONX *component is shown in red, the distant reflection component is shown in light blue, the Gaussian emission lines are shown in magenta, and the power law is shown in blue. The total model is shown in black. Bottom Panel: The data to model ratio.*
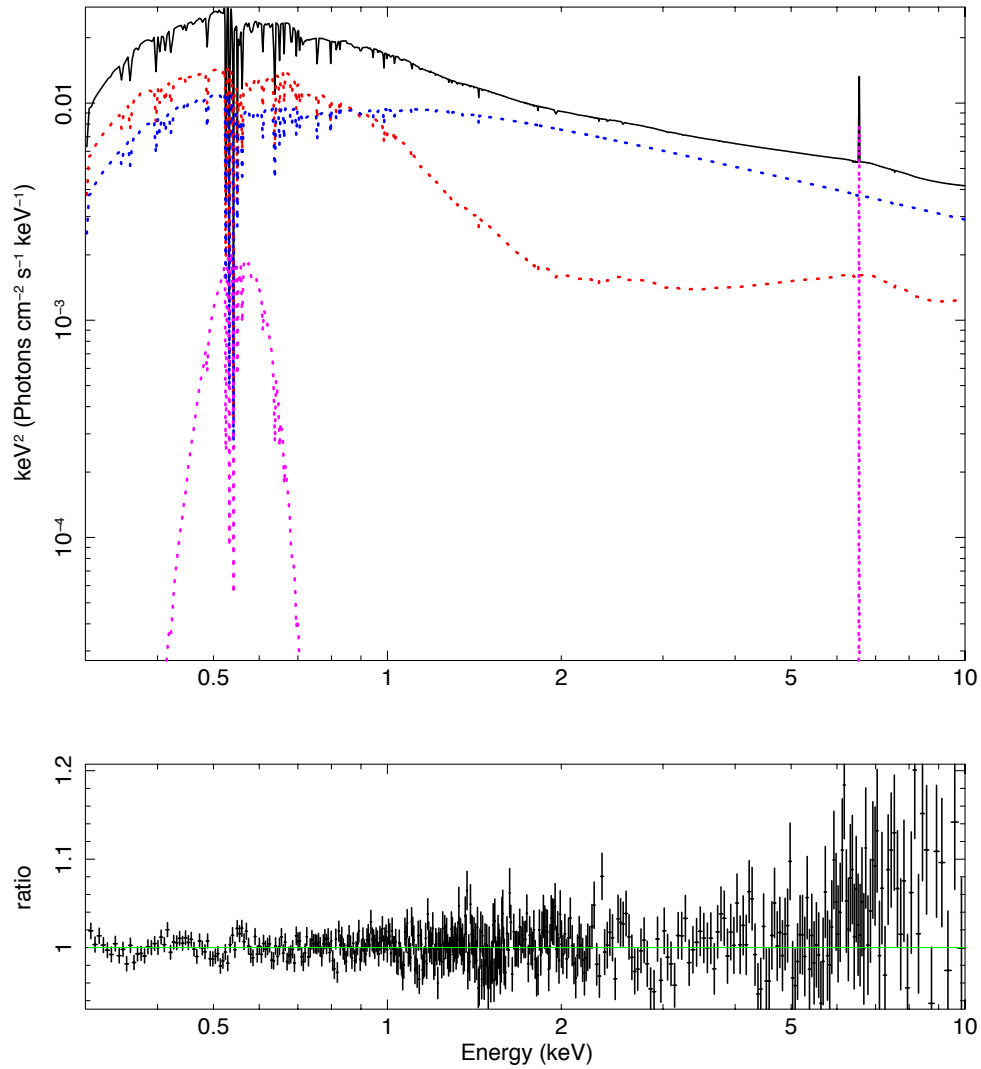
Figure 4.14: *Top panel: The best-fit model for Akn 564. The* REFLIONX *component is shown in red, the Gaussian emission lines are shown in magenta, and the power law is shown in blue. The total model is shown in black. Bottom Panel: The data to model ratio.*

for each object with multiple observations. The normalizations of the REFLIONX components were set equal across all observations of an object. The photon indices were also equal across all observations of an object. The results for each object are described in detail below.

1H0419–577: There are six observations of 1H0419–577 in addition to that in which 1H0419–577 lies above the 3σ threshold. The $0.3 - 10$ keV flux varies by a factor of ~ 10 over all epochs. The multi-epoch spectral changes are mainly attributed to flux changes in the power law component with expected changes in the ionization parameter of the disk. The changes across the epochs are reasonable given the differing flux states of the observations. There is no trend between the best-fit parameter values and the flux state of the observation. The best-fit model with the data and the residuals are shown in Figure 4.15, and the best-fit model and components are shown in Figure 4.16. Fitting the best-fit model to all observations yields $\chi^2_\nu = 1.067$ for 3958 degrees of freedom.

QSO 0056–363: In total, there are three observations of QSO 0056–363. The best-fit parameter values are similar across all observations. There is no trend between the best-fit parameters across the three epochs. Figures 4.17 and 4.18 show the best-fit model with the data and the residuals, and the best-fit model and components, respectively. Fitting the best-fit model to all observations yields $\chi^2_\nu = 1.039$ for 2435 degrees of freedom. Most of the differences between epochs can be attributed to changes in the inner emissivity index.

IRAS 13349+2438: There are four observations of IRAS 13349+2438 in total. Most of the differences between epochs can be attributed to the disk ionization parameter, which is lowest for the observation above the 3σ threshold. The best-fit model with the data and the residuals are shown in Figure 4.19, and the best-fit model and components are shown in Figure 4.20. Fitting the best-fit model to all observations yields $\chi^2_\nu = 1.025$ for 3150 degrees of freedom.

NGC 4051: In total, there are two observations of NGC 4051. The multi-epoch spectral variations are mainly attributed to the varying disk ionization parameter. There is no trend between the best-fit parameters across the two epochs. The best-fit model with the data and the residuals are shown in Figure 4.21, and the best-fit model and components are shown in Figure 4.22. Fitting the best-fit model to all observations yields $\chi^2_\nu = 1.143$ for 2876 degrees of freedom.
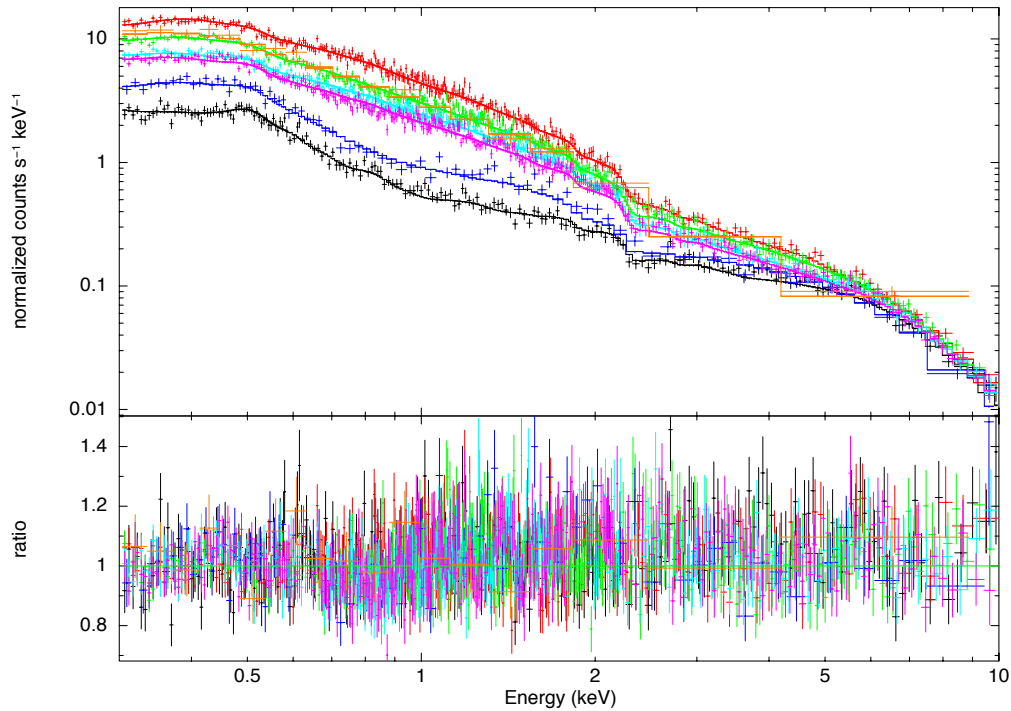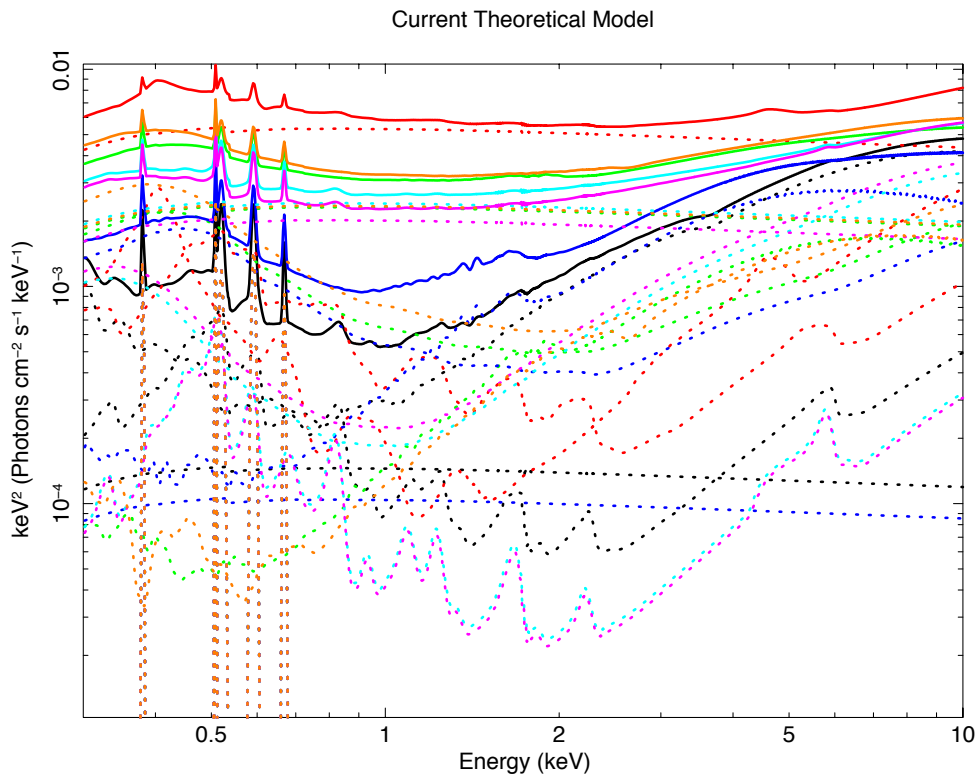
Figure 4.15: *Top Panel: The best-fit model with the data for the seven observations of 1H0419–577. The observation shown in black is the one in which 1H0419–577 lies above the 3σ threshold. Bottom Panel: The data to model ratios for all observations.*

Akn 564: In total, there are three observations of Akn 564. The multi-epoch spectral changes are mainly attributed to changes in the ionization parameter of the disk. There is no trend between the best-fit parameters across the three epochs. Figures 4.23 and 4.24 show the best-fit model with the data and the residuals, and the best-fit model and components, respectively. Fitting the best-fit model to all observations yields $\chi^2_\nu = 1.063$ for 3184 degrees of freedom.

Figure 4.16: *The best-fit model and components for 1H0419–577. The model shown in black is the one applied to the 1H0419–577 observation above the 3σ threshold. The solid lines show the total model, while the dashed and dotted lines show the components that make up the model.*
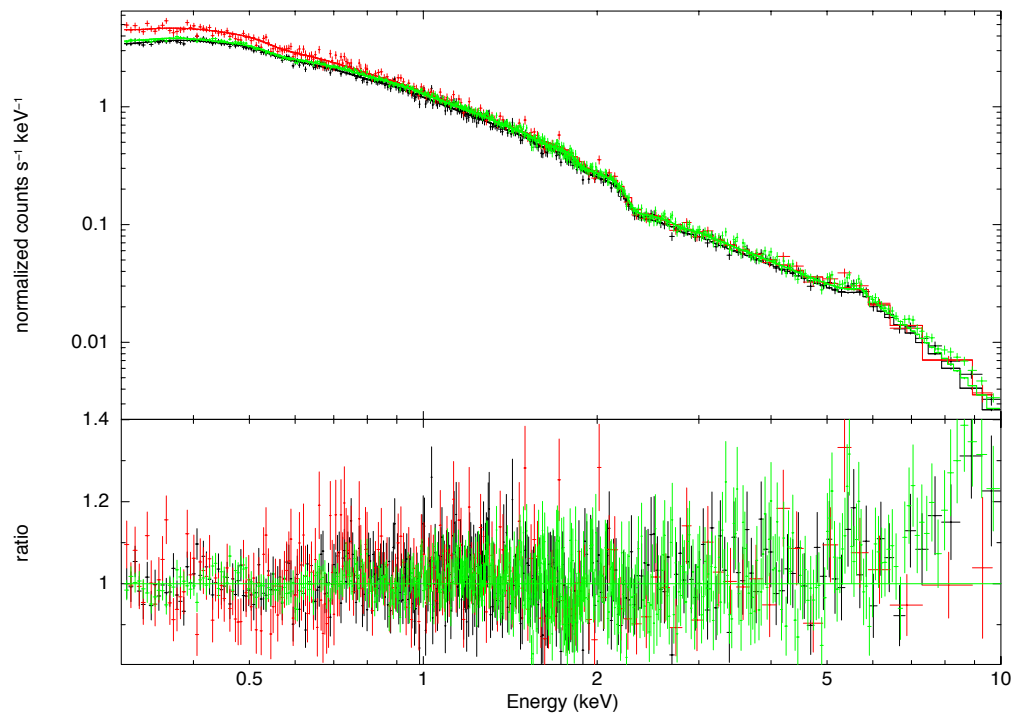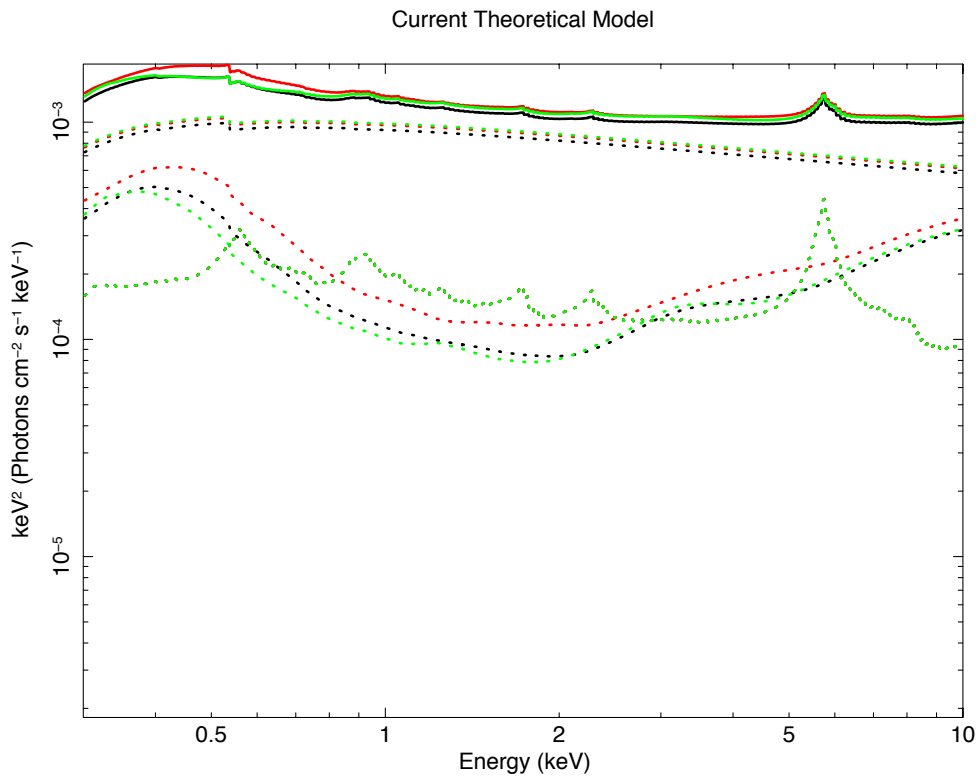
Figure 4.17: *Top Panel: The best-fit model with the data for the three observations of QSO 0056–363. The observation shown in black is the one in which QSO 0056–363 lies above the 3σ threshold. Bottom Panel: The data to model ratios for all observations.*

Figure 4.18: *The best-fit model and components for QSO 0056–363. The model shown in black is the one applied to the QSO 0056–363 observation above the 3σ threshold. The solid lines show the total model, while the dashed and dotted lines show the components that make up the model.*
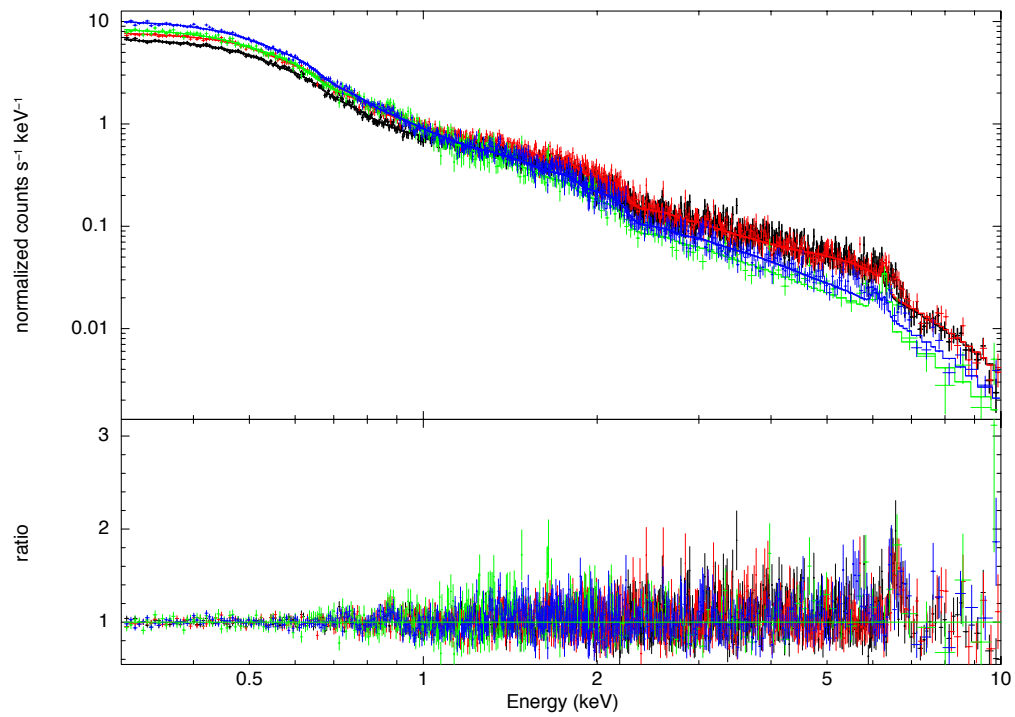
Figure 4.19: *Top Panel: The best-fit model with the data for the four observations of IRAS 13349+2438. The observation shown in black is the one in which IRAS 13349+2438 lies above the 3σ threshold. Bottom Panel: The data to model ratios for all observations.*
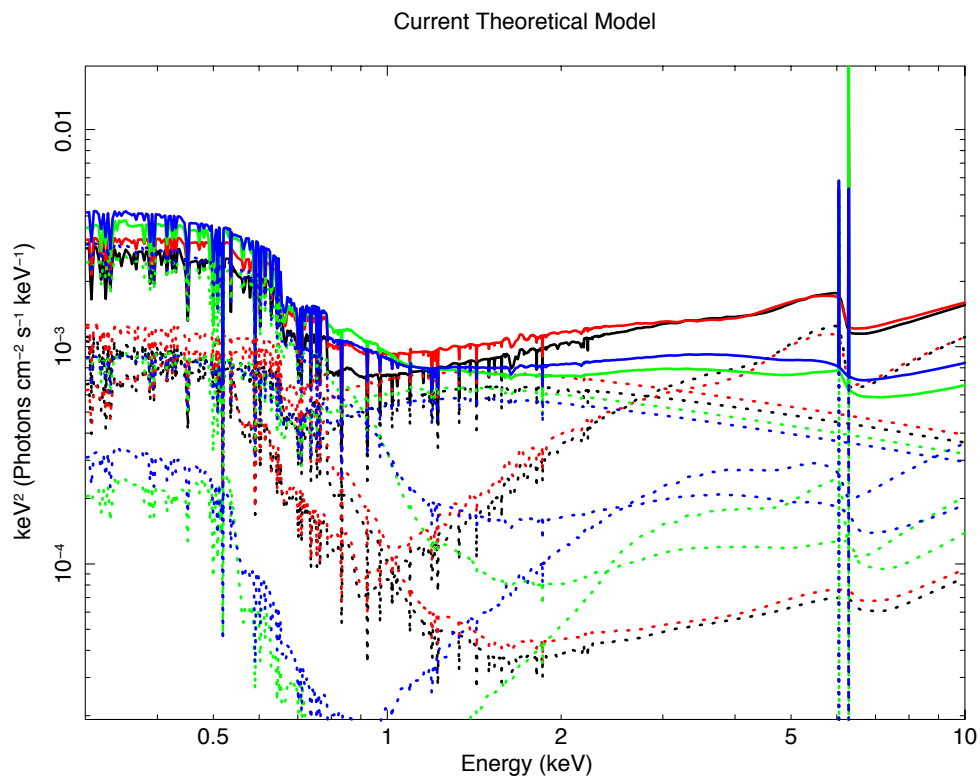
Current Theoretical Model

Figure 4.20: *The best-fit model and components for IRAS 13349+2438. The model shown in black is the one applied to the IRAS 13349+2438 observation above the 3σ threshold. The solid lines show the total model, while the dashed and dotted lines show the components that make up the model.*
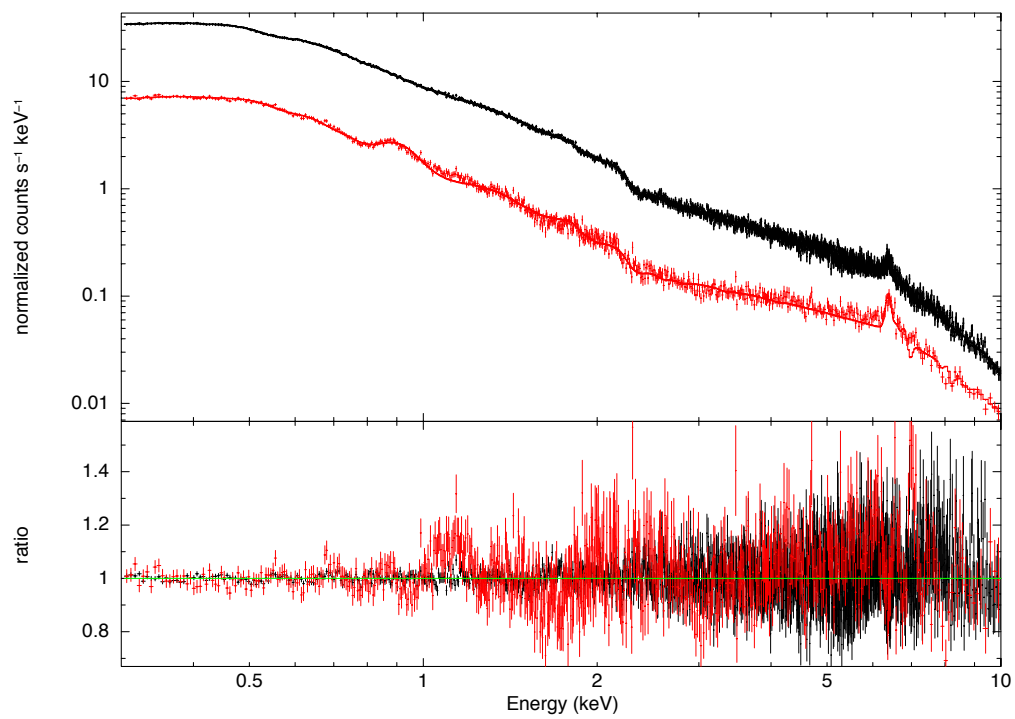
Figure 4.21: *Top Panel: The best-fit model with the data for both observations of NGC 4051. The observation shown in black is the one in which NGC 4051 lies above the 3σ threshold. Bottom Panel: The data to model ratios for both observations.*
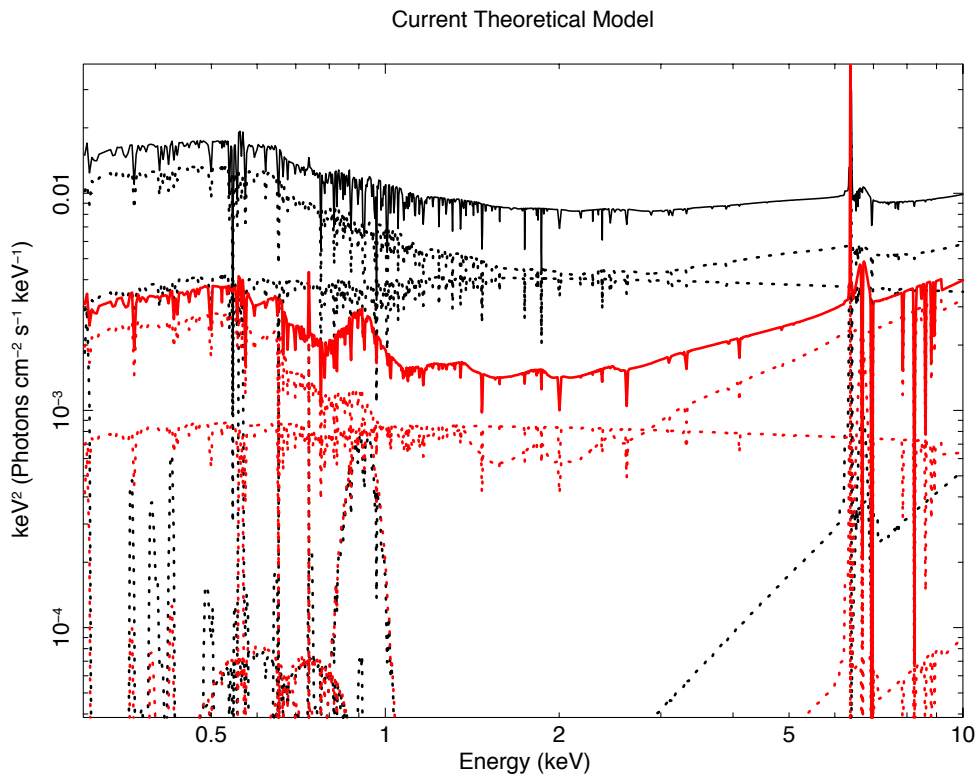
Figure 4.22: *The best-fit model and components for NGC 4051. The model shown in black is the one applied to the NGC 4051 observation above the 3σ threshold. The solid lines show the total model, while the dashed and dotted lines show the components that make up the model.*
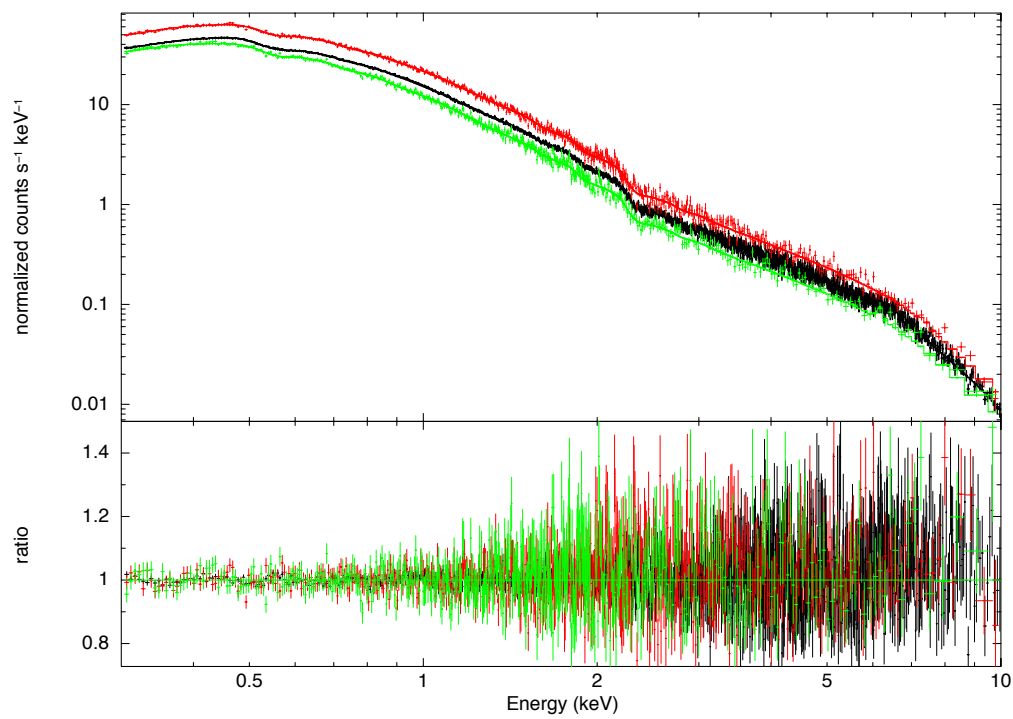
Figure 4.23: *Top Panel: The best-fit model with the data for the three observations of Akn 564. The observation shown in black is the one in which Akn 564 lies above the 3σ threshold. Bottom Panel: The data to model ratios for both observations.*
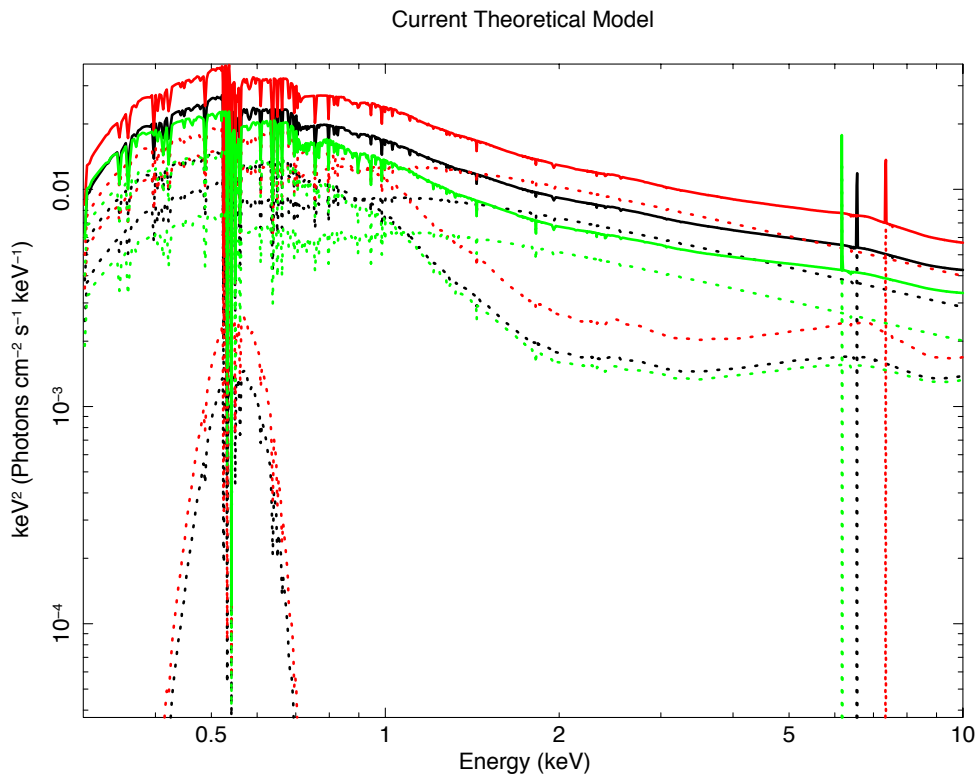
Figure 4.24: *The best-fit model and components for Akn 564. The model shown in black is the one applied to the Akn 564 observation above the 3σ threshold. The solid lines show the total model, while the dashed and dotted lines show the components that make up the model.*

Chapter 5

Conclusions

Reflection spectra of Seyfert-1 AGN are generated from partial reprocessing of the primary X-ray emitter by the cold accretion disk surrounding the SMBH. The strength and shape of the spectral features of the reflection spectrum, which are due to photoelectric absorption, fluorescence and Compton scattering processes, tell us information about the composition, motion, gravitational potential depth, abundance, and ionization of the accretion disk, as well as the geometry of the SMBH region. The most prominent X-ray reflection feature is the Fe-Kα line at 6.4 keV that originates from just a few gravitational radii from the central black hole and is broadened by relativistic effects. This broad line is therefore a powerful diagnostic tool for measuring properties of the black hole, such as mass, inclination, spin, the location and kinematics of the accretion disk, via the techniques of line spectroscopy. The challenge is that Fe-Kα arises in a spectral region where current telescopes are not very efficient photon detectors. Consequently, the features are generally of low S/N and results are questioned. A feature that is expected to coincide with Fe-Kα is Fe-Lα at about 1 keV. This feature is very important because it arises where the efficiency of current telescopes is maximum. The detection of such a high S/N feature provides confirmation of the reflection model based on Fe-Kα alone and also presents the possibility to attempt reverberation mapping in AGN. However, to date Fe-Lα emission has only been detected in two objects, namely 1H0707-495 and IRAS 13224–3809. This is presumably due to high iron abundance that allows

Fe-Lα to stand out above other spectral features and high S/N.

Finding other Fe-Lα emitters is therefore important. To find other candidates for strong Fe-Lα emission, a search was completed on a sample of 353 nearby broad and narrow line Type-1 AGN. To establish the presence of Fe-Lα in these objects, the same simple phenomenological model used for the detection of Fe-Lα in 1H0707-495 (Fabian *et al.* 2009) was applied. Potential Fe-Lα emission was detected in 40 BLS1, 22 NLS1, and 3 'other' galaxies. On average, the properties of the emission line was comparable between the object types.

We demonstrate that in low S/N spectra or for weak Fe-Lα emission, an emission line could be well fitted well with an absorption edge. Therefore, even if our entire sample could be fitted well with a LAOR profile, it does not necessarily imply detection of a Fe-Lα line. To determine the strength of the Fe-Lα feature and the S/N of the observation required so that Fe-Lα emission can be differentiated in the spectrum from an absorption edge, simulations were performed for various values of the EW and the number of counts to produce a 4×4 grid. Each simulated spectrum was fit to both an Fe-Lα model and an absorption edge model in the $0.5 - 2.0$ keV range to obtain the EW needed to identify Fe-Lα from an absorption edge, given a certain number of counts, at the 3σ level of significance. A 3σ boundary was then constructed by connecting seven points in EW and number of counts ($0.5 - 2.0$ keV) at the minimum values needed to differentiate between the two features. From this, we found that seven objects in our sample had sufficient S/N to potentially distinguish Fe-Lα from absorption. Detailed fitting of these seven objects found no distinguishing characteristic that would enhance Fe-Lα detectability. It appears that the driving factor in finding Fe-Lα emitters is simply S/N.

Future work on this project would include performing reverberation studies on the seven objects in our high S/N sample. Since beginning this work, a reverberation analysis has been conducted on one of our candidates (Akn 564; Kara *et al.* 2013). They found a strong reverberation lag in Akn 564, which provides support for our work in identifying potential candidates to study. This work only includes AGN in the *XMM-Newton* archive up until 2012. Therefore, it would be useful to apply the phenomenological model to an even larger sample to detect more simultaneous Fe-Lα and

Fe-Kα emission.

Finally, our work can motivate deeper observations of potentially interesting objects. One such object is the NLS1 galaxy 1E 0919+515; which shows strong, well-defined emission line profiles despite having low S/N. To test the *XMM-Newton* exposure time (GTI) needed to detect an Fe-Lα feature with an EW of 60 eV in this object, simulations using the background and response files of 1E 0919+515 were performed. The model used in the simulation consists of Galactic photoelectric absorption, two LAOR lines, a black body component, and a power law. After generating simulated data for a number of exposure times, the spectra were fit with an absorption edge, as in Section 4.1. In this manner, the minimum exposure time needed to distinguish Fe-Lα from the absorption edge was found to be 308 ks. Therefore, if Fe-Lα is present in 1E 0919+515, an *XMM-Newton* observation with a GTI of at least 308 ks would be needed to confirm the existence of the feature at the 3σ level of significance. Figure 5.1 shows the ratio plot of the simulated spectrum.
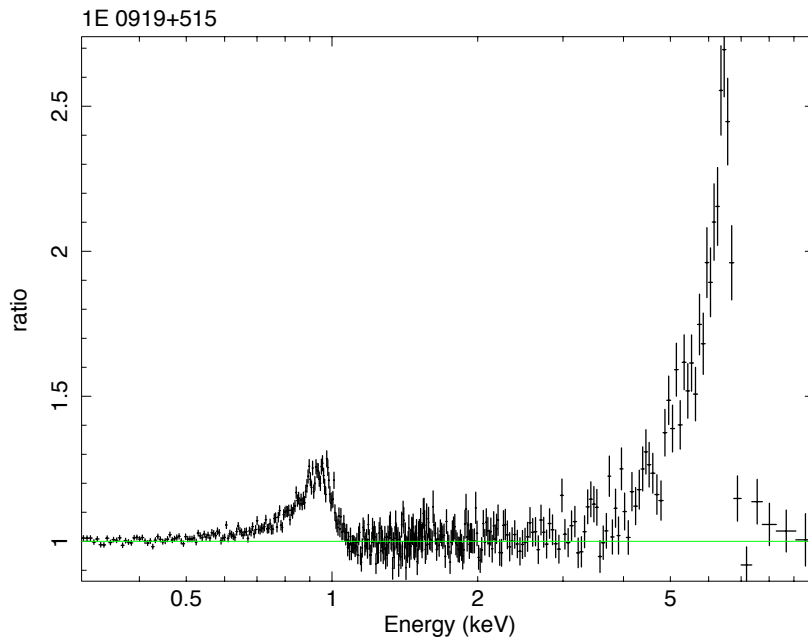

Figure 5.1: *Ratio plot for the simulated observation of 1E 0919+515. If present, Fe-Lα could be distinguished from absorption for an Fe-Lα EW of 60 eV and a GTI exposure of at least 308 ks.*

Bibliography

[1] Arnaud K.A., 1996, Astronomical Society of the Pacific Conference Series 101, 17.

[2] Ballantyne D.R., Ross R.R., Fabian A.C., 2001, Monthly Notices of the Royal Astronomical Society 327, 10.

[3] Bianchi S., Guainazzi M., Fonseca Bonilla N., *et al.*, 2009, Astronomy & Astrophysics 495, 421.

[4] Boller Th., Fabian A.C., Sunyaev R., *et al.*, 2002, Monthly Notices of the Royal Astronomical Society 329, 1.

[5] Boronson T.A., Green R.F., 1992, The Astrophysical Journal Supplement 80, 109.

[6] Brenneman L.W., Reynolds C.S., 2006, The Astrophysical Journal 652, 1028.

[7] Dewangan G.C., Griffiths R.E., Dasgupta S., 2007, The Astrophysical Journal 671, 1284.

[8] Dovčiak M., Karas V., Martocchia A., *et al.*, 2004, The Astrophysical Journal Supplement 153, 205.

[9] Elvis M., Wilkes B.J., McDowell J.C., *et al.*, 1994, The Astrophysical Journal Supplement 95, 1.

[10] Fabian A.C., 1996, International Conference on X-ray Astronomy & Astrophysics: Röntgenstrahlung from the Universe Proceedings, 403.

[11] Fabian A.C., Miniutti G., Iwasawa K., *et al.*, 2005, Monthly Notices of the Royal Astronomical Society 361, 795.

[12] Fabian A.C., Rees M.J., Stella L., *et al.*, 1989, Monthly Notices of the Royal Astronomical Society 238, 729.

[13] Fabian A.C., Zoghbi A., Ross R.R., *et al.*, 2009, Nature 459, 540.

[14] Fabian A.C., Zoghbi A., Wilkins D., *et al.*, 2012, Monthly Notices of the Royal Astronomical Society 419, 116.

[15] Gallo L.C., 2011, Journal of the Royal Astronomical Society of Canada 105, 143.

[16] George I.M., Fabian A.C., 1991, Monthly Notices of the Royal Astronomical Society 249, 352.

[17] Goodrich R.W., 1989, The Astrophysical Journal 342, 224.

[18] Grier C.J., Peterson B.M., Pogge R.W., *et al.*, 2012, The Astrophysical Journal 744, 4.

[19] Grupe D., Wills B.J., Leighly K.M., *et al.*, 2004, The Astrophysical Journal 127, 156.

[20] Jansen F., Lumb D., Altieri B., *et al.*, 2001, Astronomy & Astrophysics 365, 1.

[21] Kallman T.R., 1995, The Astrophysical Journal 455, 603.

[22] Kallman T.R., McCray R.A., 1982, The Astrophysical Journal Supplement 50, 263.

[23] King A.L., Miller J.M., Raymond J., 2012, The Astrophysical Journal 746, 20.

[24] Krolik J.H. (1999). *Active Galactic Nuclei*. Princeton, NJ: Princeton University Press.

[25] Laor A., 1991, The Astrophysical Journal 376, 90.

[26] Lee J.C., Kriss G.A., Chakravorty S., *et al.*, 2013, Monthly Notices of the Royal Astronomical Society 430, 2650.

[27] Mushotzky J.M., 2007, Annual Review of Astronomy & Astrophysics 45, 441.

[28] Mushotzky J.M., Done C., Pounds K.A., 1993, Annual Review of Astronomy & Astrophysics 31, 717.

[29] Osterbrock D.E., Pogge R.W., 1985, The Astrophysical Journal 297, 166.

[30] Papadakis I.E., Ioannou Z., Brinkmann W., *et al.*, 2008, Astronomy & Astrophysics 490, 995.

[31] Péquignot D., Amara M., Liu X.-W., *et al.*, 2002, Revista Mexicana de Astronomía y Astrofísica (Serie de Conferencias) 12, 142.

[32] Peterson B.M. (1997). *An Introduction to Active Galactic Nuclei*. Cambridge, UK: Cambridge University Press.

[33] Ponti G., Gallo L.C., Fabian A.C., *et al.*, 2010, Monthly Notices of the Royal Astronomical Society 406, 2591.

[34] Pounds K.A., Reeves J.N., Page K.L., *et al.*, 2004b, The Astrophysical Journal 616, 696.

[35] Reynolds C.S., Nowak M.A., 2003, Physics Reports 377, 389.

[36] Ross R.R., Fabian A.C., 1993, Monthly Notices of the Royal Astronomical Society 261, 74.

[37] Ross R.R., Fabian A.C., 2005, Monthly Notices of the Royal Astronomical Society 358, 211.

[38] Smith R.A.N., Page M.J., Branduardi-Raymont M., 2008, Astronomy & Astrophysics 490, 103.

[39] Strüder L., Briel U., Dennerel K., *et al.*, 2001, Astronomy & Astrophysics 365, 18.

[40] Tanaka Y., Nandra K., Fabian A.C., *et al.*, 1995, Nature 375, 659.

[41] Uttley P., Taylor R.D., McHardy I.M., *et al.*, 2004, Monthly Notices of the Royal Astronomical Society 347, 1345.

[42] Volonteri M., Madau P., Quataert E., 2005, The Astrophysical Journal 620, 69.

[43] Wilkins D.R., Fabian A.C., 2011, Monthly Notices of the Royal Astronomical Society 414, 1269.

[44] Zoghbi A., Fabian A.C., Uttley P., *et al.*, 2010, Monthly Notices of the Royal Astronomical Society 401, 2419.

[45] *XMM-Newton* Science Operations Centre, *XMM-Newton: A Technical Description*, http://xmm.esac.esa.int, recovered May 15, 2013.

Appendices

Appendix A

Log of Observations

Table A.1: Log of Observations (full table)

Object Name	Observation ID	Start Date	Duration (ks)	GTI Exposure (ks)
B21128+31	0102040201	Nov. 22, 2000	24.61	15.61
TonS180	0110890401	Dec. 14, 2000	31.05	20.62
Mrk1044	0112600301	Jul. 23, 2002	8.38	5.55
1H0419-577	0112600401	Dec. 04, 2000	9.56	5.72
RXJ0323.2-4931	0140190101	Aug. 16, 2003	29.61	24.91
NGC 985	0150470601	Jul. 15, 2003	57.95	39.79
NGC 4051	0157560101	Nov. 22, 2002	51.87	45.82
ESO359-G19	0201130101	Mar. 09, 2004	24.44	16.80
H0439-272	0301450101	Aug. 13, 2005	20.52	13.93
Fairall 1116	0301450301	Aug. 28, 2005	20.52	14.05
QSO0056-363	0401930101	Nov. 26, 2006	47.11	41.39
RXJ1034.6+3938	0506440101	May 31, 2007	93.21	76.99
PG 0157+001	0101640201	Jul. 29, 2000	14.77	6.59
PG 0844+349	0103660201	Nov. 04, 2000	26.41	13.49
PG 1202+281	0109080101	May 30, 2002	17.92	12.86
PG 1048+342	0109080701	May 13, 2002	33.18	27.53
PG 1114+445	0109080801	May 14, 2002	43.51	37.50
PG 1307+085	0110950401	Jun. 13, 2002	13.97	10.84
PG 0947+396	0111290101	Nov. 03, 2001	21.98	17.55
PG 0953+414	0111290201	Nov. 22, 2001	15.57	11.53
PG 1115+407	0111290301	May 17, 2002	21.12	15.03
PG 1216+069	0111291101	Dec. 18, 2002	16.95	14.03
PG 1211+143	0502050101	Dec. 21, 2007	64.87	45.53

The names, observation IDs, start dates, durations, and GTI exposure times of the unique objects in the AGN sample.

Table A.1 Continued: Summary of Blurred Reflection Models

Object Name	Observation ID	Start Date	Duration (ks)	GTI Exposure (ks)
PG 1004+130	0140550601	May 04, 2003	22.21	18.08
3C 249.1	0153210101	Nov. 01, 2002	23.02	9.98
PG 0921+525	0201130501	Nov. 15, 2004	47.42	32.86
PG 1116+215	0111290401	Dec. 02, 2001	10.19	5.55
PG 1011-040	0202060101	May 08, 2005	31.92	24.53
PG 1126-041	0202060201	Dec. 31, 2004	33.82	29.06
PG 0050+124	0300470101	Jul. 19, 2005	85.51	58.05
PG 0043+039	0300890101	Jun. 15, 2005	31.81	26.60
PG 1229+204	0301450201	Jul. 09, 2005	25.51	17.34
PG 0052+251	0301450401	Jun. 26, 2005	20.52	14.00
PG 1259+593	0304570101	Apr. 20, 2006	33.92	9.76
Mrk 335	0306870101	Jan. 03, 2006	133.25	92.71
Mrk 586	0048740101	Jul. 23, 2002	47.34	19.53
NGC 7158	0103860501	Nov. 27, 2001	8.21	4.46
II Zw 177	0103861201	Jun. 07, 2001	12.96	8.60
E1346+266	0109070201	Jan. 13, 2003	72.06	48.94
Mrk 590	0201020201	Jul. 04, 2004	112.67	30.77
IRAS 13224-3809	0110890101	Jan. 19, 2002	64.02	53.59
PHL 1092	0110890901	Jan. 18, 2003	27.45	19.72
Mrk 896	0112600501	Nov. 15, 2001	11.21	7.149
Mrk 359	0112600601	Jul. 09, 2000	27.21	6.91
IRAS 04505-2958	0153100101	Sep. 09, 2003	15.93	11.77
IRAS 06269-0543	0153100601	Oct. 08, 2003	9.91	2.48
RXJ2241.8-4405	0153220101	May 17, 2003	10.92	0.57
RXJ1225.7-2055	0153220301	Jun. 12, 2003	13.92	3.58
Akn 564	0206400101	Jan. 06, 2005	101.77	69.29
5C3.100	0300910201	Aug. 01, 2005	43.71	5.35
1E0919+515	0300910301	Oct. 08, 2005	40.91	21.27
Mrk 507	0300910401	Jun. 17, 2005	27.61	3.39
1H0707-495	0511580101	Jan. 29, 2008	123.82	108.00
RXJ095208.7-014818	0065790101	Nov. 12, 2001	9.96	4.44
PHL 1811	0204310101	Nov. 1, 2004	32.92	27.21
J024912.86-081525.6	0303550101	Feb. 16, 2006	7.41	3.86
J082912.67+500652.3	0303550901	Apr. 26, 2006	17.45	2.31
J114008+030711	0305920201	Dec. 03, 2005	41.51	0.12
J135724.52+653505.8	0305920301	Apr. 04, 2005	57.45	19.05
PG1404+226	0051760201	Jun. 18, 2001	21.36	12.18
ESO323-G077	0300240501	Feb. 07, 2006	28.85	23.76
2MASSIJ1318176+324053	0135940201	Jul. 10, 2002	11.92	8.73
2MASSIJ2344495+122143	0149170101	Jul. 03, 2003	7.95	5.43
Akn 120	0147190101	Aug. 24, 2003	112.15	78.17
CTSA08.12	0201130301	Oct. 30, 2004	46.41	32.16
ESO15-ig011	0103861701	Sep. 29, 2000	13.55	5.00
ESO244-g17	0103860901	Dec. 18, 2000	22.61	17.06
Fairall 9	0605800401	Dec. 09, 2009	130.05	90.73
HS0810+5157	0148742101	Apr. 27, 2003	9.21	6.59
H1846-786	0147920701	Aug. 21, 2003	9.45	6.76

The names, observation IDs, start dates, durations, and GTI exposure times of the unique objects in the AGN sample.

Table A.1 Continued: Summary of Blurred Reflection Models

Object Name	Observation ID	Start Date	Duration (ks)	GTI Exposure (ks)
HE1029-1401	0203770101	Dec. 19, 2004	47.09	31.90
HE1143-1810	0201130201	Jun. 08, 2004	34.08	21.72
HE2217-2818	0302380401	Oct. 31, 2005	25.61	21.07
HS1939+7000	0148740701	Jun. 28, 2003	14.15	4.39
IC4329A	0147440101	Jun. 06, 2003	136.05	93.18
IRAS 13349+2438	0402080301	Jul. 16, 2006	68.91	47.94
IRAS 15091-2107	0300240201	Jul. 26, 2005	23.01	19.13
IRAS 17020+4544	0206860101	Aug. 30, 2004	21.82	14.97
IRASF 09159+2129	0303360101	Nov. 15, 2005	21.82	18.20
J124126.3-574955	0312191901	Feb. 01, 2006	11.87	8.83
J144414.6-574955	0207130401	Feb. 11, 2002	20.41	15.76
KUV18217+6419	0506210101	Dec. 10, 2007	14.32	9.72
MGC-2-58-22	0109130701	Dec. 01, 2000	11.76	7.22
MGC-01-13-025	0103861401	Aug. 30, 2000	13.01	1.18
MGC-02-14-009	0550640101	Feb. 27. 2009	125.08	107.80
MGC+8-11-11	0201930201	Apr. 09, 2004	38.45	26.55
Mrk 509	0601390201	Oct. 15, 2009	60.92	40.03
Mrk 766	0304030101	May 23, 2005	95.51	66.43
Mrk 841	0205340201	Jan. 17, 2005	72.65	32.13
Mrk 1018	0554920301	Aug. 07, 2008	17.62	12.03
MS2254.9-3712	0205390101	May 01, 2005	71.41	49.65
NGC 7469	0207090101	Nov. 30, 2004	85.02	59.18
NGC 7314	0111790101	May 02, 2001	44.66	30.11
NGC 2622	0302260201	Apr. 09, 2005	13.87	6.62
NGC 3516	0107460701	Nov. 09, 2001	129.99	89.94
NGC 3783	0112210101	Dec. 28, 2000	40.41	26.07
NGC 4235	0204650201	Jun. 09, 2004	13.11	8.96
NGC 4579	0112840101	Jun. 12, 2003	23.67	19.54
NGC 4593	0109970101	Jul. 02, 2000	28.06	9.50
NGC 5548	0089960301	Jul. 09, 2001	95.82	65.09
NGC 7213	0605800301	Nov. 11, 2009	132.52	87.92
PB 5062	0012440301	May 24, 2001	35.21	26.58
PDS 456	0501580101	Sep. 12, 2007	92.36	78.13
PG 0804+761	0605110201	Mar. 12, 2010	44.63	25.35
PG 1115+080	0203560401	Jul. 26, 2004	86.52	72.52
PG 1247+267	0143150201	Jun. 18, 2003	33.92	27.65
PG 1351+640	0205390301	Jun. 23, 2004	50.91	43.41
PG 1352+183	0109080401	Jul. 20, 2007	15.93	12.47
PG 1402+261	0400200201	Dec. 23, 2006	24.77	16.42
PG 1415+451	0109080501	Dec. 08, 2002	24.62	21.17
PG 1427+480	0109080901	May 31, 2002	39.69	35.20
PG 1440+356	0107660201	Dec. 23, 2001	32.62	24.84
PG 1444+407	0109080601	Aug. 11, 2002	21.97	18.72
PG 1630+377	0033540901	Jan. 06, 2002	17.62	13.02
PG 1634+706	0143150101	Nov. 22, 2002	19.71	15.62
PG 2302+029	0033541001	Nov. 29, 2001	13.16	8.92
Q0144-3938	0090070101	Jun. 17. 2002	33.02	27.94

*The names, observation IDs, start dates, durations, and GTI exposure times of the unique objects in the AGN sample.*

Table A.1 Continued: Summary of Blurred Reflection Models

Object Name	Observation ID	Start Date	Duration (ks)	GTI Exposure (ks)
Q1442+2931	0103060201	Aug. 01, 2002	41.87	32.01
Q2251-178	0012940101	May 18, 2002	65.37	44.73
UGC 3973	0502091001	Apr. 26, 2008	88.52	61.22
UGC 11763	0150470701	May 16, 2003	37.95	26.23
UGC 12138	0103860301	Jun. 03, 2001	8.11	4.50
ESO 113-g010	0301890101	Nov. 10, 2005	103.72	89.91
ESO 198-g24	0067190101	Jan. 24, 2001	34.11	21.70
ESO 416-g002	0103861101	Jun. 28, 2001	8.09	1.82
H 0557-385	0404260301	Nov. 03, 2006	80.71	56.19
HS 1824+6507	0148740401	Feb. 09, 2003	12.21	2.22
UGC 3973	0400070401	Mar. 19, 2007	20.45	13.99
IRASF 12397+3333	0202180201	Jun. 20, 2005	80.11	68.43
J14028+2631	0149170801	Aug. 01, 2003	6.91	3.22
LBQS 1228+1116	0306630201	Dec. 17, 2005	99.52	84.86
MGC-5-23-16	0112830301	May 13, 2001	38.44	14.56
MGC-05-01-013	0103861501	May 25, 2001	16.34	0.87
Mrk 205	0401240501	Oct. 22, 2006	59.31	52.46
Mrk 279	0302480501	Nov. 17, 2005	59.81	41.45
Mrk 352	0312190101	Jan. 24, 2006	13.05	8.58
Mrk 493	0112600801	Jan. 16, 2003	19.22	13.72
Mrk 609	0402110201	Jan. 27, 2007	21.81	17.12
Mrk 618	0307001301	Feb. 15, 2006	18.11	11.59
Mrk 728	0103861801	May 23, 2002	9.71	6.11
Mrk 766	0304030701	Jun. 03, 2005	35.02	24.13
Mrk 876	0102040601	Apr. 13, 2001	12.83	0.89
Mrk 1383	0102040501	Jul. 28, 2000	17.61	2.24
PG 1206+459	0033540601	May 11, 2002	13.19	8.01
PG 1244+026	0051760101	Jun. 17, 2001	13.06	6.21
PG 1322+659	0109080301	May 11, 2002	12.27	8.72
PG 1416-129	0203770201	Jul. 14, 2004	49.92	38.71
PG 1448+273	0152660101	Feb. 08, 2003	21.57	18.34
PG 1543+489	0505050301	Jun. 17, 2007	16.7	3.87
PG 1626+554	0109081101	May 05, 2002	10.92	5.52
PG 2233+134	0153220601	May 28, 2003	12.92	9.53
Q0119-286	0110950201	Jan. 07, 2003	9.23	6.51
RXJ1046.2+5256	0200480201	Oct. 25, 2004	45.79	24.77
UM269	0090070201	Jan. 04, 2002	21.12	16.22
BR0019-1522	0203460101	Dec. 22, 2004	49.91	42.48
1AXGJ044749-0629	0014740601	Sep. 08, 2002	28.89	20.50

The names, observation IDs, start dates, durations, and GTI exposure times of the objects in the AGN sample.

Appendix B

Ratio Plots
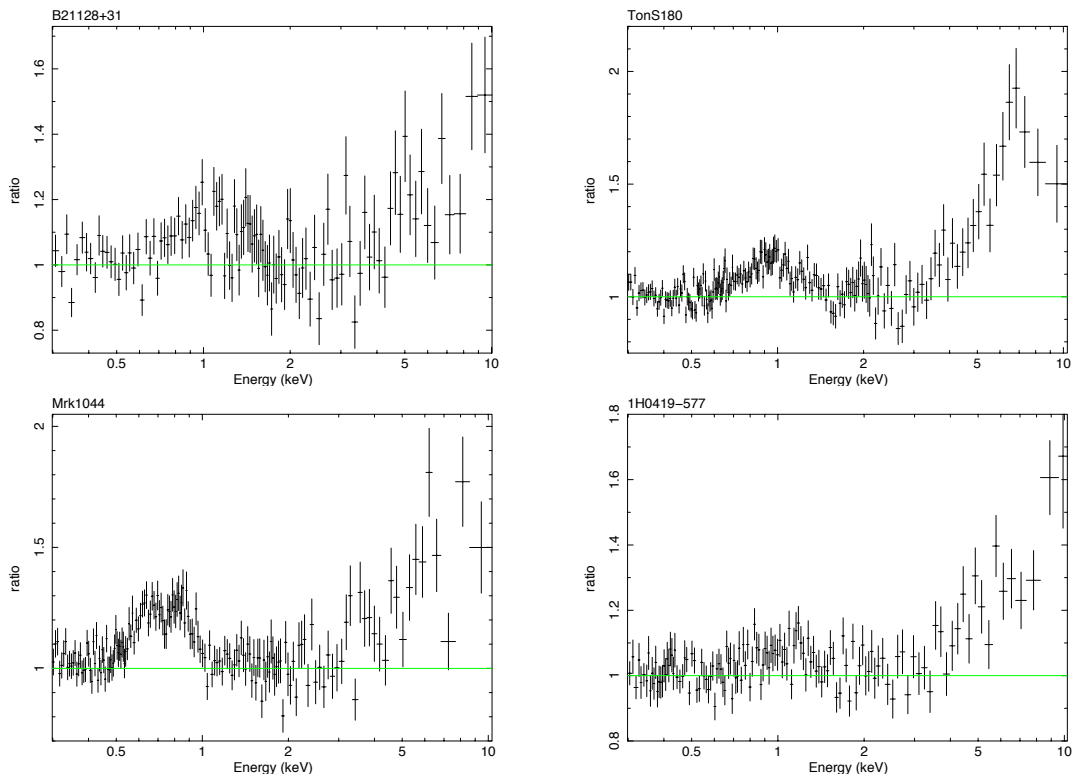
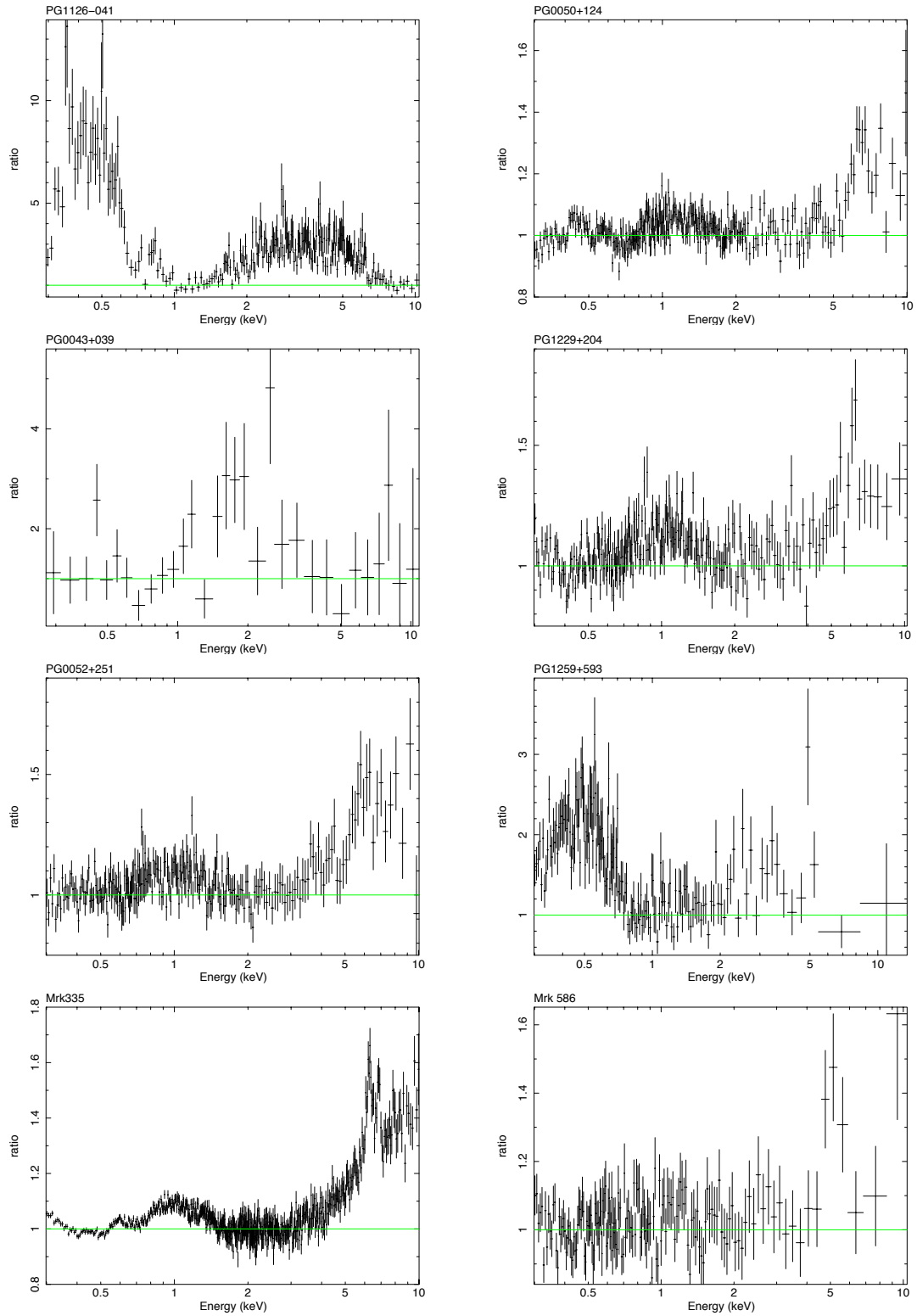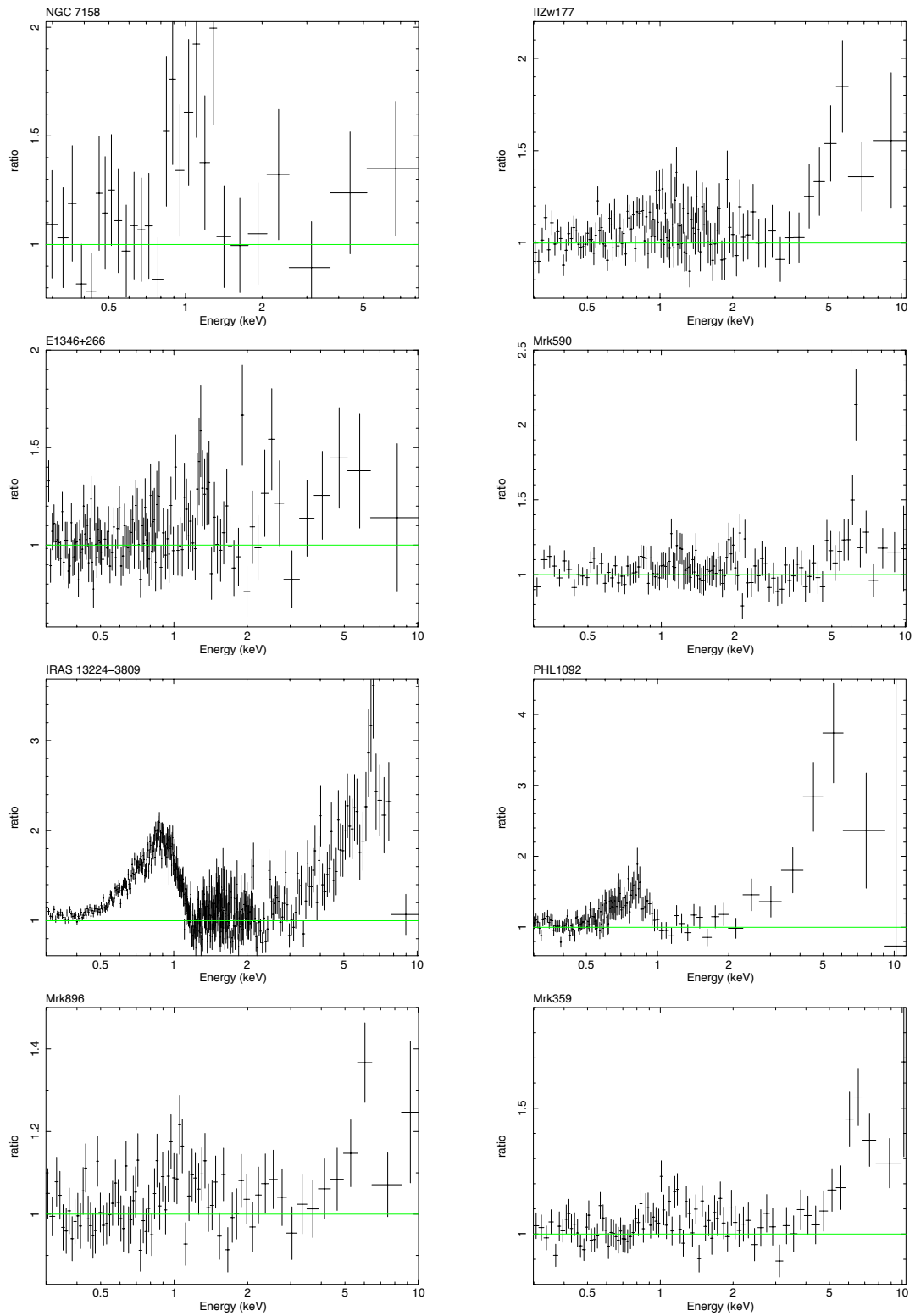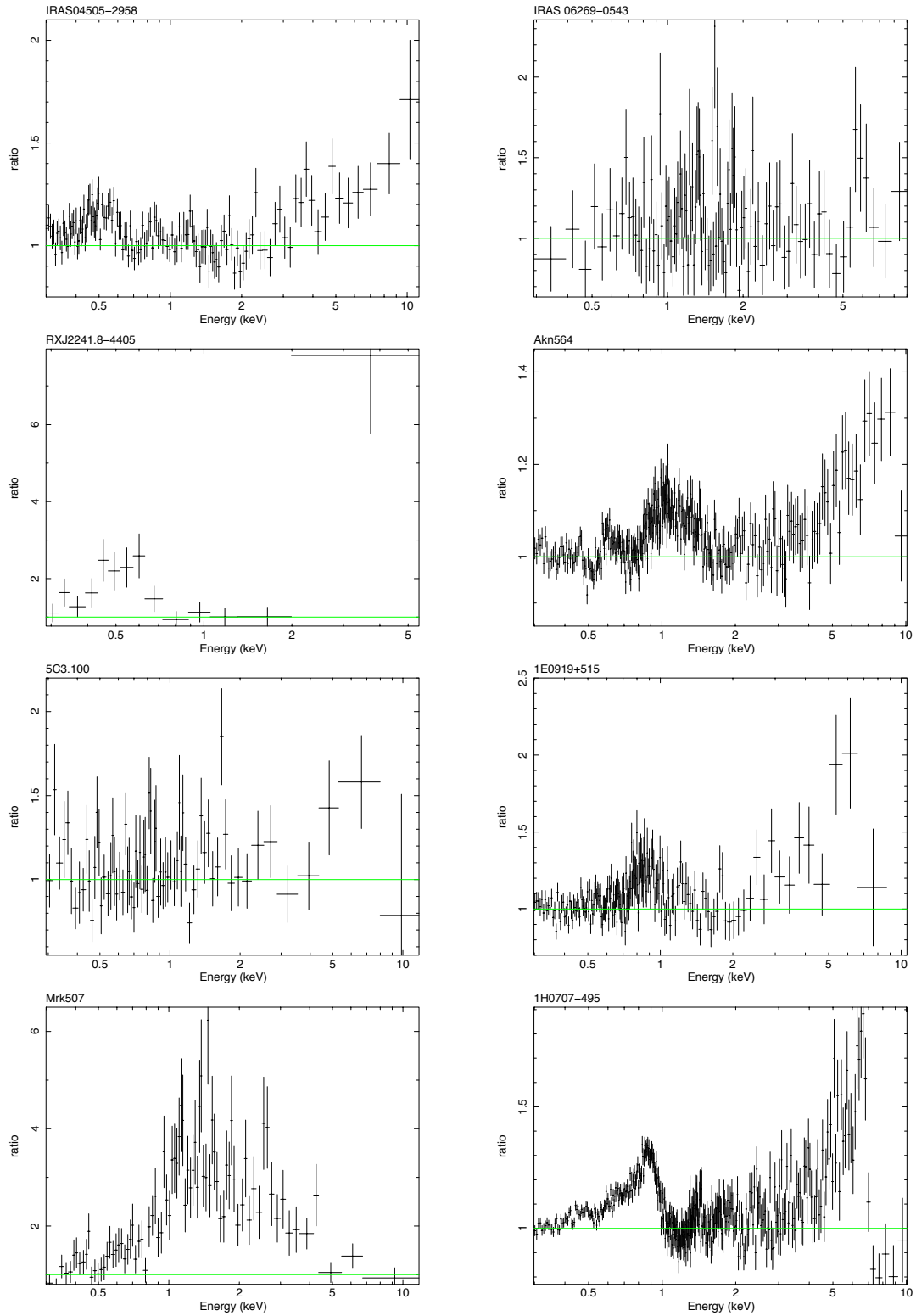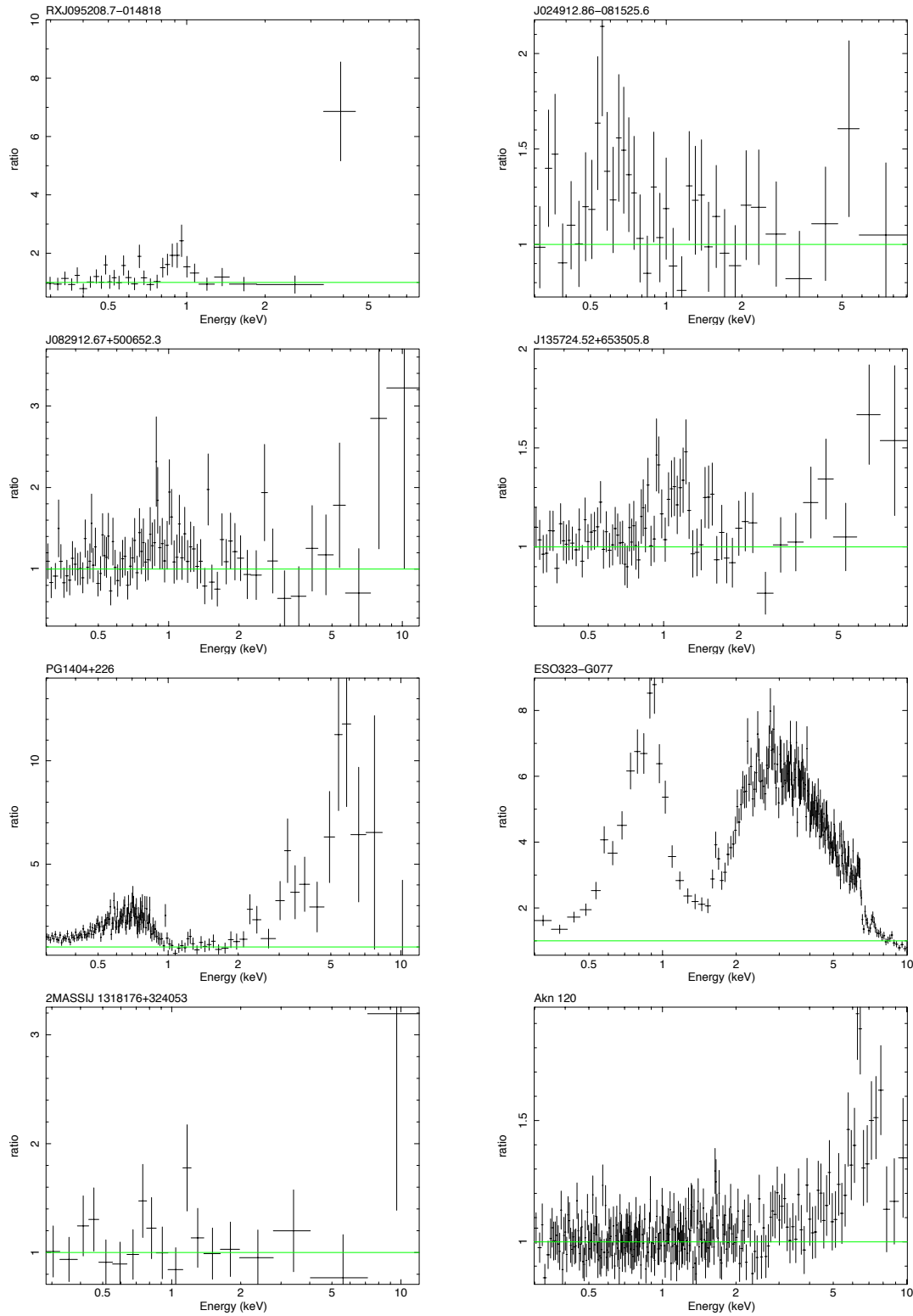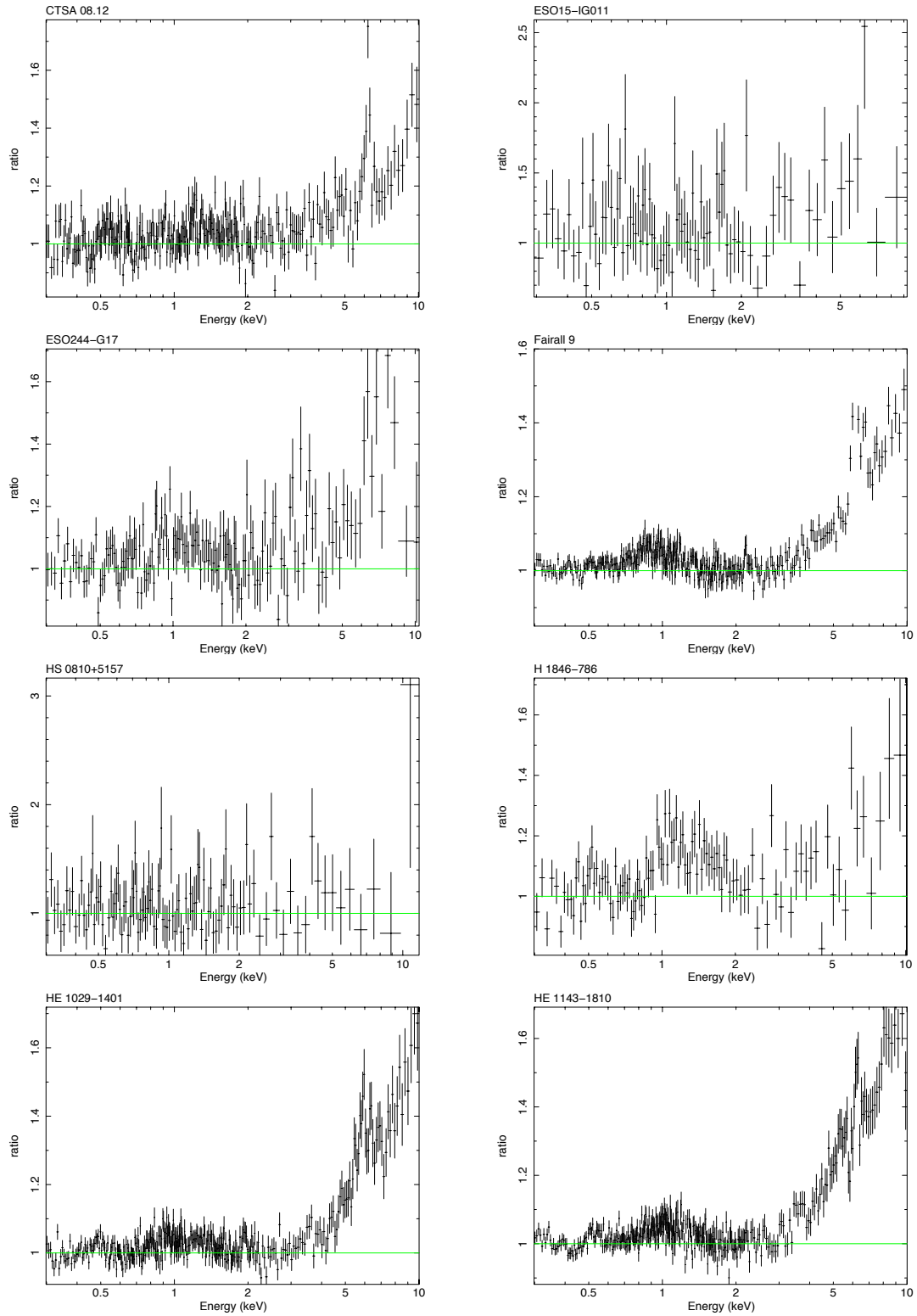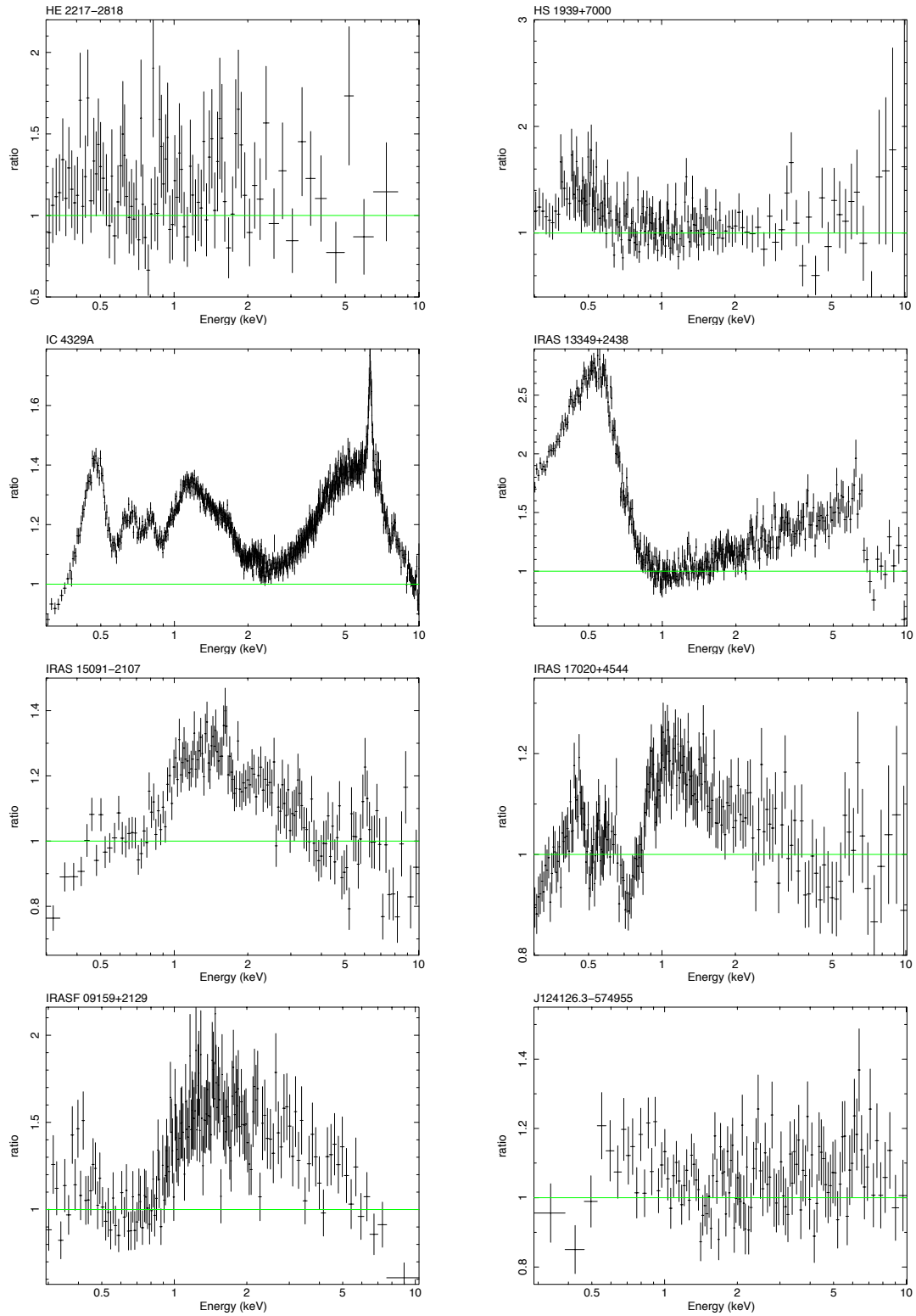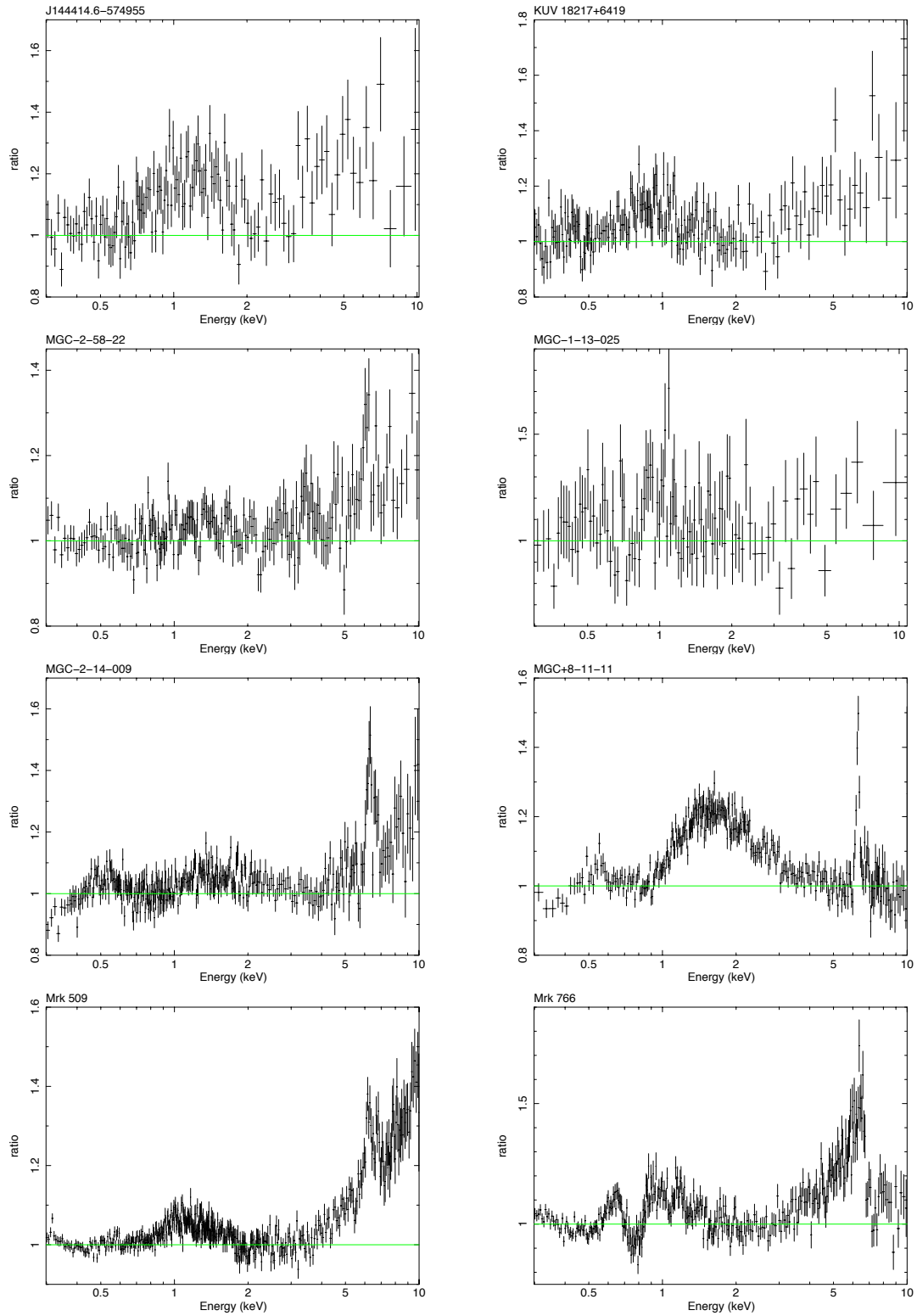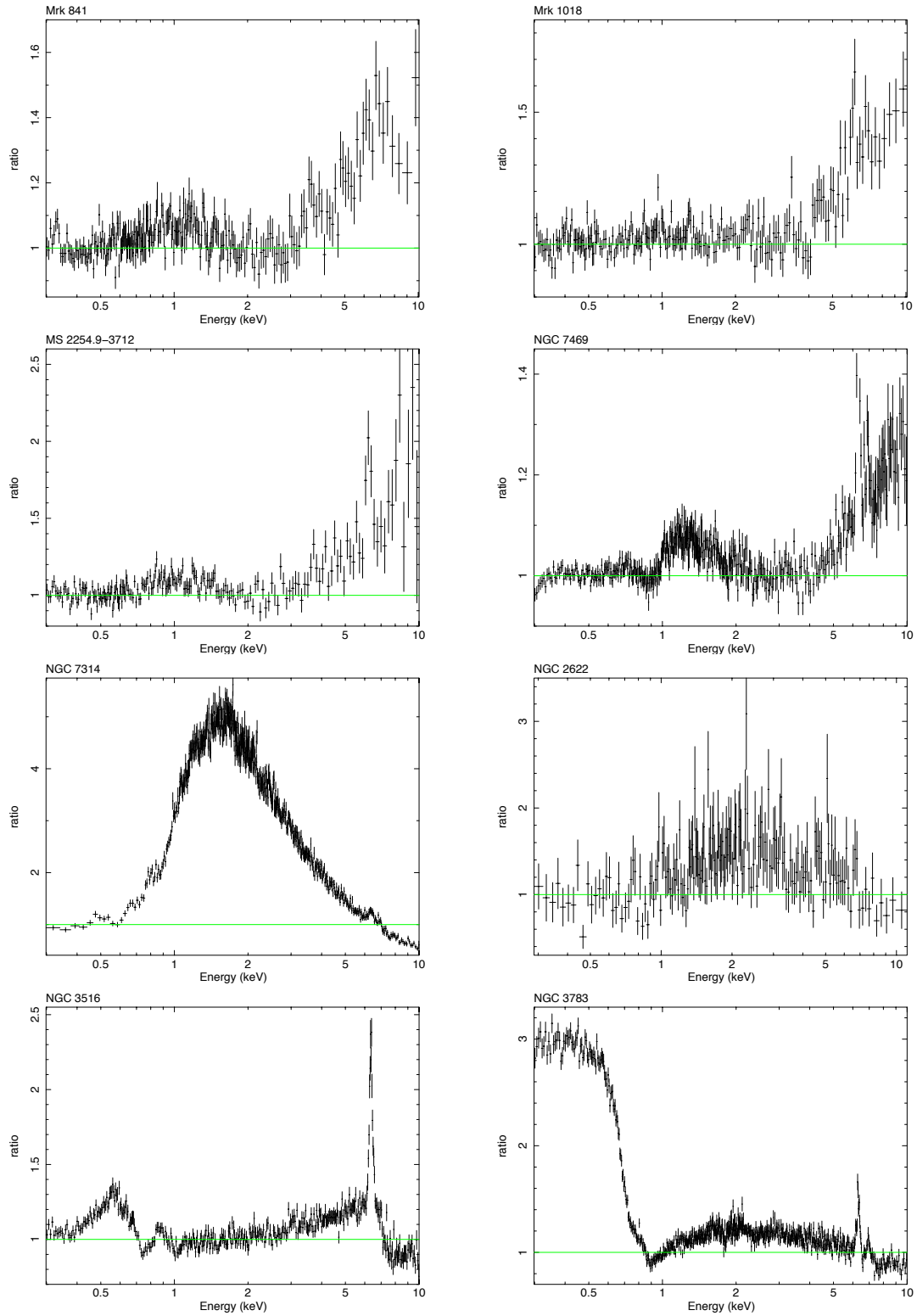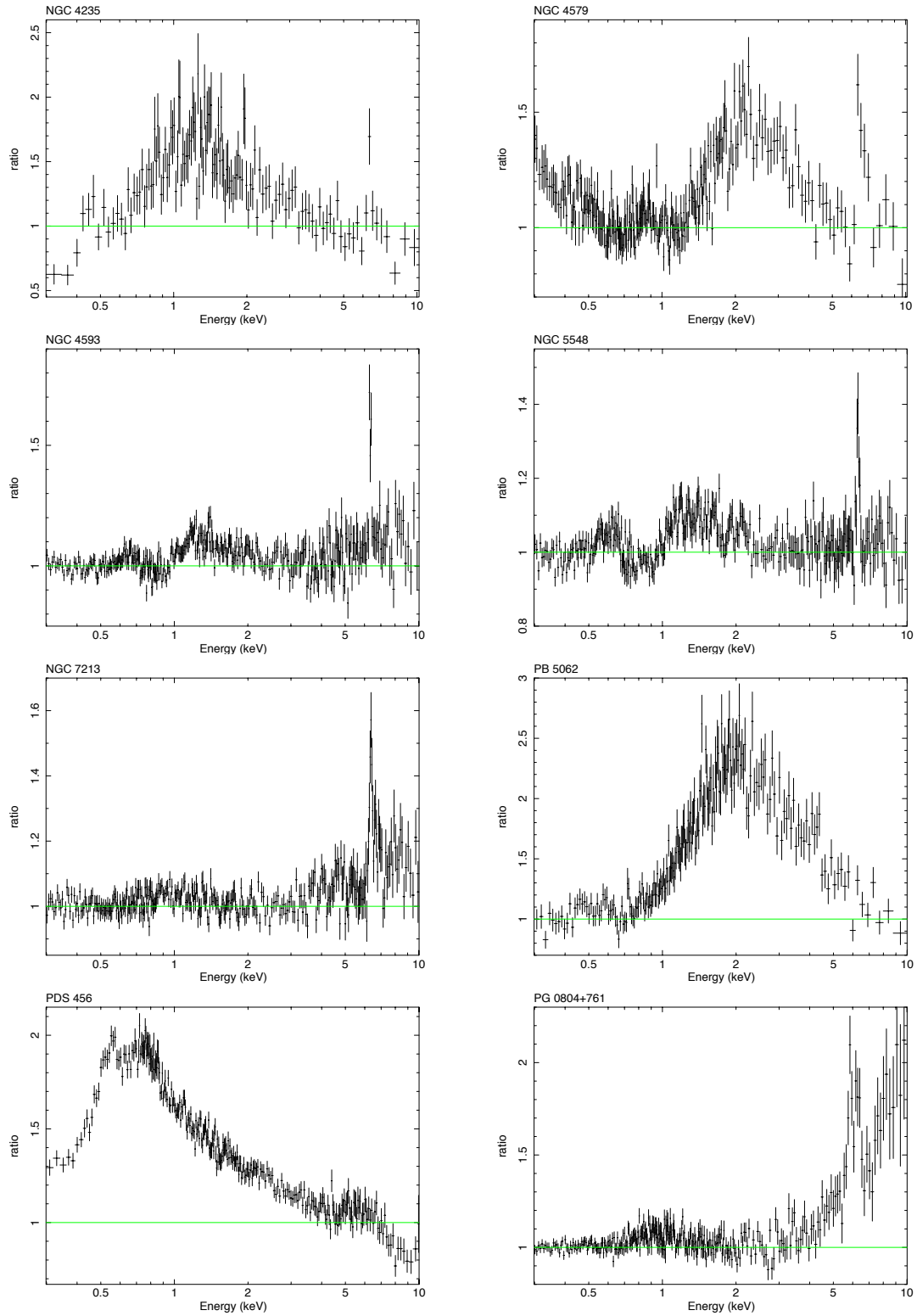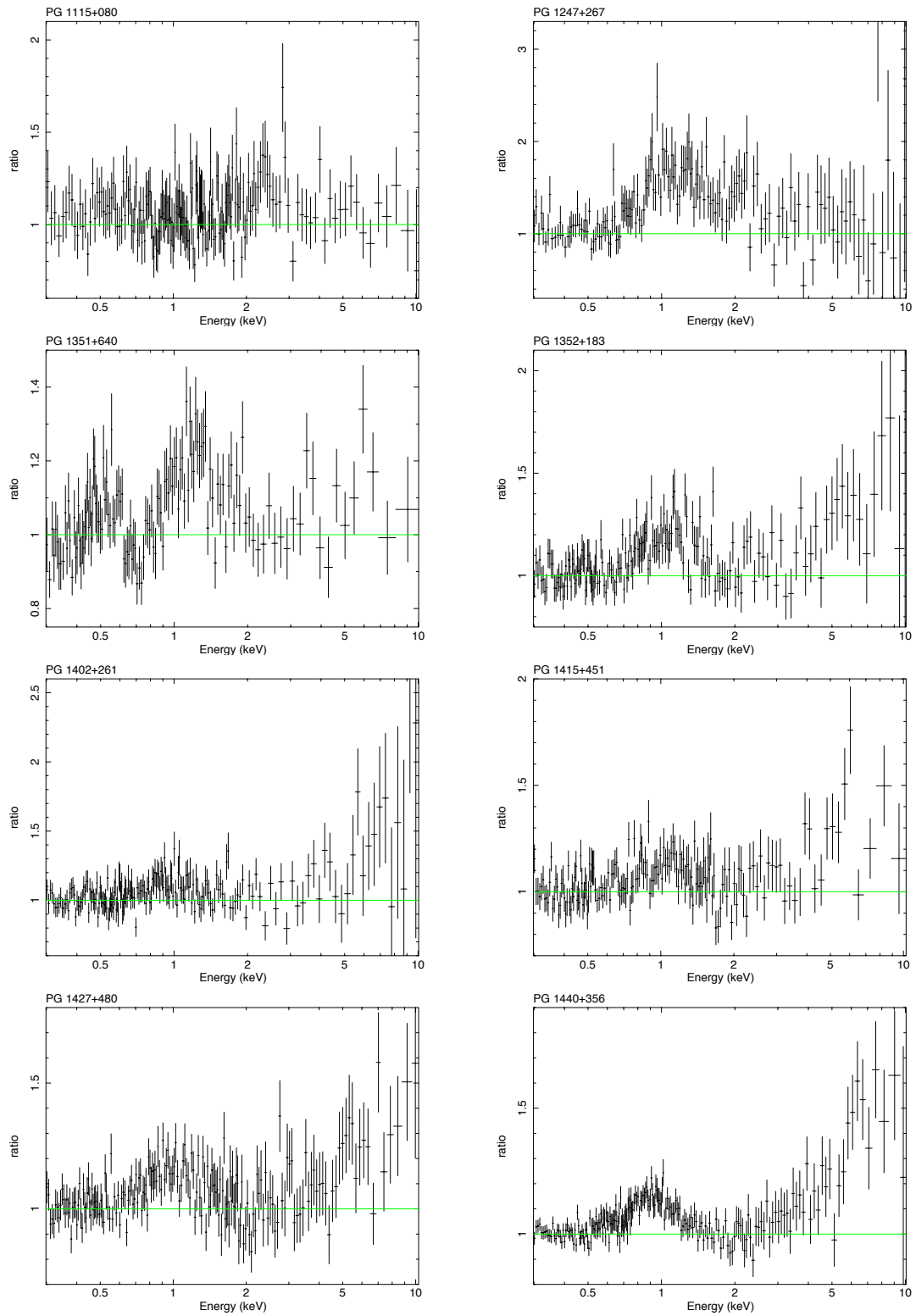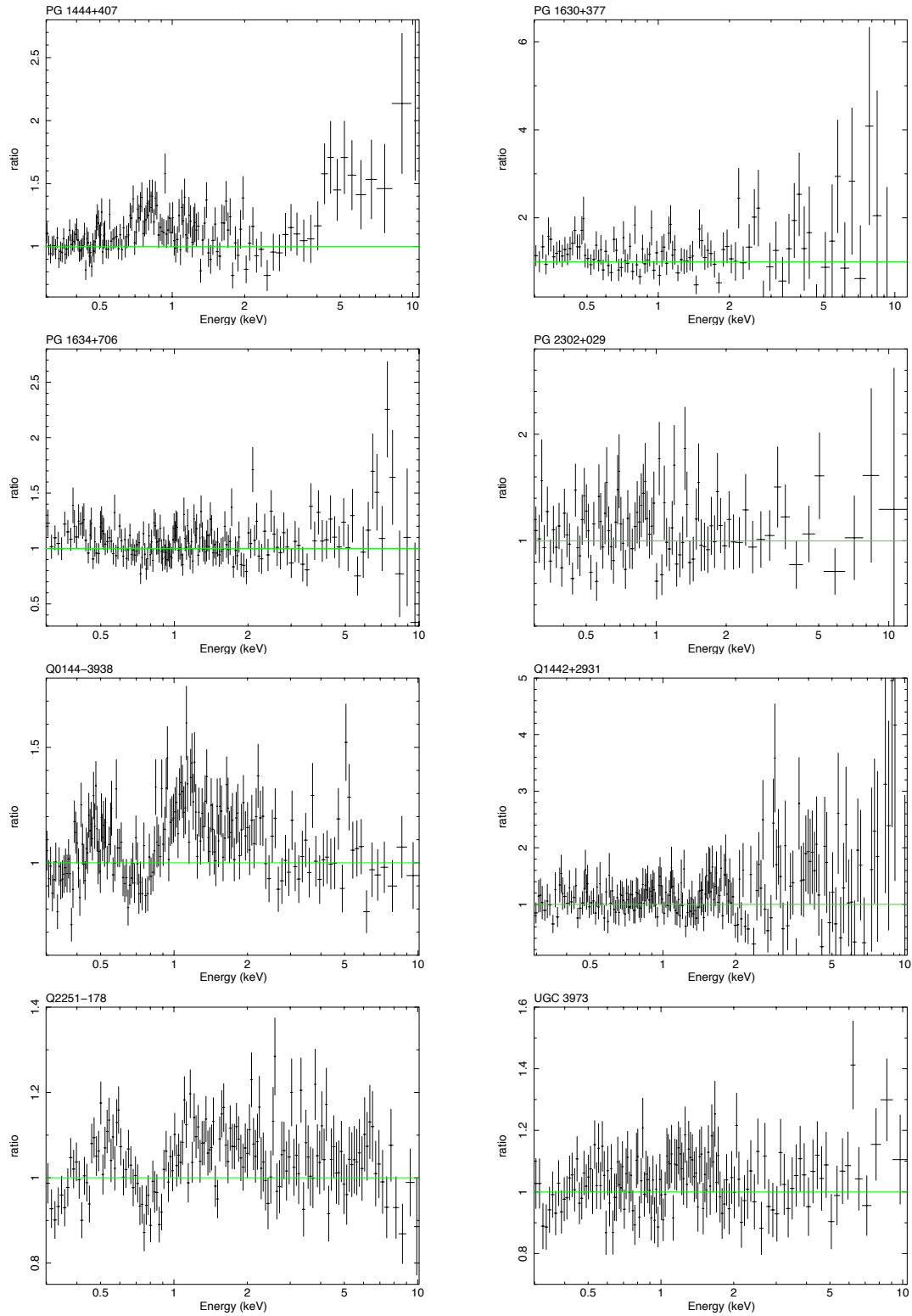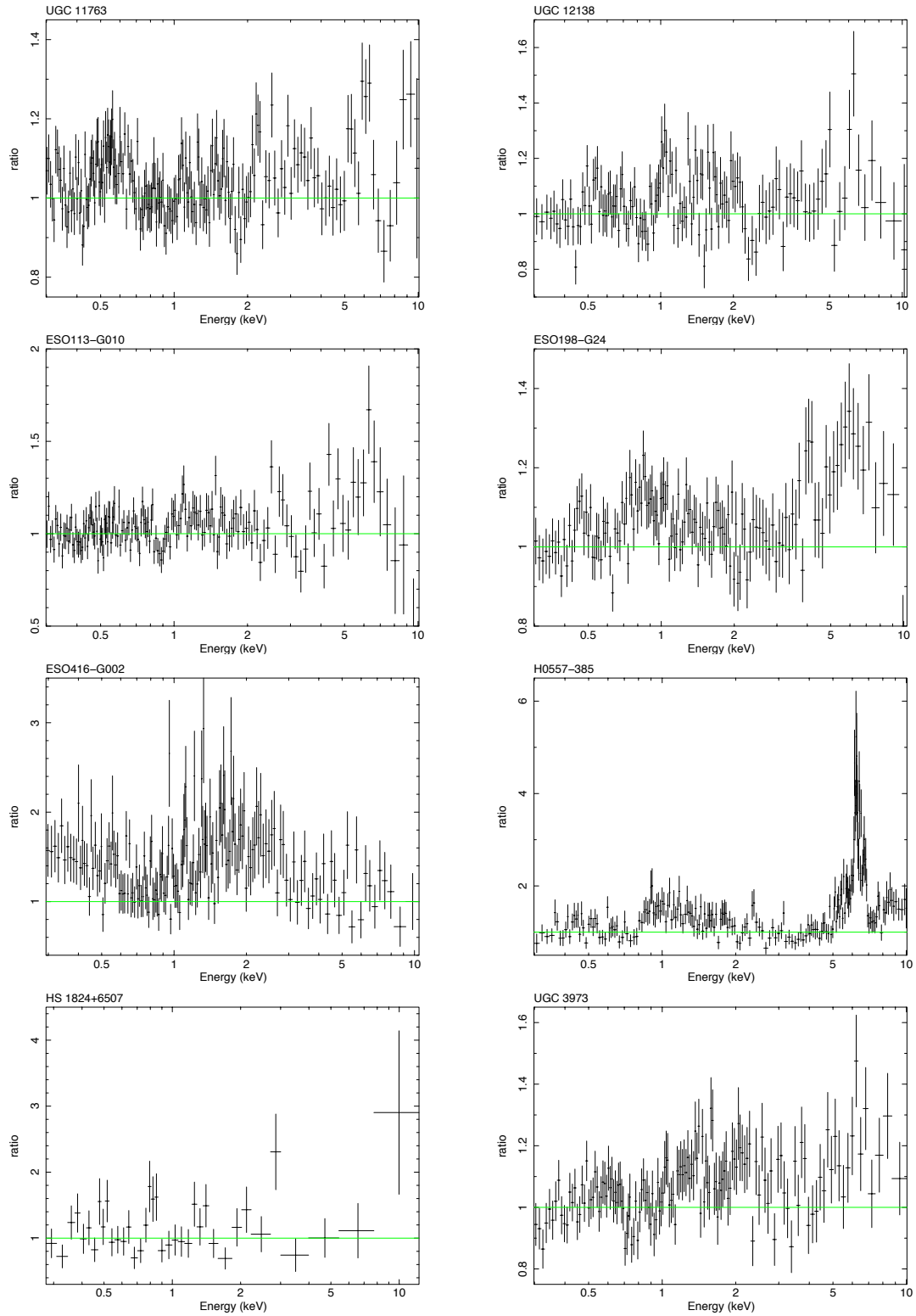*Ratio plots of the objects in the AGN sample.*

Ratio plots of the unique objects in the AGN sample.

Ratio plots of the unique objects in the AGN sample.

Ratio plots of the unique objects in the AGN sample.
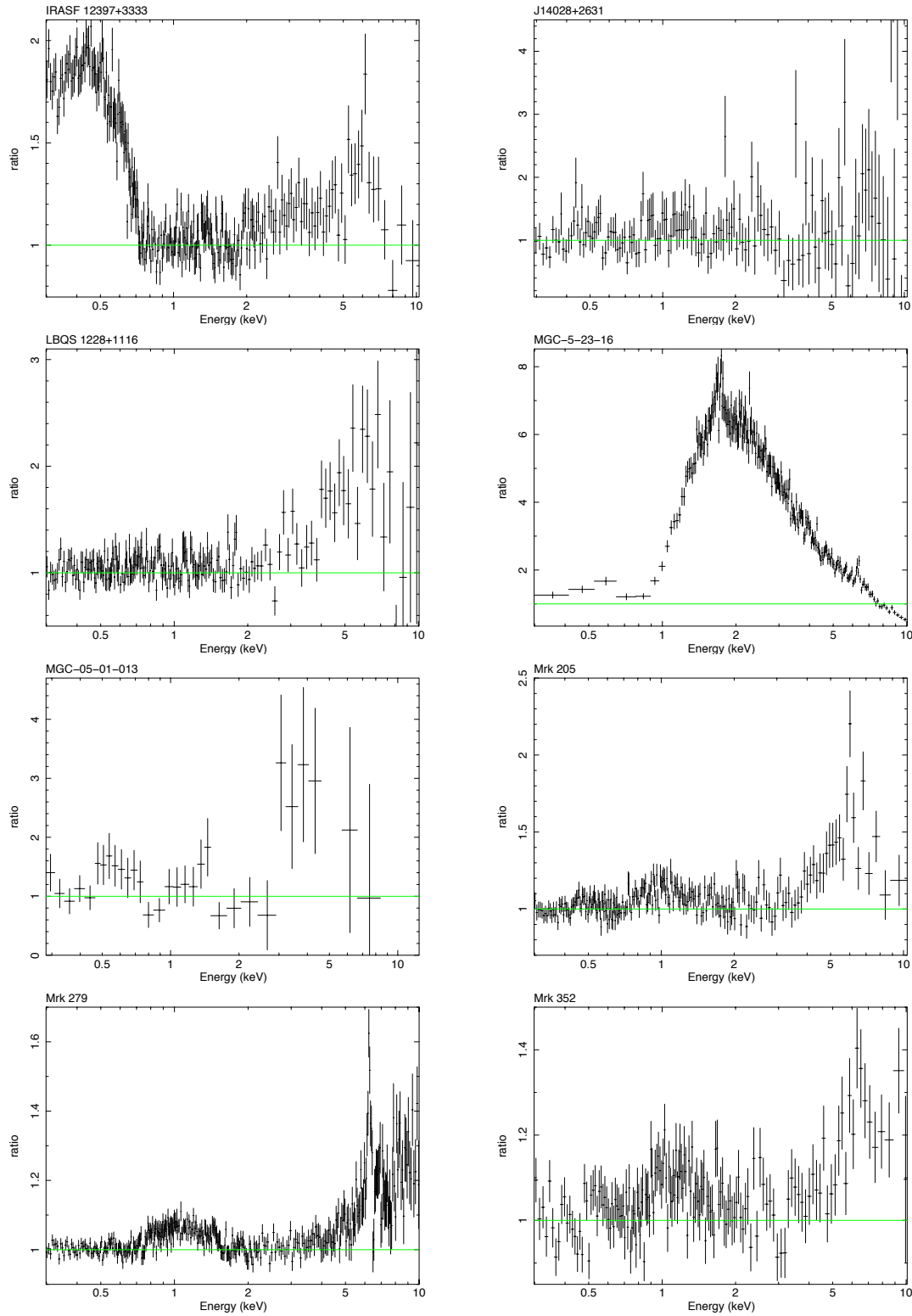
Ratio plots of the unique objects in the AGN sample.

Ratio plots of the unique objects in the AGN sample.

Ratio plots of the unique objects in the AGN sample.

Ratio plots of the unique objects in the AGN sample.
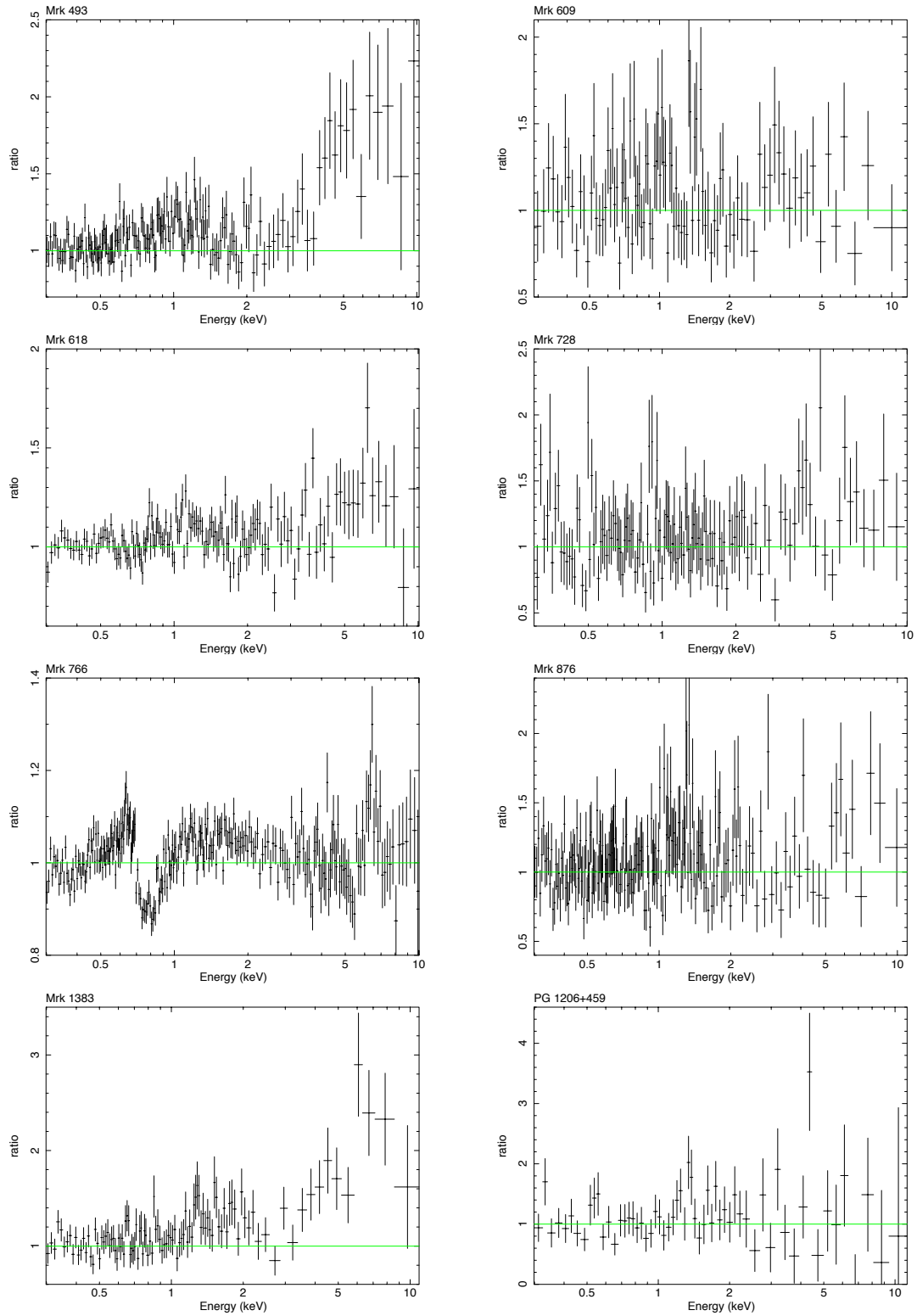
Ratio plots of the unique objects in the AGN sample.

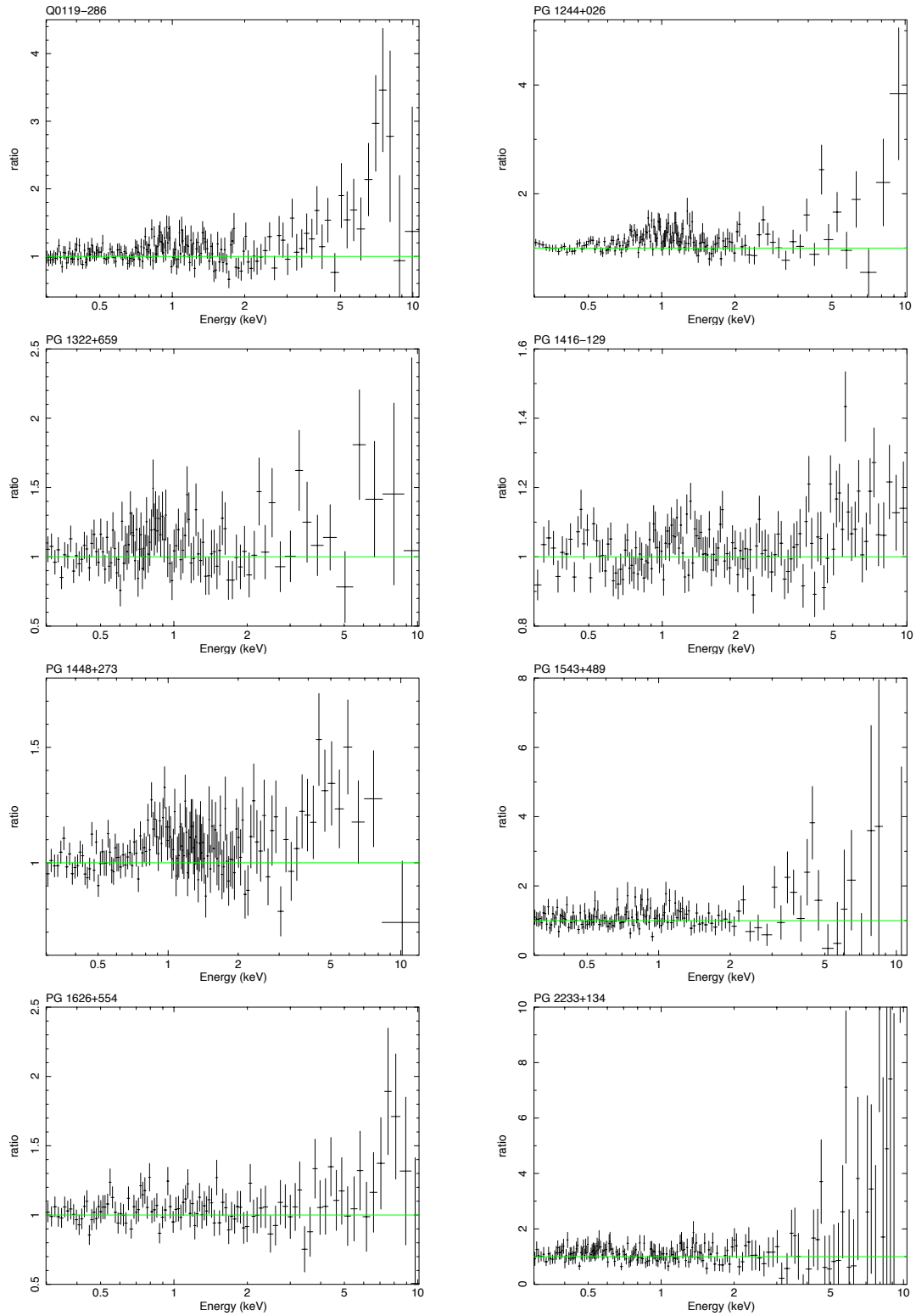*Ratio plots of the unique objects in the AGN sample.*

Ratio plots of the unique objects in the AGN sample.

Ratio plots of the unique objects in the AGN sample.

Ratio plots of the unique objects in the AGN sample.

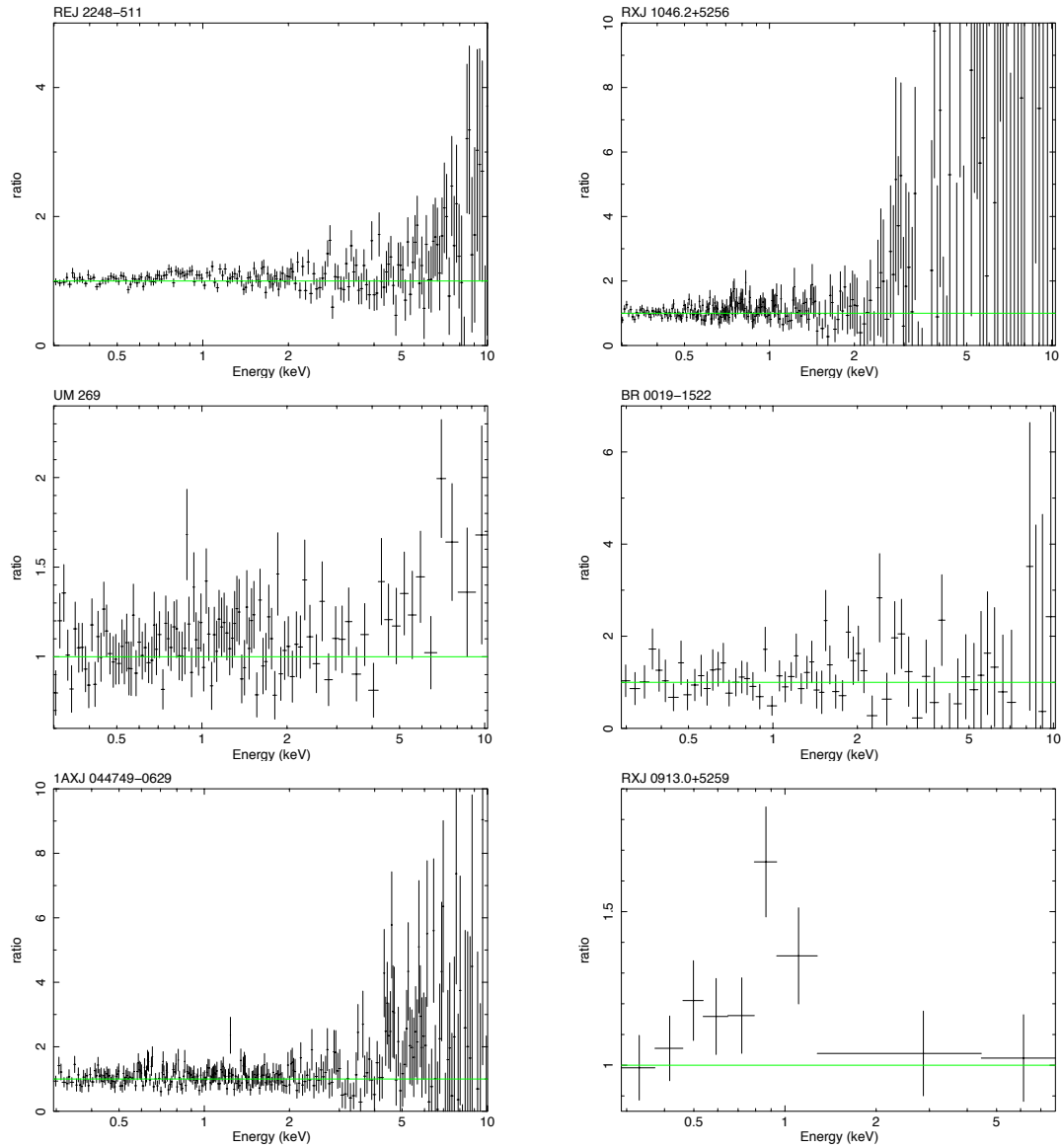*Ratio plots of the unique objects in the AGN sample.*

Ratio plots of the unique objects in the AGN sample.

Ratio plots of the unique objects in the AGN sample.

Ratio plots of the unique objects in the AGN sample.

Ratio plots of the unique objects in the AGN sample.

Ratio plots of the unique objects in the AGN sample.

Ratio plots of the unique objects in the AGN sample.